

UNCLASSIFIED

---

AD 278 063

*Reproduced  
by the*

ARMED SERVICES TECHNICAL INFORMATION AGENCY  
ARLINGTON HALL STATION  
ARLINGTON 12, VIRGINIA

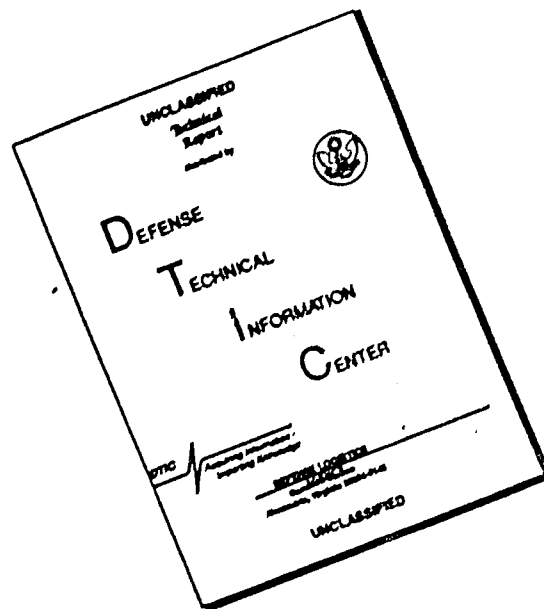


---

UNCLASSIFIED

NOTICE: When government or other drawings, specifications or other data are used for any purpose other than in connection with a definitely related government procurement operation, the U. S. Government thereby incurs no responsibility, nor any obligation whatsoever; and the fact that the Government may have formulated, furnished, or in any way supplied the said drawings, specifications, or other data is not to be regarded by implication or otherwise as in any manner licensing the holder or any other person or corporation, or conveying any rights or permission to manufacture, use or sell any patented invention that may in any way be related thereto.

# DISCLAIMER NOTICE



THIS DOCUMENT IS BEST QUALITY AVAILABLE. THE COPY FURNISHED TO DTIC CONTAINED A SIGNIFICANT NUMBER OF PAGES WHICH DO NOT REPRODUCE LEGIBLY.

278 063

62-4-3

278063

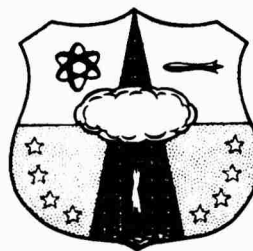
CATALOGED BY ASTIA  
AS AFM NO.

THE INVESTIGATION OF SILO AND TUNNEL LININGS

TECHNICAL DOCUMENTARY REPORT NUMBER AFSWC-TDR-62-1

Final Report

March 1962



Research Directorate  
AIR FORCE SPECIAL WEAPONS CENTER  
Air Force Systems Command  
Kirtland Air Force Base  
New Mexico

Project No. 1080, Task 108003

ARF Project 8199

NOX

(Prepared under Contract AF 29(601)-2596  
by Armour Research Foundation of Illinois  
Institute of Technology)



Copy No. \_\_\_\_\_

HEADQUARTERS  
AIR FORCE SPECIAL WEAPONS CENTER  
Air Force Systems Command  
Kirtland Air Force Base  
New Mexico

When Government drawings, specifications, or other data are used for any purpose other than in connection with a definitely related Government procurement operation, the United States Government thereby incurs no responsibility nor any obligation whatsoever; and the fact that the Government may have formulated, furnished, or in any way supplied the said drawings, specifications, or other data, is not to be regarded by implication or otherwise as in any manner licensing the holder or any other person or corporation, or conveying any rights or permission to manufacture, use, or sell any patented invention that may in any way be related thereto.

This report is made available for study upon the understanding that the Government's proprietary interests in and relating thereto shall not be impaired. In case of apparent conflict between the Government's proprietary interests and those of others, notify the Staff Judge Advocate, Air Force Systems Command, Andrews AF Base, Washington 25, DC.

This report is published for the exchange and stimulation of ideas; it does not necessarily express the intent or policy of any higher headquarters.

Qualified requesters may obtain copies of this report from ASTIA. Orders will be expedited if placed through the librarian or other staff member designated to request and receive documents from ASTIA.

THE INVESTIGATION OF SILO AND TUNNEL LININGS

TECHNICAL DOCUMENTARY REPORT NUMBER AFSWC-TDR-62-1

Final Report  
by R. R. Robinson  
March 1962

Research Directorate  
AIR FORCE SPECIAL WEAPONS CENTER  
Air Force Systems Command  
Kirtland Air Force Base  
New Mexico

Project No. 1080, Task 108003  
ARF Project 8199

(Prepared under Contract AF29(601)-2596  
by Armour Research Foundation of Illinois  
Institute of Technology)

## FOREWORD

This is the final report on Contract AF29(601)-2596, ARF Project K199, "The Investigation of Silo and Tunnel Linings", which commenced in February 1960. The work was administered under the Air Force Special Weapons Center, with Mr. C. Wiehle as project monitor.

Personnel contributing to this report include J. Anderson, C. J. Costantino, A. Humphreys, R. R. Robinson, R. Rowe, M. A. Salmon and T. A. Zaker. Particular acknowledgement is made to M. A. Salmon who served as project engineer until July 1961 and continued to make important contributions for the remainder of the contract.

ARMOUR RESEARCH FOUNDATION OF ILLINOIS INSTITUTE OF TECHNOLOGY

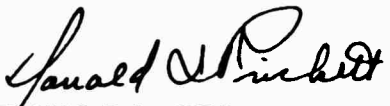
## A B S T R A C T


Some of the aspects of the problem of determining the response of underground cylindrical tunnel and silo linings to blast-induced loading are presented in this report. The studies include the effects on silo linings of differential horizontal soil displacements, vertical skin-friction forces generated by vertical compression of the surrounding soil, and axial response of a silo with integral cover to the blast-induced cover loading. (U)

A theoretical method for estimating the forces acting on a cylindrical structure subjected to air blast-induced ground shock is presented. The radial forces on the surface of the cylinder consist of the undisturbed free-field pressure component plus pressures proportional to the radial velocity and displacement of the structure relative to the free-field particles. The effect of virtual mass, foundation modulus, and damping on the response was studied by obtaining solutions appropriate for tunnel and silo linings. Static tests on three metal, cylindrical tunnel models buried in dense Ottawa sand are presented and compared with the theoretical method. (U)

## PUBLICATION REVIEW

This report has been reviewed and is approved.

  
DONALD I. PRICKETT  
Colonel USAF  
Director, Research Directorate

  
JOHN J. DISHUCK  
Colonel USAF  
DCS/ Plans & Operations



## TABLE OF CONTENTS

	<u>Page</u>
FOREWORD	ii
ABSTRACT	iii
<u>Section</u>	
I. INTRODUCTION	1
II. THEORETICAL ANALYSIS OF THE RESPONSE OF SILO AND TUNNEL LININGS TO RADIAL PRESSURE	5
A. Introduction.....	5
B. Basic Assumptions .....	5
C. Loading.....	7
D. Equations of Motion.....	20
E. Selection of Parameter Value .....	27
F. Results of the Analysis.....	29
1. Tunnel Cases (Side-On Orientation) .....	30
2. Silo Cases.....	31
G. Discussion of Results .....	42
H. Solution for Static Loading.....	44
Symbol Index (Section II)	51
III. STATIC LOAD TESTS ON TUNNELS	53
A. Introduction.....	53
B. Test Setup and Instrumentation.....	53
C. Test Results .....	62
D. Discussion of Results .....	82
Symbol Index (Section III)	87
IV. EFFECTS OF DIFFERENTIAL HORIZONTAL SOIL DISPLACEMENTS	89
A. Introduction.....	89
B. Analysis.....	89
Symbol Index (Section IV)	105
V. AXIAL LOADING OF SILO LININGS	107
A. Introduction.....	107
B. Analysis.....	109
C. Silo Model Push-Out Tests .....	115
D. Segmented Silo Model Tests .....	124
Symbol Index (Section V)	135

<u>Section</u>	<u>Page</u>
VI. CONCLUSIONS AND RECOMMENDATIONS	137
References.....	140

#### APPENDICES

A. AIR-BLAST INDUCED STRESS WAVES IN LAUNCH SILOS .....	A-1
B. PLAIN STRAIN SOLUTION FOR THE DISPLACEMENTS AT BOUNDARY OF A CIRCULAR HOLE IN AN INFINITE ELASTIC PLATE.....	B-1
C. COMPUTER PROGRAM FOR SHELL RESPONSE TO RADIAL PRESSURE.....	C-1

## LIST OF ILLUSTRATIONS

<u>Figure</u>	<u>Page</u>
1 Silo Stress Wave.....	9
2 Tunnel Stress Wave.....	10
3 Stress Wave and Shell Coordinate System .....	12
4 Pulse with Linear Rise.....	14
5 Wave Front Position Angles.....	15
6a Pressure-Time Variation (Case 26).....	33
6b Relative Displacement-Time Variation (Case 26) .....	34
6c Combined Stress-Time Variation (Case 26).....	35
7 Velocity-Time Variation (Tunnel) .....	36
8a Pressure-Time Variation (Case 35).....	38
8b Relative Displacement-Time Variation (Case 35).....	39
8c Combined-Stress-Time Variation (Case 35).....	40
9 Velocity-Time Variation (Silo) .....	41
10a Static Combined Stress-Radius to Thickness Ratio Variation.	48
10b Static Combined Stress-Radius to Thickness Ratio Variation.	49
11 Tunnel Model Test Arrangement.....	54
12a Tunnel Model Test Setup .....	56
12b Tunnel Model Prior to Sand Placement .....	56
13 Radial Displacement Gage .....	57
14a Radial Displacement Gage Assembly and Amplifier .....	59
14b Displacement Gage Position Pointer.....	59
14c Differential Transformer Probe .....	59

ARMOUR RESEARCH FOUNDATION OF ILLINOIS INSTITUTE OF TECHNOLOGY

<u>Figure</u>		<u>Page</u>
15	Surface Displacement Gages.....	60
16	Grain Size Distribution, Ottawa Sand.....	61
17	Surface Pressure -Displacement Variation, Test 1B, Steel Tunnel Model, $a/h = 60$ .....	64
18a	Surface Pressure-Average Displacement Variation Steel Tunnel Model, $a/h = 60$ .....	66
18b	Surface Pressure-Average Displacement Variation Steel Tunnel Model, $a/h = 40$ .....	67
18c	Surface Pressure-Average Displacement Variation Aluminum Tunnel Model, $a/h = 60$ .....	68
19	Radial Displacements for 15-Deg Segments (Test 1B) .....	69
20	Sectional Elevations of Silo Lining .....	90
21	Shell Coordinate System .....	91
22	Reinforced Concrete Shell Parameters (Elastic Stresses)....	98
23	Free-Field and Silo Horizontal Displacements.....	100
24	Load, Shear and Moment Diagrams .....	101
25	Relative Vertical Displacement of Silo and Structure.....	108
26	Section Through Silo Showing Assumed Failure Surface.....	110
27	Assumed Failure Surface and Resultant Forces.....	112
28	Independent Cover Silo Shear Stress for $w = c = 0$ .....	116
29	Silo Model Push-Out Test Arrangement.....	118
30	Angle of Internal Friction Versus Density, Ottawa Sand .....	120
31a	Load-Displacement Curves for Silo Model Push-Out Tests, Independent Cover.....	121
31b	Load-Displacement Curves for Silo Model Push-Out Tests, Monolithic Cover.....	122
32	Segmented Silo Model Test Arrangement.....	126

ARMOUR RESEARCH FOUNDATION OF ILLINOIS INSTITUTE OF TECHNOLOGY

<u>Figure</u>		<u>Page</u>
33	Segmented Silo Model.....	127
34	Segmented Silo Model.....	128
35	Typical Silo Model Segment (a) Assembled View (b) Exploded View.....	129
36a	Sealing Membrane and LVDT Arrangement.....	130
36b	ARF Dynamic Soil Facility.....	130
37	Surface Pressure Versus Silo Cover and Soil Displacement...	131
38a	Pressure Versus Segment Shear, Silo with Monolithic Cover..	132
38b	Surface Pressure Versus Segment Shear,Independent Cover...	133

#### APPENDICES

A-1	Wave and State Diagrams for Wave-Area Discontinuity Interaction .....	A-13
A-2	Force-Strain Relations for Steel and Concrete.....	A-14
A-3	Composite Force-Strain Relations for Silo Walls .....	A-15
A-4	Wave Diagram for Silo Wall Model.....	A-16
A-5	State Diagram for Silo Wall Model, I.....	A-17
A-6	State Diagram for Silo Wall Model, II .....	A-18
C-1	Flow Diagram for Machine Code .....	C-4

## LIST OF TABLES

<u>Table</u>	<u>Page</u>
1     Maximum Displacement, Stress, and Pressure for Tunnel Cases (Side-On Orientation).....	32
2     Maximum Displacement, Stress and Pressure for Silo Cases .	37
3     Tunnel Model Properties. ....	63
4a    Diametric Displacement, Inches X 10 <sup>4</sup> Test 1A Steel Tunnel Model, a/h = 60 .....	70
4b    Diametric Displacement, Inches X 10 <sup>4</sup> Test 1B Steel Tunnel Model, a/h = 60 .....	71
4c    Diametric Displacement, Inches X 10 <sup>4</sup> Test 2A Steel Tunnel Model, a/h = 40 .....	72
4d    Diametric Displacement, Inches X 10 <sup>4</sup> Test 2B Steel Tunnel Model, a/h = 40 .....	73
4e    Diametric Displacements, Inches X 10 <sup>4</sup> Test 3A Alum. Tunnel Model, a/h = 60 .....	74
4f    Diametric Displacements, Inches X 10 <sup>4</sup> Test 3B Alum. Tunnel Model, a/h = 60.....	75
5a    Direct and Bending Stresses, psi Test 1A, Steel Tunnel Model, a/h = 60 .....	76
5b    Direct and Bending Stresses, psi Test 1B, Steel Tunnel Model, a/h = 60 .....	77
5c    Direct and Bending Stresses, psi Test 2A, Steel Tunnel Model, a/h = 40 .....	78
5d    Direct and Bending Stresses, psi Test 2B, Steel Tunnel Model, a/h = 40 .....	79
5e    Direct and Bending Stresses, psi Test 3A, Aluminum Tunnel Model, a/h = 60.....	80
5f    Direct and Bending Stresses, psi Test 3B, Aluminum Tunnel Model, a/h = 60.....	81

<u>Table</u>		<u>Page</u>
6	Differential Horizontal Displacement Results, Summary.....	103
7	Silo Model Push-Out Tests.....	119

## APPENDICES

A-1		
C-1	Output Format.....	C-6

## INVESTIGATION OF SILO AND TUNNEL LININGS

### I. INTRODUCTION

This is the final report on Air Force Contract AF 29(601)-2596, "The Investigation of Silo and Tunnel Linings", initiated on February 26, 1960 and extended on January 5, 1961. This report covers the work performed by the Armour Research Foundation during the course of the contract.

To prepare adequate economical designs for silo and tunnel linings to resist blast induced loads, an understanding of the behavior of these structures in their soil environment is necessary. The objective of this program was to develop methods for the analysis of the response of silo and tunnel linings to blast loads. It is anticipated that the results of this study can be incorporated in a rational method of design for these structures.

The air-blast pressure traveling over the ground surface produces stresses and displacements in the soil in both vertical and horizontal directions. Since the resistance to deformation of an underground structure differs from that of the soil it replaces, a knowledge of the state of stress in the free-field is insufficient to permit direct determination of the loading on the structure. That is, some consideration must be given to the major problem of estimating the effects on loading of the soil-structure interaction.

Consider the effects of air blast induced ground shock on a cylinder of soil which a silo or tunnel lining replaces. The lateral surface of the cylinder will be subjected to certain stresses which will produce deformation. These stresses and deformations are known to the extent that free-field effects can be predicted. In general, the deformations will be such that originally circular cross sections of the cylinder will become elliptical in shape, the axis of the cylinder will become curved, and there will be a shortening of the cylinder in the axial direction. The lining which replaces the soil will tend to deform in the same way. The elliptical deformation of originally circular cross sections will produce circumferential bending stresses while the uniform component of the radial pressure will cause compressive

ARMOUR RESEARCH FOUNDATION OF ILLINOIS INSTITUTE OF TECHNOLOGY



circumferential stress. The curvature of the axis of the lining will produce longitudinal bending stresses in the lining acting as a beam and, since the lining will, in general, be more rigid in axial compression than the column of soil it replaces, longitudinal friction forces between the soil and the lining will produce direct axial stress.

To simplify the analysis, each of these effects is considered separately, as follows.

1. An analytical method for estimating the interaction effects on the response of a circular cross section of such cylindrical structures as silo and tunnel linings is presented in Section II. In this analysis, an attempt is made to account for the soil-structure interaction by introducing load components proportional to the displacement and velocity of corresponding points in the undisturbed free-field. Inertial effects arising from the disturbance of the free-field, caused by the presence of the structure, are accounted for by the addition of a virtual mass to the actual mass of the structure. The constants of proportionality relating relative displacement and velocity to load are estimated on the basis of consideration of certain elastic media properties. The effect on the dynamic response to variations in the constants are then studied to determine the sensitivity of the results to the parameters. The analysis should be of value in estimating the relative importance of dynamic effects on the response of silo and tunnel structures, and in establishing the range of applicability of simple design criteria based on static loadings. It should also be useful in assessing the relative merits of flexible versus rigid linings.

Since the method of analysis is intended to be applicable to structures buried in soil, an inelastic medium, the appropriate values for the constants relating load to relative displacement and velocity, the virtual mass, and etc., must be determined experimentally. A test program to investigate the problems associated with the evaluation of the parameters for cylindrical structures under static load, is presented in Section III.

2. The blast induced horizontal displacements of the free field (at points remote from ground zero) will generally be nonlinear with depth. The static behavior of silo linings, as a result of the imposed differential horizontal displacements, is investigated analytically in Section IV. Expressions are derived for the determination of bending and shear stress under the assumption that loading is proportional to the displacement of the structure relative to the given free field profile. It is shown in the analysis that axial curvature has a secondary effect on the shell deformations in the plane of the circular cross sections.

3. Theoretical and experimental studies concerning the axial skin friction loading of silo linings are described in Section V. These surface tractions result from the relative vertical displacement at the structure-soil interface, arising from soil compression generated by the intense surface overpressure. The investigation of this loading aspect relates to static behavior only. The analysis is concerned with the equilibrium of an elemental wedge of soil at impending failure (bounded by assumed failure surfaces at the silo lining and a conical surface through to soil) assuming Coulomb shear at the failure surface. Push-out tests of a silo model embedded in dense and loose Ottawa sand and experiments on a segmented silo model in dense sand are also given.

4. The passage of the air shock front over the silo cover results in the sudden application of vertical load to the silo wall if the cover is integral with the lining. A compression wave travels down the lining and is reflected at the base. The nature of the reflected wave depends on conditions at the base. In general, for silos founded in soil, the elastic modulus of the foundation will be such that a tension wave will be reflected. Since concrete has very little tensile strength, the vertical reinforcing steel must be capable of preventing spallation failures. In Appendix A, a method for the analysis of the effects of axial stress waves is presented and applied to a representative launch silo.

## II. THEORETICAL ANALYSIS OF THE RESPONSE OF SILO AND TUNNEL LININGS TO RADIAL PRESSURE

### A. Introduction

The stresses and displacements produced in soils by the air shock of a nuclear weapon are not well understood. The two primary reasons for this are, first, the complexity of the constitutive equations required to describe the material properties of soil and, secondly, the difficulty in the analysis of the subsurface effects of time-dependent air-blast loadings in any but ideally elastic media. The semiempirical methods developed for the prediction of subsurface stresses and displacements as functions of time are based on greatly simplified analytical models and the limited results of full scale tests (see, for example, Ref. 1).

The analysis presented in this section gives a method for estimating the significance of the dynamic effects of blast-induced earth pressure loadings on underground silo and tunnel linings in the plane of the circular cross section. It is not an exact solution (in the sense that it is a solution for the response of a structure in an inelastic medium with known properties) to the disturbance produced in such a medium by surface air-blast loading. In fact, no exact solutions in this sense have been obtained for the design of these structures for static earth pressure loadings. That is, design methods currently used for static loads are semiempirical. It is hoped that with the accumulation of experimental data on the response of buried structures to blast-induced loadings, the analysis presented here will constitute a method of design for dynamic loads.

### B. Basic Assumptions

The objective of the analysis presented in this section is the determination of the significance of dynamic effects on the deformation of an originally circular cross section in its own plane. The effects of variation in the loading in the axial direction are neglected. This is equivalent to the assumption that the loading is uniformly distributed along the cylinder axis. In this way the problem is reduced to the determination of the response of a ring to forces acting in the plane of the ring.

ARMOUR RESEARCH FOUNDATION OF ILLINOIS INSTITUTE OF TECHNOLOGY

The tangential component of the soil pressures acting on the ring is neglected. The magnitude of this force is limited by the coefficient of friction and the magnitude of the normal component of the loading. There does not seem to be a simple way to estimate these forces.

One possible approach to the design of a silo or tunnel lining would be to estimate the free-field stresses and strains using methods currently available and then determine which of the following conditions impose the most severe stresses; 1) the radial component of the free-field stress acting as a static load or 2) the stresses caused by requiring the radial displacements of the cylinder to conform to the free-field displacements. These two conditions represent limiting cases for static loading. In the conventional design of tunnels for static loads, this procedure has been refined by taking into account the flexibility of the structure (3)\*. This can be done by assuming that differential radial displacements of points on the structure relative to displacement of corresponding points in the free field result in changes in the loading, directly proportional to the magnitude of the relative displacement. There is some experimental data available (3, 4), on both full scale and model structures to use as a basis for estimating the appropriate value of the constant of proportionality (the "foundation modulus") for various types of soils.

In the design for dynamic loads induced by air blast, it is clear that effects not present in static loading may be important. That is, one would expect the loading at a point on the structure to be influenced by the relative velocity as well as the relative displacement with respect to a corresponding point in the undisturbed free field. In addition, one would suppose that the presence of the surrounding soil has the effect of increasing the natural periods of vibration of the structure. An effective mass has been added to the actual mass to account for this effect. Since there is, at this time, no experimental data on which to base the selection of appropriate values for the constant of proportionality between relative velocity and change in load or the virtual or effective mass, estimates must be made.

In this analysis, an attempt is made to take each of these effects

---

\* Numbers in parentheses cite references listed on page 140.

into account. We assume that the loading on the structure consists of the components:

- 1) the radial component of the free-field stress,
- 2) a component proportional to the relative displacement ( $w_0 - w$ ), where  $w$  is the radial displacement of a point on the shell and  $w_0$  is the corresponding component of the free-field displacement, and
- 3) a component proportional to the relative velocity ( $\dot{w}_0 - \dot{w}$ ), where dots denote differentiation with respect to time.

A virtual mass has been added to the actual mass in computing the response of each of the modes. To compute the loading on a cylinder according to this scheme, it is necessary to know the free-field stress and displacement as functions of time and to select the factors of proportionality which relate relative displacement and velocity to load. To obtain a reasonable estimate of the range of values for these parameters, the properties of elastic media (not a true soil) are considered (Section II E). Ultimately, the selection of these factors must be based on experimental results in soil.

As mentioned, methods of predicting free-field stress and displacement have not been advanced to the point where it is possible to predict these quantities as functions of time for a specified range of blast and soil parameters. It is, however, possible to make estimates of peak stress, displacement, and strain. To estimate the importance of dynamic effects, the peak stress and strain in the plane of the cross section are assumed produced by the passage of a plane compression wave traveling at a constant speed. The results should permit an estimation of the importance of dynamic effects.

### C. Loading

The maximum values of the free-field stress and strain in the plane of the cross section as well as the rise time at these values are assumed known. The speed with which the disturbance transits the cross section is assumed known and constant. For a silo, this speed will be equal to the speed of the air-shock front since, for the pressure range of

of interest (above 100 psi), the speed of the air shock will exceed that of compression waves in most soils. For a tunnel oriented side-on to ground zero, the speed with which the cross section is engulfed cannot exceed the speed of compression waves in the soil, while, for end-on orientation, less time will be required for engulfment. Sketches of each of these cases are shown in figures 1 and 2. In the case of the silo and the case of end-on orientation of the tunnel, the speed with which a given cross section is engulfed is greater than the speed of a compression wave in the soil. Therefore, the hypothetical compression wave which is assumed to cause the observed stress and strain in the plane of the cross section must make an angle  $\chi$  with the normal to the plane of the cross section as shown in the sketches. The assumption that the observed free-field values of stress and strain could be produced by a compression wave imposes certain restrictions. Since in a plane compression wave the strains in the plane of the wave front are zero, there is no strain in the direction of the diameter perpendicular to the direction of engulfment. In the three cases shown, this diameter is perpendicular to a line through ground zero and therefore it is expected that in these cases the observed strains will be negligibly small. However, for tunnel orientations intermediate to those shown in figure 2, this strain will be somewhat larger, but it will doubtless be much smaller than the strain in the vertical direction.

A second restriction imposed by our assumption is that a certain relationship exists between the observed values of the stress biaxiality ratio ( $\beta$ ), the apparent modulus ( $E^*$ ), the ratio of stress ( $\sigma$ ) to strain ( $\epsilon$ ) in the plane of the ring, and the speed of engulfment ( $c$ ). With reference to figure 1, the speed of compression waves for a given soil is

$$c_c = \sqrt{\frac{E_c}{\rho}} \quad (1)$$

where

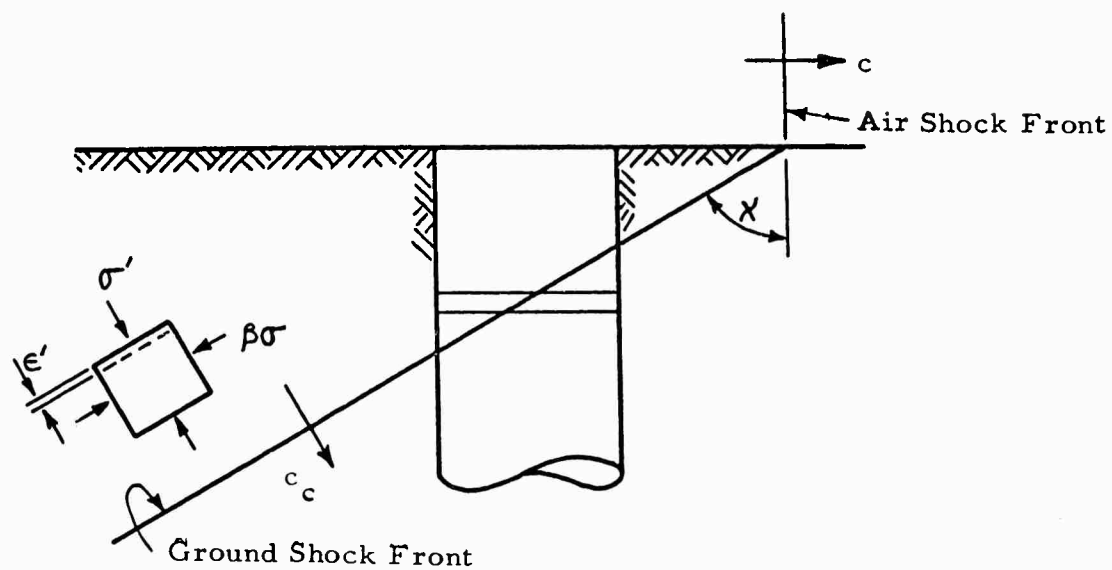
$E_c$  is the modulus of the soil observed in confined compression,

and

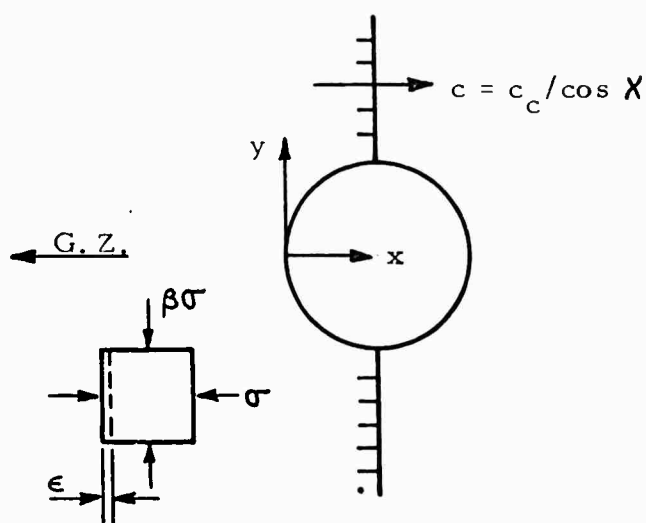
$\rho$  is the density of the soil.

If the value of  $c$  is specified, the angle  $\chi$  is then

ARMOUR RESEARCH FOUNDATION OF ILLINOIS INSTITUTE OF TECHNOLOGY

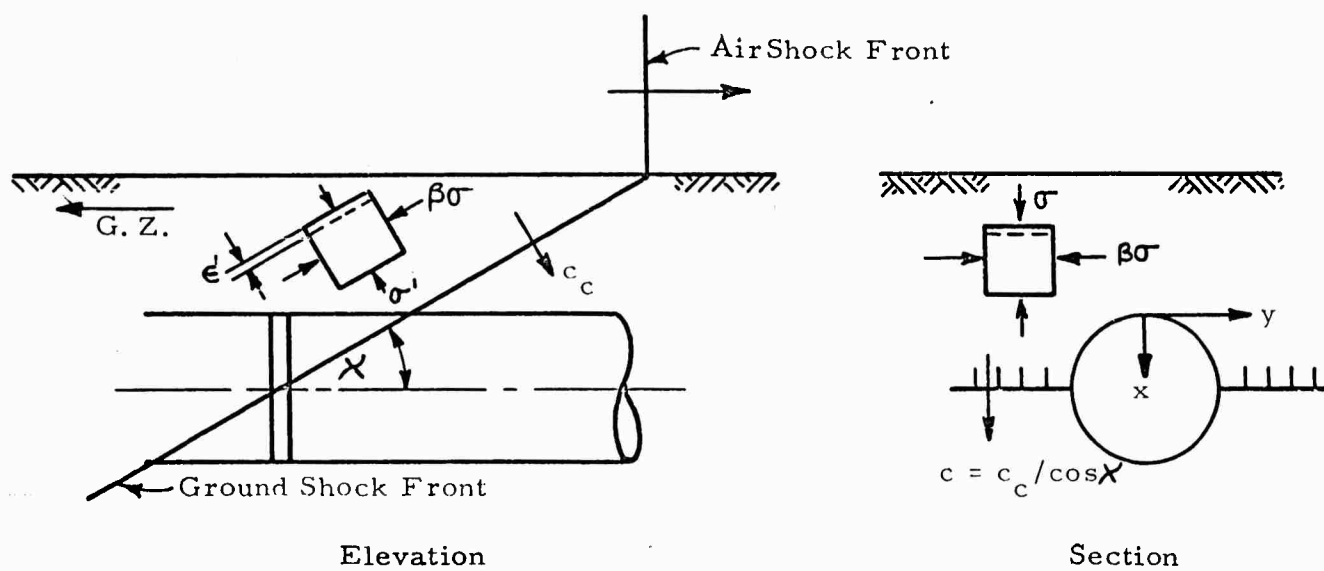


(a) Elevation

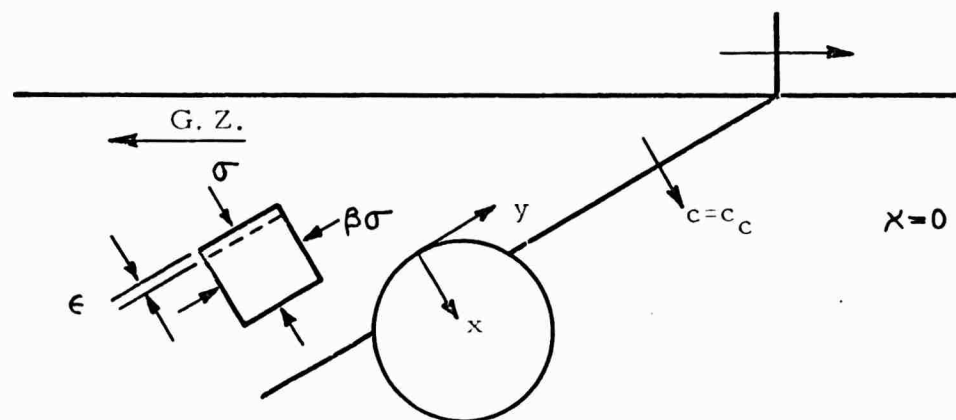


(b) Plan

Fig. 1 SILO STRESS WAVE



(a) End-On Orientation



(b) Side-On Orientation

Fig. 2 TUNNEL STRESS WAVE



$$X = \cos^{-1} \frac{c_c}{c}$$

or

$$X = \cos^{-1} \frac{1}{r}$$

where

$$r = \frac{c}{c_c}.$$

Now for a specified value of the biaxiality ratio ( $\beta$ ) the stress in the direction of propagation of the compression wave ( $\sigma'$ ) is related to the stress ( $\sigma$ ) (see Fig. 1) by the formula

$$\sigma' = [\beta + (1 - \beta) r^2] \sigma,$$

while the strain ( $\epsilon$ ) is related to the strain in the direction of the wave ( $\epsilon'$ ) by

$$\epsilon = \epsilon' / r^2$$

The apparent modulus ( $E^*$ ) is then

$$E^* = \frac{\sigma}{\epsilon} = E_c \frac{r^2}{\beta + (1 - \beta) r^2} \quad (2)$$

where the fact that

$$E_c = \frac{\sigma'}{\epsilon'}$$

is used.

Equation 2 shows that it is not possible to account for any desired combination of observed values of  $E^*$ ,  $\beta$ , and  $c$ , by the proposed scheme. Given any two of these quantities, the third may be determined. The degree of success with which the observed values can be fitted by the proposed method depends upon the extent to which they actually represent the effects of the passage of a compression wave.

The stress wave and shell coordinate system in the plane of the cross section are shown in figure 3.

ARMOUR RESEARCH FOUNDATION OF ILLINOIS INSTITUTE OF TECHNOLOGY

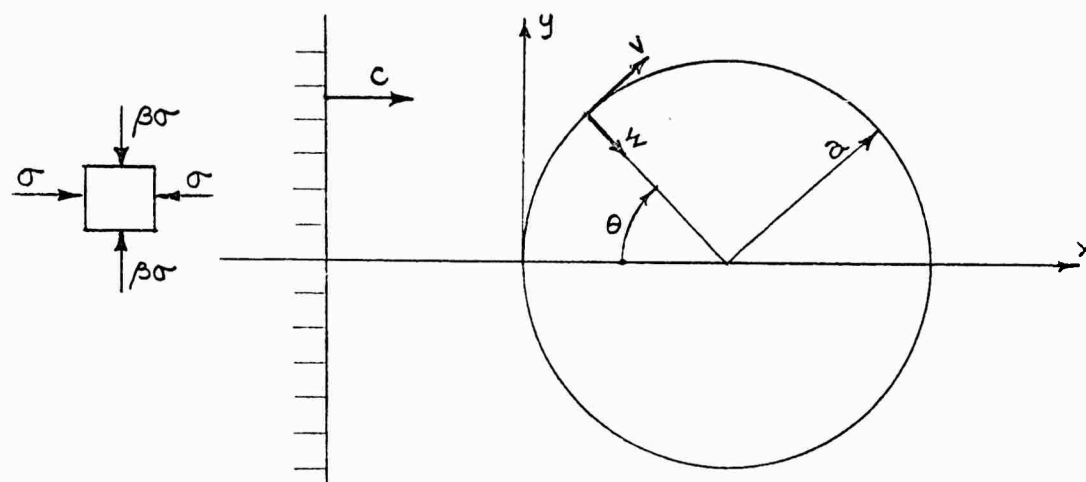


Fig. 3 STRESS WAVE AND SHELL COORDINATE SYSTEM

With reference to the coordinate system shown in the sketch, the variation of the compressive stress in the x-direction is of the form:

$$\left. \begin{aligned} \sigma &= \sigma_0 f(x - ct) && \text{for } x < ct \\ \sigma &= 0 && \text{for } x > ct \end{aligned} \right\} \quad (3)$$

The compressive stress in the y-direction is assumed equal to  $\beta\sigma$  for all values of x, that is, the biaxiality ratio is assumed constant. The strain in the x-direction will be assumed proportional to the stress.

$$\epsilon = \frac{\sigma}{E^*} \quad (4)$$

The displacement in the positive  $x$ -direction of a particle originally at  $x$  is, for small strains,

$$u(x) = \int_x^{ct} \epsilon(x) dx$$

or using equations 3 and 4,

$$u(x) = \frac{\sigma_0}{E^*} \int_x^{ct} f(x - ct) dx \quad (5)$$

The inward radial free-field displacement of particles originally on the surface of the cylinder is then

$$w_0 = u \cos \theta, \text{ for } \cos \theta \geq 1 - \tau$$

where

$$\tau = \frac{ct}{a}$$

Replacing  $u$  by its value from equation 5,

$$w_0 = \frac{\sigma_0 \cos \theta}{E^*} \int_{a(1 - \cos \theta)}^{ct} f(x - ct) dx, \cos \theta \geq 1 - \tau \quad (6a)$$

$$w_0 = 0, \cos \theta < 1 - \tau \quad (6b)$$

The inward radial velocity of a particle is

$$\dot{w}_0 = \frac{c\sigma_0 \cos \theta}{E^*} \left\{ f(0) - \int_{a(1 - \cos \theta)}^{ct} f'(x - ct) dx \right\}, \cos \theta \geq 1 - \tau \quad (7a)$$

where

$$f'(x - ct) = \frac{df}{d(x - ct)}$$

$$\dot{w}_0 = 0, \cos \theta < 1 - \tau \quad (7b)$$

ARMOUR RESEARCH FOUNDATION OF ILLINOIS INSTITUTE OF TECHNOLOGY

The radial component of the free-field stress is

$$\sigma_{rr} = \frac{\sigma}{2} \left[ 1 + \beta + (1 - \beta) \cos 2\theta \right], \cos \theta \geq 1 - \tau$$

or using equation 3

$$\sigma_{rr} = \frac{\sigma_0}{2} \left[ 1 + \beta + (1 - \beta) \cos 2\theta \right] f(x - ct), \cos \theta \geq 1 - \tau \quad (8a)$$

$$\sigma_{rr} = 0, \cos \theta < 1 - \tau \quad (8b)$$

Equations 6, 7, and 8 give the radial components of the free-field displacement, particle velocity, and stress in terms of a general pulse shape,  $f(x - ct)$ . The particular pulse shape that will be considered in this study is one which rises linearly to a constant value (see Fig. 4). This pulse is defined as follows:

$$f(x - ct) = \begin{cases} 0, & x < ct \\ \frac{ct - x}{ct}, & c(t - t_1) \leq x \leq ct \\ 1, & x < c(t - t_1) \end{cases}$$

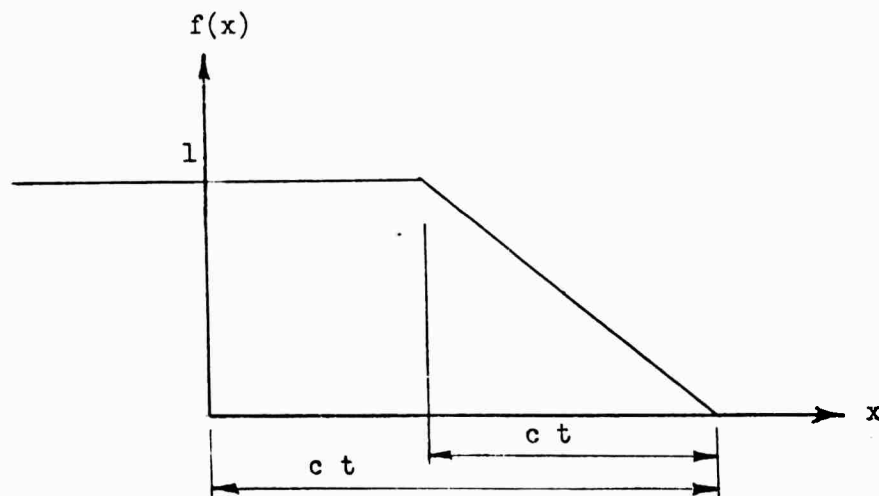


Fig. 4 PULSE WITH LINEAR RISE

ARMOUR RESEARCH FOUNDATION OF ILLINOIS INSTITUTE OF TECHNOLOGY

In discussing the state of affairs as the pulse engulfs the cross section, it is convenient to define the following angles (See Fig. 5)

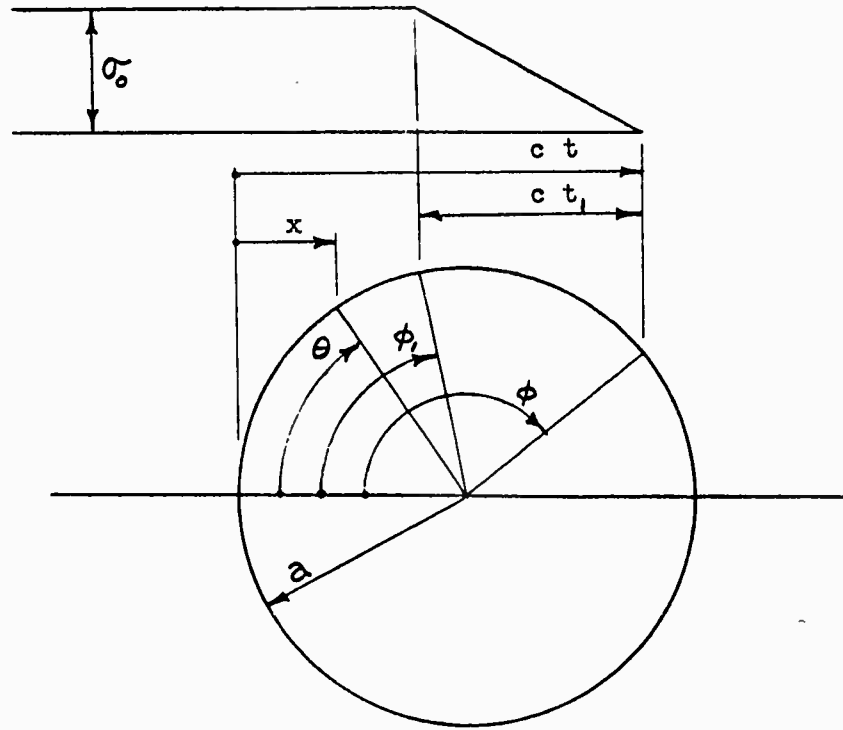


Fig. 5 WAVE FRONT POSITION ANGLES

$$\phi_1 = \begin{cases} \cos^{-1}(1 - \tau + \tau_1), & \tau_1 \leq \tau \leq 2 + \tau_1 \\ \pi & , 2 + \tau_1 \leq \tau \end{cases}$$

$$\phi = \begin{cases} \cos^{-1}(1 - \tau), & 0 \leq \tau \leq 2 \\ \pi & , 2 \leq \tau \end{cases}$$

The general expressions for free-field radial displacement particle velocity, and stress become, for the pulse shape being considered,

Case 1 ( $0 \leq \tau \leq \tau_1$ )

a. for  $-\phi \leq \theta \leq \phi$

$$w_o = \frac{\sigma_o}{E^*} \frac{a \cos \theta}{2 \tau_1} \left[ \cos \theta - (1 - \tau) \right]^2 \quad (9)$$

$$\dot{w}_o = \frac{c \sigma_o}{E^*} \frac{\cos \theta}{\tau_1} \left[ \cos \theta - (1 - \tau) \right] \quad (10)$$

ARMOUR RESEARCH FOUNDATION OF ILLINOIS INSTITUTE OF TECHNOLOGY

$$\sigma_{rr} = \frac{\sigma_o}{2\tau_1} \left[ \cos \theta - (1 - \tau) \right] \left[ 1 + \beta + (1 - \beta) \cos 2\theta \right] \quad (11)$$

b. for  $\phi \leq \theta \leq 2\pi - \phi$

$$w_o = \dot{w}_o = \sigma_{rr} = 0 \quad (12)$$

Case 2 ( $\tau_1 \leq \tau \leq 2 + \tau_1$ )

a. for  $\phi_1 \leq \theta \leq \phi$  and  $2\pi - \phi \leq \theta \leq 2\pi - \phi_1$

Equations 9, 10, and 11 apply

b. for  $\phi_1 \leq \theta \leq 2\pi - \phi$

$$w_o = \dot{w}_o = \sigma_{rr} = 0$$

c. for  $-\phi \leq \theta \leq \phi$

$$w_o = \frac{\sigma_o^a}{E^*} \cos \theta \left[ \cos \theta - (1 - \tau) - \frac{\tau_1}{2} \right] \quad (13)$$

$$\dot{w}_o = \frac{c \sigma_o}{E^*} \cos \theta \quad (14)$$

$$\sigma_{rr} = \frac{\sigma_o}{2} \left[ 1 + \beta + (1 - \beta) \cos 2\theta \right] \quad (15)$$

Case 3 ( $\tau \geq 2 + \tau_1$ )

In this case, equations 13, 14, and 15 apply for all values of  $\theta$ .

The Fourier expansions of  $w_o$ ,  $\dot{w}_o$ , and  $\sigma_{rr}$  have the form

$$w_o = \frac{c_o}{2} + \sum_{n=1}^{\infty} c_n \cos n\theta \quad (16)$$

$$\dot{w}_o = \frac{d_o}{2} + \sum_{n=1}^{\infty} d_n \cos n\theta \quad (17)$$

$$\sigma_{rr} = \frac{b_0}{2} + \sum_{n=1}^{\infty} b_n \cos n \theta \quad (18)$$

where the coefficients  $b_n$ ,  $c_n$ , and  $d_n$  have the following values:

Case 1 ( $0 \leq \tau \leq \tau_1$ )

$$b_n = \frac{\sigma_0}{\pi \tau_1} \left\{ - (1 - \tau) (1 + \beta) S_0(\phi, n) + \left[ \frac{1 + \beta}{2} + \frac{1 - \beta}{4} \right] S_1(\phi, n) \right. \\ \left. - \frac{(1 - \tau)(1 - \beta)}{2} S_2(\phi, n) + \frac{1 - \beta}{4} S_3(\phi, n) \right\} \quad (19)$$

$$c_n = \frac{\sigma_0^a}{E^* \pi \tau_1} \left\{ - (1 - \tau) S_0(\phi, n) + \frac{1}{2} \left[ \frac{3}{4} + (1 - \tau)^2 \right] S_1(\phi, n) \right. \\ \left. - \frac{(1 - \tau)}{2} S_2(\phi, n) + \frac{1}{8} S_3(\phi, n) \right\} \quad (20)$$

$$d_n = \frac{c \sigma_0}{E^* \pi \tau_1} \left\{ S_0(\phi, n) - (1 - \tau) S_1(\phi, n) + \frac{1}{2} S_2(\phi, n) \right\} \quad (21)$$

in which

$$S_0(\phi, n) = \frac{\sin n \phi}{n}, \quad n \neq 0$$

$$S_0(\phi, n) = \phi, \quad n = 0$$

and

$$\left. \begin{aligned} S_1(\phi, n) &= \frac{\sin(n-1)\phi}{n-1} + \frac{\sin(n+1)\phi}{n+1}, \quad n \neq 1 \\ S_1(\phi, n) &= \phi + \frac{\sin(n+1)\phi}{n+1}, \quad n = 1 \end{aligned} \right\} \quad i = 1, 2, 3 \quad (22)$$

Case 2 ( $\tau_1 \leq \tau \leq 2 + \tau_1$ )

$$b_n = \frac{\sigma_o}{\pi} \left\{ (1+\beta) s_o(\phi_1, n) + \frac{1-\beta}{2} s_2(\phi_1, n) - (1-\tau)(1+\beta) s'_o(n) \right. \\ \left. \left[ \frac{1+\beta}{2} + \frac{1-\beta}{4} \right] s'_1(n) - \frac{(1-\tau)(1-\beta)}{2} s'_2(n) + \frac{1-\beta}{4} s'_3(n) \right\}, \quad (23)$$

$$c_n = \frac{\sigma_o^a}{\pi E^*} \left\{ s_o(\phi_1, n) - \left[ 1 - \tau + \frac{\tau_1}{2} \right] s_1(\phi_1, n) + \frac{1}{2} s_2(\phi_1, n) \right. \\ \left. - (1-\tau) s'_o(n) + \frac{1}{2} \left[ \frac{3}{4} + (1-\tau)^2 \right] s'_1(n) - \frac{(1-\tau)}{2} s'_2(n) + \frac{1}{8} s'_3(n) \right\} \quad (24)$$

$$d_n = \frac{c \sigma_o}{\pi E^*} \left\{ s_1(\phi_1, n) + s'_o(n) - (1-\tau) s'_1(n) + \frac{1}{2} s'_2(n) \right\} \quad (25)$$

where

$$\left. \begin{aligned} s'_1(n) &= \frac{1}{\tau_1} \left[ s_1(\phi, n) - s_1(\phi_1, n) \right] \text{ For } \tau_1 \neq 0 \\ s'_1(n) &= 0, \text{ For } \tau_1 = 0 \end{aligned} \right\} \quad (26)$$

Case 3 ( $\tau \geq 2 + \tau_1$ )

$$b_n = \sigma_o \left\{ \begin{aligned} 1+\beta, & n=0 \\ 0, & n=1 \\ (1-\beta)/2, & n=2 \\ 0, & n=3, 4, \dots \end{aligned} \right. \quad (27)$$

$$c_n = \frac{\sigma_o^a}{E^*} \left\{ \begin{aligned} 1, & n=0 \\ (\tau - 1 - \tau_1/2), & n=1 \\ 1/2, & n=2 \\ 0, & n=2, 3, \dots \end{aligned} \right. \quad (28)$$

ARMOUR RESEARCH FOUNDATION OF ILLINOIS INSTITUTE OF TECHNOLOGY



$$d_n = \frac{c \sigma_o}{E^*} \begin{cases} 0 & , n = 0 \\ 1 & , n = 1 \\ 0 & , n = 2, 3, \dots \end{cases} \quad (29)$$

The loading normal to the surface of the cylinder can be written as follows:

$$p = \sigma_{rr} + k(w_o - w) + s(\dot{w}_o - \dot{w}) \quad (30)$$

in which  $k$  and  $s$  are factors of proportionality relating relative radial displacement and velocity to load.

Assuming radial displacement of the cylinder in the form

$$w = a_o + \sum_{n=1}^{\infty} a_n \cos n \theta ,$$

the load acting on the cylinder can be expressed as

$$p = \sum_{n=0}^{\infty} p_n \cos n \theta \quad (31)$$

where

$$\left. \begin{aligned} p_o &= \frac{1}{2} \left[ b_o + k(c_o - 2a_o) + s(d_o - 2\dot{a}_o) \right] \\ \text{and} \\ p_n &= b_n + k(c_n - a_n) + s(d_n - \dot{a}_n) , n = 1, 2, \dots \end{aligned} \right\} \quad (32)$$

The coefficients,  $b_n$ ,  $c_n$ , and  $d_n$ , in equation 32 are defined in equation 19 through equation 29 for the various time intervals.

#### D. Equations of Motion

The radial and tangential displacements of the ring are assumed in the form

$$\begin{aligned} w &= a_0(t) + \sum_{n=1}^{\infty} a_n(t) \cos n \theta \\ v &= \sum_{n=1}^{\infty} \frac{a_n(t)}{n} \sin n \theta \end{aligned} \quad (33)$$

where the  $a_n(t)$  are functions of time which are to be determined. The equations for determining these functions can be found by using d'Alembert's principle together with the principle of virtual work.

The intensity of the inertia forces is, in the radial direction

$$-m \ddot{w} = -\frac{m}{2} \ddot{a}_0 - m \left[ \sum_{j=1}^{\infty} \ddot{a}_j \cos j \theta \right],$$

and in the tangential direction

$$-m \ddot{v} = -m \sum_{j=1}^{\infty} \frac{\ddot{a}_j}{j} \sin j \theta.$$

where  $m$  is surface density.

Assuming a virtual displacement,

$$\delta w = \delta a_n \cos n \theta, \quad \delta v = \frac{\delta a_n}{n} \sin n \theta,$$

the work of the inertia forces is found to be

$$\begin{aligned} & -m a \int_0^{2\pi} \ddot{w} \delta w d\theta - m a \int_0^{2\pi} \ddot{v} \delta v d\theta \\ &= -2\pi a m \ddot{a}_0 \delta a_0, \quad n=0 \\ &= -\pi a m \frac{(n^2+1)}{n^2} \ddot{a}_n \delta a_n, \quad n \neq 0. \end{aligned}$$

An expression for the strain energy of a thin ring of thickness (h) is

$$U = \frac{\bar{E} h}{2a} \int_0^{2\pi} \left( \frac{dv}{d\theta} - w \right)^2 d\theta + \frac{\bar{E} I}{2a^3} \int_0^{2\pi} \left( \frac{d^2 w}{d\theta^2} + w \right)^2 d\theta \quad (34)$$

where

$$\bar{E} = \frac{E}{1 - \nu^2} \quad \text{and} \quad (35)$$

$$I = \frac{h^3}{12 a^3} \quad (36)$$

Using the assumed forms for  $w$  and  $v$  given in equation 33,

$$U = \frac{\pi \bar{E} h}{a} a_0^2 + \frac{\pi \bar{E} I}{2a^3} \sum_{n=1}^{\infty} (n^2 - 1)^2 a_n^2 + \frac{\pi \bar{E} I}{a^3} a_0^2$$

or

$$U = \frac{\pi \bar{E} h}{a} \left( 1 + \frac{h^2}{12 a^2} \right) a_0^2 + \frac{\pi \bar{E} I}{2a^3} \sum_{n=1}^{\infty} (n^2 - 1)^2 a_n^2$$

The internal work done on a virtual displacement is

$$\Delta W_1 = - \frac{\partial U}{\partial a_n} \delta a_n$$

therefore,

$$\Delta W_1 = - 2\pi \bar{E} a_0 \frac{h}{a} \left( 1 + \frac{h^2}{12 a^2} \right) \delta a_0, \quad n = 0$$

and

ARMOUR RESEARCH FOUNDATION OF ILLINOIS INSTITUTE OF TECHNOLOGY

$$\Delta W_i = - \frac{\pi \bar{E} I}{a^3} (n^2 - 1)^2 a_n \delta a_n, \quad n \neq 0$$

The work done by the external forces is

$$\delta W_e = a \int_0^{2\pi} p \delta w d\theta,$$

$$\delta W_e = 2\pi a p_0 \delta a_0, \quad n = 0,$$

and

$$\delta W_e = \pi a p_n \delta a_n, \quad n \neq 0.$$

Now from the condition that the work on a virtual displacement is zero it follows that

$$- 2\pi a m \ddot{a}_0 - 2\pi \bar{E} a_0 \frac{h}{a} \left(1 + \frac{h^2}{12 a^2}\right) - 2\pi a p_0 = 0$$

or replacing  $p_0$  by its value from equation 32 we have

$$m \ddot{a}_0 + s \dot{a}_0 + \left[ \bar{E} \frac{h}{a^2} \left(1 + \frac{h^2}{12 a^2}\right) + k \right] a_0 = \frac{1}{2} (b_0 + k c_0 + s d_0) \quad (37)$$

for the equation governing pure radial motion.

In the same way we obtain

$$2m \ddot{a}_1 + s \dot{a}_1 + k a_1 = b_1 + k c_1 + s d_1 \quad (38)$$

as the equation governing rigid body motion

and

$$\frac{m(n^2 + 1)}{n^2} \ddot{a}_n + s \dot{a}_n + \left[ \frac{\bar{E} I}{a^4} (n^2 - 1)^2 + k \right] a_n = b_n + k c_n + s d_n \quad (39)$$

as the equation of motion for  $n > 1$ .

In the last of the above equations the effect of circumferential stress on the bending deflection has been neglected. It is shown in 5 that in the case of a statically loaded ring under a uniform pressure,  $p_o$ , the effect of circumferential stress on bending can be taken into account by the addition of a fictitious pressure equal to

$$-\frac{p_o}{a} \left( \frac{d^2 w}{d\theta^2} + w \right) = \frac{p_o}{a} \sum_{n=2}^{\infty} (n^2 - 1) a_n \cos n \theta. \quad (40)$$

In the present case, dynamic effects will be ignored in determining the uniform component ( $p_o$ ) of the radial pressure. This simplification uncouples the equations of motion. Then from equation 32,

$$p_o = \frac{1}{2} \left[ b_o + k (c_o - 2a_o) \right]$$

in which  $a_o$  is set equal to its value under static loading,

$$a_o = \frac{1}{2} (b_o + k c_o) / \left[ \frac{\bar{E} h}{a^2} \left( 1 + \frac{h^2}{12 a^2} \right) + k \right] \quad (41)$$

This equation is obtained from equation 37 by neglecting the inertia and damping terms. Further simplification is obtained by introducing the approximation that

$$1 + \frac{h^2}{12 a^2} \simeq 1$$

The expression for  $p_o$  then becomes

$$p_o = \frac{1}{2} (b_o + k c_o) / \left( 1 + \frac{k a^2}{\bar{E} h} \right). \quad (42)$$

The work done by the fictitious pressure on a virtual displacement,

$$\delta w = \delta a_n \cos n \theta,$$

is

$$\pi p_o (n^2 - 1) a_n \delta a_n = \pi \frac{(b_o + k c_o)}{2(1 + \frac{k a}{E h})} (n^2 - 1) a_n \delta a_n ,$$

and the modified equation of motion becomes for  $n \geq 1$

$$\begin{aligned} \frac{m(n^2 + 1)}{n^2} \ddot{a}_n + s \dot{a}_n + \left[ \frac{E I}{a^4} (n^2 - 1)^2 + k \right] a_n &= b_n + k c_n + s d_n \\ + \frac{(b_o + k c_o)}{2(1 + \frac{k a}{E h})} (n^2 - 1) \frac{a_n}{a} \end{aligned} \quad (43)$$

Up to the time of complete engulfment, that is, for  $\tau < 2 + \tau_1$ , the equation of motion for the bending modes, equation 43, must be solved by numerical means. After complete engulfment the  $b_n$ ,  $c_n$ , and  $d_n$  are constant (equations 27, 28, and 29), so that solutions in closed form can be obtained.

In terms of the dimensionless displacement and time variables,  $x_n$  and  $\tau$ ,

$$x_n = a_n / a$$

$$\tau = ct/a$$

Equation 43 becomes

$$f_2 x_n'' + f_1 x_n' + f_0 x_n = g, \quad n = 2, 3, \dots \quad (44)$$

where primes indicate differentiation with respect to  $\tau$  and where

$$f_2 = \frac{n^2 + 1}{n^2} \frac{m c^2}{\sigma_o a} \quad (45)$$

$$f_1 = \frac{c s}{\sigma_o} \quad (46)$$

$$f_o = \frac{(n^2 - 1)}{\sigma_o} \left[ \frac{\bar{E} I}{a^3} (n^2 - 1) + \frac{k a}{n^2 - 1} - \sigma_o \frac{1 + \beta + \frac{k a}{E^*}}{2(1 + \frac{k a^2}{E h})} \right] \quad (47)$$

and

$$\left. \begin{aligned} g &= \frac{1}{2} (1 - \beta + \frac{k a}{E^*}) , \quad n = 2 \\ g &= 0 , \quad n > 2 \end{aligned} \right\} \quad (48)$$

The character of the solution differs depending on whether or not  $f_o > 0$ . For sufficiently large values of  $\sigma_o$ ,  $f_o$  becomes negative and the displacements grow without bound, buckling occurs. Since yielding under hoop compression occurs before the buckling load is reached, this case is of little importance. For values of  $f_o > 0$  the solutions are either oscillatory or overdamped depending upon whether the quantity  $f_1^2 / 4 f_o f_2$  is less than unity. There are three cases:

Case 1 ( $f_1^2 < 4 f_o f_2$ ) Underdamped

$$x_n = \left\{ (\bar{x}_n - x_{n_s}) \cos \Psi(\tau - 2 - \tau_1) \frac{1}{\Psi} \left[ \bar{x}'_n - \xi(\bar{x}_n - x_{n_s}) \right] \right. \\ \left. \sin \Psi(\tau - 2 - \tau_1) \right\} e^{\xi(\tau - 2 - \tau_1)} x_{n_s} \quad (49)$$

Case 2 ( $f_1^2 > 4 f_o f_2$ ) Overdamped

$$x_n = \frac{1}{2\eta} \left[ (\xi + \eta)(\bar{x}_n - x_{n_s}) - x'_n \right] e^{(\xi - \eta)(\tau - 2 - \tau_1)} \\ - \frac{1}{2\eta} \left[ (\xi - \eta)(\bar{x}_n - x_{n_s}) - x'_n \right] e^{(\xi + \eta)(\tau - 2 - \tau_1)} + x_{n_s} \quad (50)$$

Case 3 ( $f_1^2 = 4 f_o f_2$ ) Critically Damped

$$x_n = \left\{ (\bar{x}_n - x_{n_s}) + \left[ \bar{x}'_n - \xi(\bar{x}_n - x_{n_s}) \right] (\tau - 2 - \tau_1) \right\} e^{\xi(\tau - 2 - \tau_1)} x_{n_s} \quad (51)$$

where

$$\xi = -f_1/2f_2$$

$$\psi = \sqrt{\frac{f_o}{f_2} - \xi^2}$$

$$\eta = \sqrt{\xi^2 - \frac{f_o}{f_2}}$$

$$x_{ns} = g/f_o$$

and

$$\bar{x}_n = x_n \text{ at } \tau = 2 + \tau_1$$

$$\bar{x}'_n = x'_n \text{ at } \tau = 2 + \tau_1$$

The value  $x_{ns}$  is the peak static displacement of the  $n^{\text{th}}$  mode. Since  $g = 0$  for  $n > 2$  the first bending mode ( $n = 2$ ) has the only non-zero static displacement.

The critical value of damping at which the motion loses its oscillatory character is given by the condition

$$f_1^2 = 4 f_o f_2$$

In this case

$$s_{cr} = 2 \left\{ \frac{n^2 + 1}{n^2} - \frac{m}{a} (n^2 - 1) \left[ \frac{E I}{a^3} (n^2 - 1) + \frac{k a}{n^2 - 1} \right. \right. \\ \left. \left. - \sigma_o \frac{1 + \beta + \frac{k a}{E^*}}{2 \left( 1 + \frac{k a^2}{E h} \right)} \right]^{1/2} \right\} \quad (52)$$



The term involving  $\sigma_0$  in equation 52 derives from the term that was added to equation 39 to account for the effect of direct stress on bending. When this effect is negligible the value of  $s_{cr}$  increases with increasing mode number. When the direct stress nears the buckling stress, the quantities in the brackets in equation 52 reaches a minimum for a value of  $n \geq 2$  and  $s_{cr}$  can first decrease then increase with increasing  $n$ . In any case, for  $n$  sufficiently large, the effect of damping diminishes.

#### E. Selection of Parameter Values

Before the method can be applied to the investigation of the dynamic effects of blast-induced loads, values must be assigned to the constant  $k$  and  $s$  which relate changes in load to relative displacement and velocity, and values must be assumed for the virtual mass.

Static load tests on culverts ranging from 30 to 84 inches in diameter indicate that the foundation modulus ( $k$ ) is a function of the radius (3). Values of the quantity  $ka$  where  $a$  is the radius of the cylinder seem to be constant for a given soil condition. Values of  $ka \geq 200$  psi are cited in reference 3 for various types of backfill. Values of the compression moduli and density of the fill material are not given so it is difficult to relate the observed values of the foundation modulus to other soil properties.

Watkins (4) obtained values of  $ka$  ranging from about 2300 to 3700 psi for various mixtures of silt and clay. These results were obtained from tests on 3-7/8-in. diameter cylinders. Increasing values of  $ka$  were found with increasing density of the soil, so that apparently  $ka$  increases with increasing values of the compression modulus.

The plane strain solution for the displacements produced by the application of a radial pressure varying as  $\cos n \theta$  to the boundary of a hole in an infinite elastic medium is given in Appendix B as follows

$$ka = \frac{n^2 - 1}{2n + 1} E_c, \quad n \geq 2 \quad (53)$$

Thus, for an elastic medium, the foundation modulus increases with increasing mode number and is directly proportional to the modulus in confined compression.

If a similar solution is obtained for  $n=1$  (rigid body displacement), the foundation modulus is found to be zero. That is, there is no resistance to the displacement of a hole as a rigid body in an infinite elastic medium. For this reason, a zero value for the foundation modulus is used in the computation of the rigid body motion ( $n=1$ ). A fixed value of  $ka$ , equal to some fraction of  $E_c$ , is used in the computations described in the following subsection for all other values of  $n$  since there is no basis for estimating what the variation with  $n$  should be for soils.

There is no experimental data on which to base the selection of the value of  $s$ , the constant of proportionality relating changes in load to relative velocity. The choice of  $s$ , determines the magnitude of the jump in pressure at the head on point ( $\phi = 0$ ) at  $t=0$ . There is, as yet, no evidence that such reflection effects exist in soils; however, for an elastic medium, the reflected pressure would be twice the incident pressure for the case of normal incidence of a compression wave. To obtain this result from the analysis presented here, a value of

$$s = \rho c_c \text{ (Elastic Medium)} \quad (54)$$

would be required. Selected values of the parameter,  $s$ , used in this analysis are taken as less than the value for an elastic medium, i.e.,  $\frac{s}{\rho c_c} < 1.0$ .

It is shown in reference 6 that, in the analysis of the response of a cylindrical shell submerged in an incompressible fluid, the interaction between the fluid and the shell can be completely accounted for by the addition of a virtual mass to the actual mass of the shell. This virtual mass is given by the formula

$$m_{v_n} = \rho a \frac{n}{n^2 + 1} \quad (55)$$

where  $\rho$  is the density of the soil,  $a$  is the radius of the cylinder, and  $n$  is the displacement mode. It seems plausible to suppose that the use of some fraction of this virtual mass is appropriate for an underground structure. In the computations described in the following section, a mass equal to  $K_{m_v}$  times  $m_{v_n}$  is added to the actual mass of the shell, where the factor  $K_{m_v}$  is between zero and unity.

ARMOUR RESEARCH FOUNDATION OF ILLINOIS INSTITUTE OF TECHNOLOGY

## F. Results of the Analysis

It is clear that the utility of the proposed method for the analysis of the response of silo and tunnel linings to blast-induced loadings can be established only by demonstrating agreement between predictions of the method and experimental results. There is, at this time, no data that can be used for this purpose. It is expected that tests will be carried out in the near future to check the theory.

In the interim, something is to be gained by an investigation of the nature of the solutions given by the method and by the study of the effects on these solutions of variations in the parameters whose values at this time are more or less indeterminate. Although it is not possible to assign precise values to the parameters on which the solution depends, it may prove that for wide variations in their values the stresses remain within certain limits. In this way it may be possible to draw useful conclusions concerning the significance of dynamic effects. In other words, it may be possible to show that with the application of an appropriate factor to account for dynamic effects, an analysis for static loading is adequate for design.

A further reason for investigating solutions given by the method is that, in this way, a fairly accurate knowledge of the relative effects of variations in the flexibility of the structure can be obtained. The effects of variation in wall thickness in a concrete cylinder and variations in the parameter (s) were considered in the first interim report on this program (7). However, the results suffer from the fact that the value of the apparent modulus  $E^*$  used in the three cases considered did not satisfy the requirement contained in equation 2. Since too low a value of  $E^*$  was used, the results exaggerate the dynamic effects.

In the present report, typical examples of curves of displacement, pressure, and stress-versus-time are presented. Because these are the quantities that will be measured in any future experimental investigations, it is of interest to note the characteristics of the response predicted by the theory. No attempt has been made to study completely the effects of variations in the parameters entering into the solution.

ARMOUR RESEARCH FOUNDATION OF ILLINOIS INSTITUTE OF TECHNOLOGY

Solutions were obtained for 31 cases listed in table 1 which are intended to be representative of a tunnel oriented side-on to the direction of the compression wave propagation (see Fig. 2). Solutions for seven additional cases listed in table 2 that are representative of a silo (see Fig. 1) have also been obtained. Six displacement modes ( $n = 0$  through 5) have been included in the solutions. The numerical integration was performed on the Foundation's UNIVAC 1105, Remington Rand Computer. The computer program is given in Appendix C.

#### 1. Tunnel Cases (Side-On Orientation)

Variations in the values of  $ka$ , the virtual mass,  $s$ ,  $\tau_1$  and the ratio of radius to thickness,  $a/h$  were considered. The following fixed values were used for the other constants.

$$\sigma_0 = 200 \text{ psi}$$

$$\beta = 1/3$$

$$E^* = E_c = 21,600 \text{ psi}$$

$$c = c_c = 1,000 \text{ fps}$$

$$\rho = 1.5 \times 10^{-4} \text{ lb-sec}^2\text{-in.}^{-4}, \text{ soil density (100 pcf)}$$

$$\rho_s = 2.25 \times 10^{-4} \text{ lb-sec}^2\text{-in.}^{-4}, \text{ density of shell material (concrete)}$$

$$\bar{E} = 3 \times 10^6 \text{ psi (appropriate for concrete)}$$

The compression modulus is in the range of values for representative soils and a biaxiality ratio ( $\beta$ ) equal to one-third is justifiable for the side-on orientation since this value of lateral pressure to applied normal pressure is commonly used for a wide variety of soils.

Three values of  $ka$  equal to 5000, 2000 and 500 psi were used. These variations cover the extremes of the range of values given in references 3 and 4. Values of the quantity  $\frac{s}{\rho c_c}$  equal to 0, 0.125, 0.25, and 0.5 were used to investigate the effects of variations in  $s$  while values of  $K_{m_v}$  equal to zero and one-half were used to study the effects of variations of virtual mass. Values of  $a/h$  equal to 30, 20 and 10 were used to examine the effect of thick-

ness variations. These ratios represent wall thicknesses of 6, 9 and 18 inches respectively for a tunnel radius of 15 feet. Constant values of  $s/\rho c_c$  equal to 0.125 and  $K_{m_v}$  of 0.5 were selected for the  $a/h$  variation. The majority of the solutions were obtained for a step-pulse loading ( $\tau_1 = 0$ ); however, the effect of a rise time equal to one transient time of the stress wave ( $\tau_1 = 2$ ) was considered for each  $ka$  with fixed values of  $K_{m_v} = 1/2$ ,  $s/\rho c_c = 1/8$  and  $a/h = 10$ . For a tunnel radius of 15 feet the rise time,  $t_1$ , equals 30 msec.

Typical curves of pressure, relative displacement, and maximum combined stress-versus-time are given in figure 6a, b and c. The peak values of these quantities and the times of their occurrence are listed in table 1. Curves of velocity-versus-time for rigid body response are shown in figure 7.

## 2. Silo Cases

Two values each of  $ka$ ,  $\sigma_0$  and  $c$  were considered. A concrete lining with ~~two~~ ratios of radius to thickness and a single steel lining were studied. Fixed values of constants for all cases were

$$K_{m_v} = 0.5$$

$$c_c = 1000 \text{ fps}$$

$$\tau_1 = 0.0$$

$$s/\rho c_c = 0.25$$

$$\rho = 1.5 \times 10^{-4} \text{ lb} - \text{sec}^2 - \text{in}^{-4}$$

$$\beta = 1.0$$

$$E_c = 21,600 \text{ psi}$$

and

$$\rho_s = \begin{cases} 2.25 \times 10^{-4} \text{ lb} - \text{sec}^2 - \text{in}^{-4}, & \text{concrete shell} \\ 7.35 \times 10^{-4} \text{ lb} - \text{sec}^2 - \text{in}^{-4}, & \text{steel shell} \end{cases}$$

$$\bar{E} = \begin{cases} 3 \times 10^6 \text{ psi}, & \text{concrete shell} \\ 30 \times 10^6 \text{ psi}, & \text{steel shell} \end{cases}$$

Table 1

## MAXIMUM DISPLACEMENT, STRESS, AND PRESSURE FOR TUNNEL CASES (Side-On Orientation)

Case	k <sub>a</sub> (psi)	K <sub>m<sub>v</sub></sub>	s pc	a h	Max Relative Displacement		Max Combined Stress		Max Press. Ratio			
					τ <sub>1</sub>	Static × 2	D. L. F. ⊕ τ <sub>max</sub>	Static** f <sub>D</sub> + f <sub>B</sub> C <sub>0</sub> θ=0	D. L. F. ⊕ τ <sub>max</sub>	Σ <sup>5</sup> p <sub>n</sub> σ <sub>0</sub> 0	τ <sub>max</sub>	
1	5000	0	0.5	10	0	.01323	.98	* 5.8	.98	* 5.6	1.44	.1
2			0.25				1.06	4.9	1.06	5.0	1.29	.1
3			0.125				1.11	4.8	1.22	3.2	1.20	.1
4			0.06				1.24	3.2	1.67	3.2	1.15	.2
5		0.5	0.5				1.04	6.1	1.03	6.2		
6			0.25				1.21	5.2	1.16	5.1		
7			0.125				1.36	5.0	1.35	5.1	1.24	.2
8			0.06				1.63	5.0	1.66	5.0		.2
9			0.125				1.24	4.7	1.10	3.8	1.20	.1
10			0.06				1.25	4.9	1.12	5.0	1.21	.2
11	5000	0.5	0.125	10	0	.01323	1.36	5.0	1.35	5.1	1.24	.2
12	2000	0	0.125	10	2.0	.01323	1.31	6.1	1.13	6.4	1.03	2.0
13			0.06				1.03	6.1	1.03	6.1	1.27	.1
14		0.5	0.125	10		.01985	1.16	5.0	1.26	5.0	1.19	.2
15			0.06				1.39	4.2	1.60	5.0	1.13	.2
16		0.5	0.125	10		.01985	1.16	6.4	1.16	6.3	1.32	.1
17			0.06				1.39	6.2	1.40	6.2	1.23	.2
18			0.125	10		.01985	1.81	6.1	1.88	6.2	1.44	.2
19			0.06			.04563	1.21	7.7	1.13	7.2	1.20	.1
20	2000	0.5	0.125	10	0	.04084	1.21	8.0	1.11	9.2	1.20	.1
21	500		0.06			.01985	1.39	6.2	1.40	6.2	1.23	.2
22			0.125	10	2	.01985	1.35	7.2	1.32	7.1	1.01	2.0
23		0.5	0.06			.02943	.89	9.9	.90	9.9	1.44	.1
24			0.125	10			.98	* 9.8	.98	* 9.8	1.28	.1
25		0.5	0.06				1.14	6.1	1.15	6.1	1.19	.1
26			0.125	10			1.74	5.1	1.80	5.1	1.13	.2
27		0.5	0.06				.91	9.9	.91	9.9	1.53	.1
28			0.125	10		.02943	1.09	8.8	1.08	8.8	1.32	.1
29		0.5	0.06			.3866	1.32	7.4	1.31	7.4	1.22	.2
30			0.125	10		.1836	1.34	7.2	1.85	6.4	1.13	.2
31	500	0.5	0.125	10	2	.02943	.411	9.2	.492	9.9	1.19	.1
						.02943	.671	9.9	.691	9.9	1.20	.1
						.02943	1.32	7.4	1.31	7.4	1.22	.2
						.02943	1.31	8.5	1.27	8.1	1.00	2.0

\* Time when response value attained 98% of static value. (This time is given when curve is approaching static value asymptotically since it is difficult to determine when D. L. F. = 1)

\*\* See equations 57 and 58.

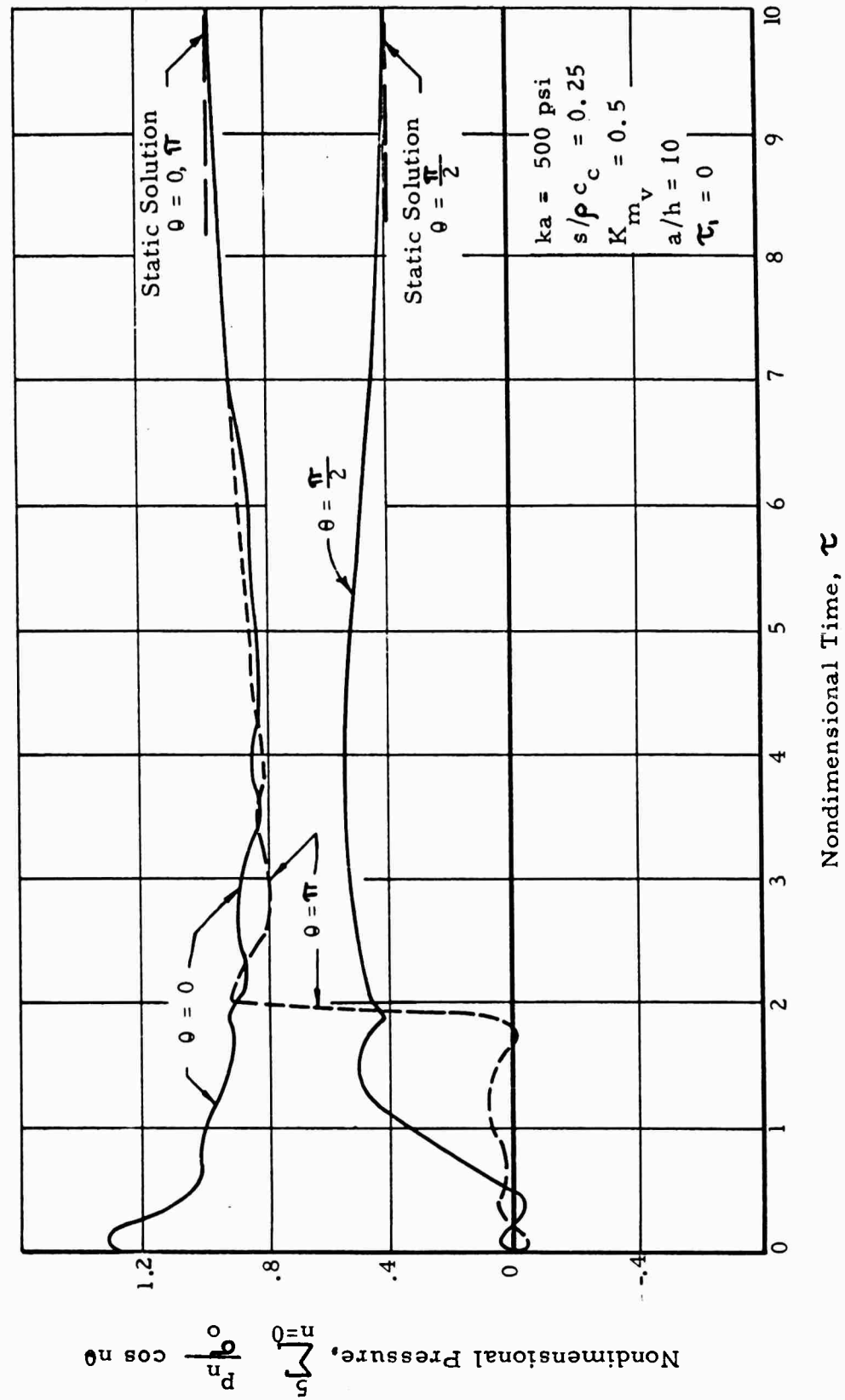


Fig. 6a PRESSURE-TIME VARIATION (CASE 26)

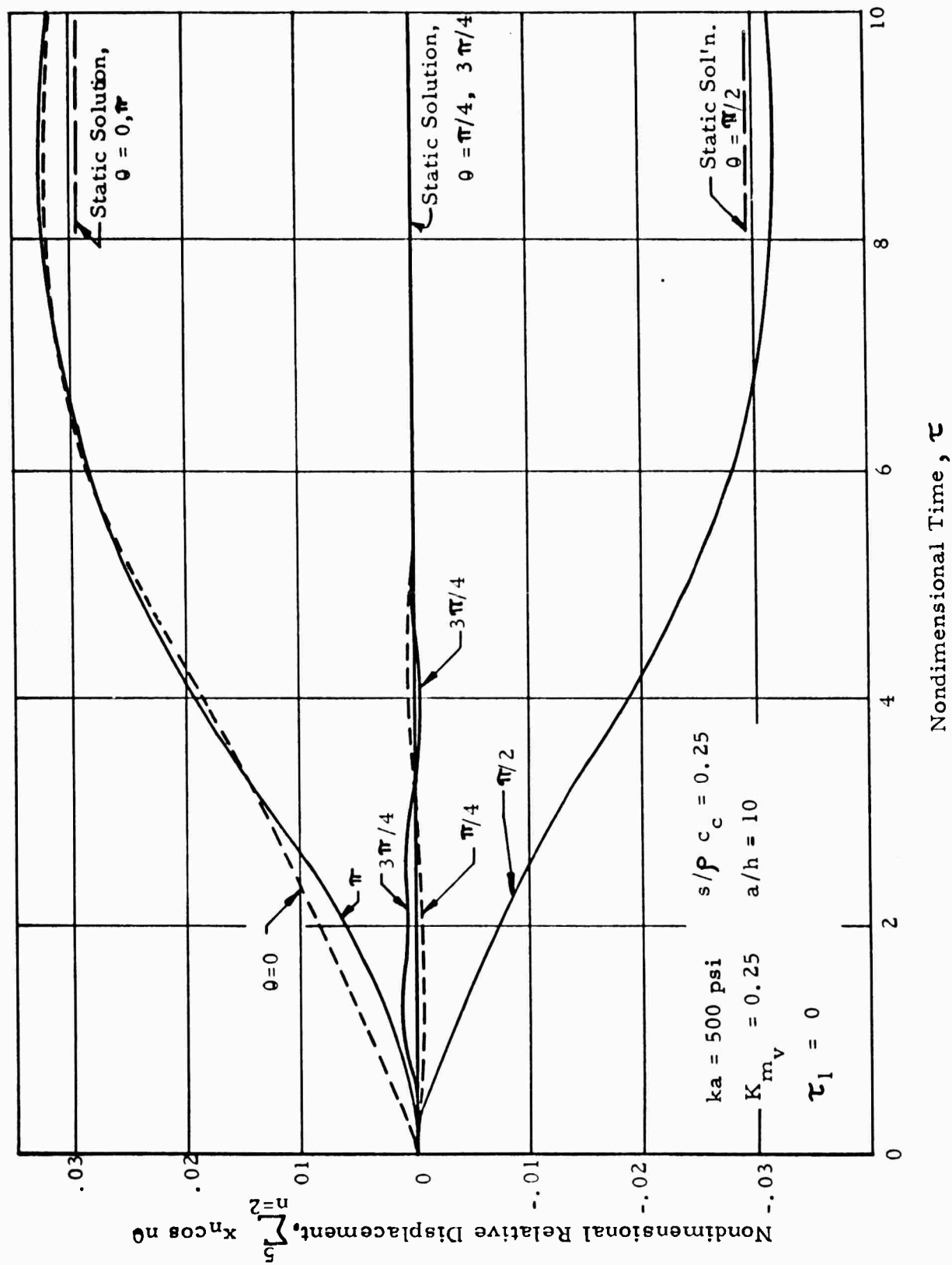


Fig. 6b RELATIVE DISPLACEMENT - TIME VARIATION (CASE 26)



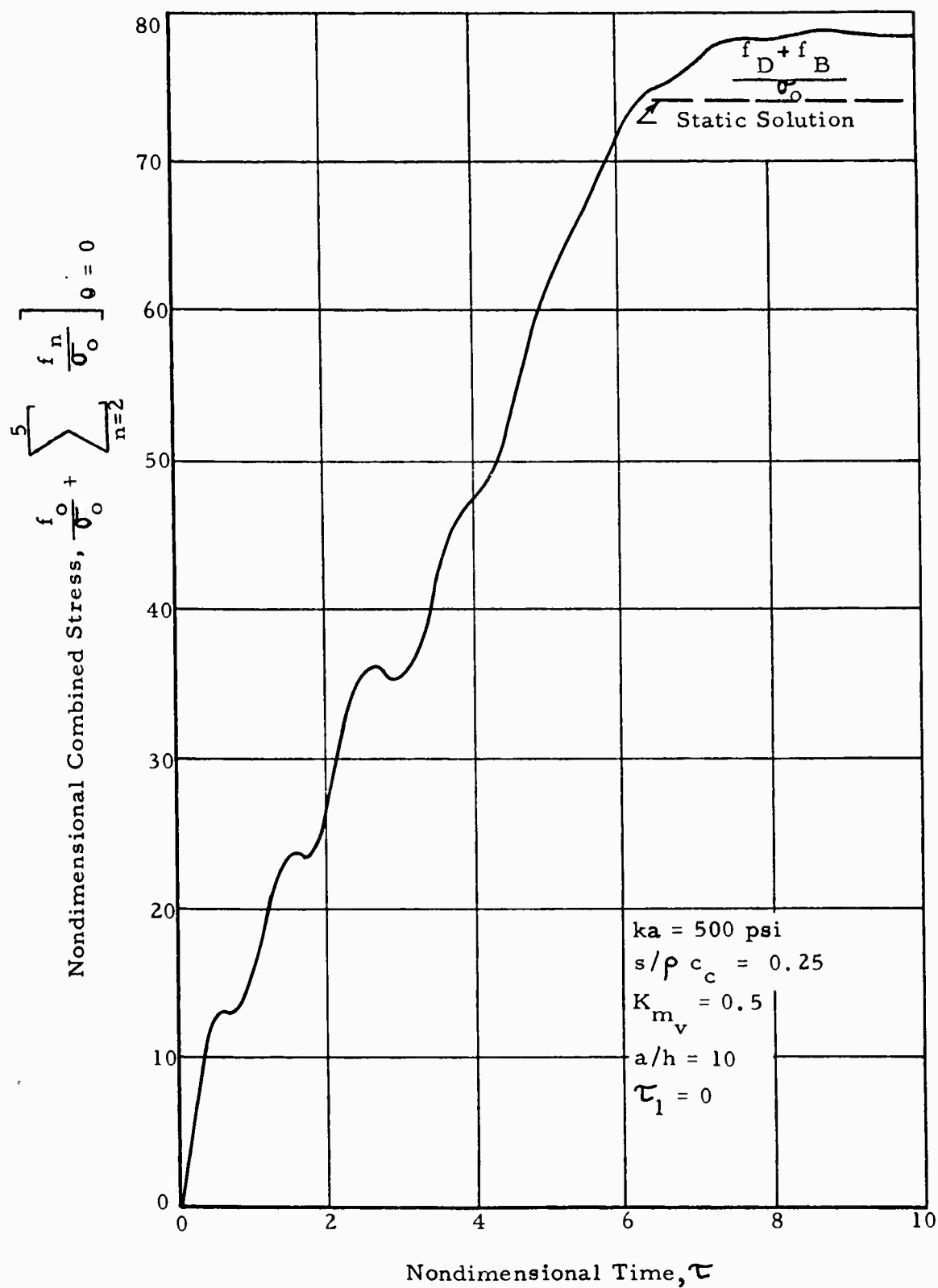


Fig. 6c COMBINED STRESS-TIME VARIATION (CASE 26)

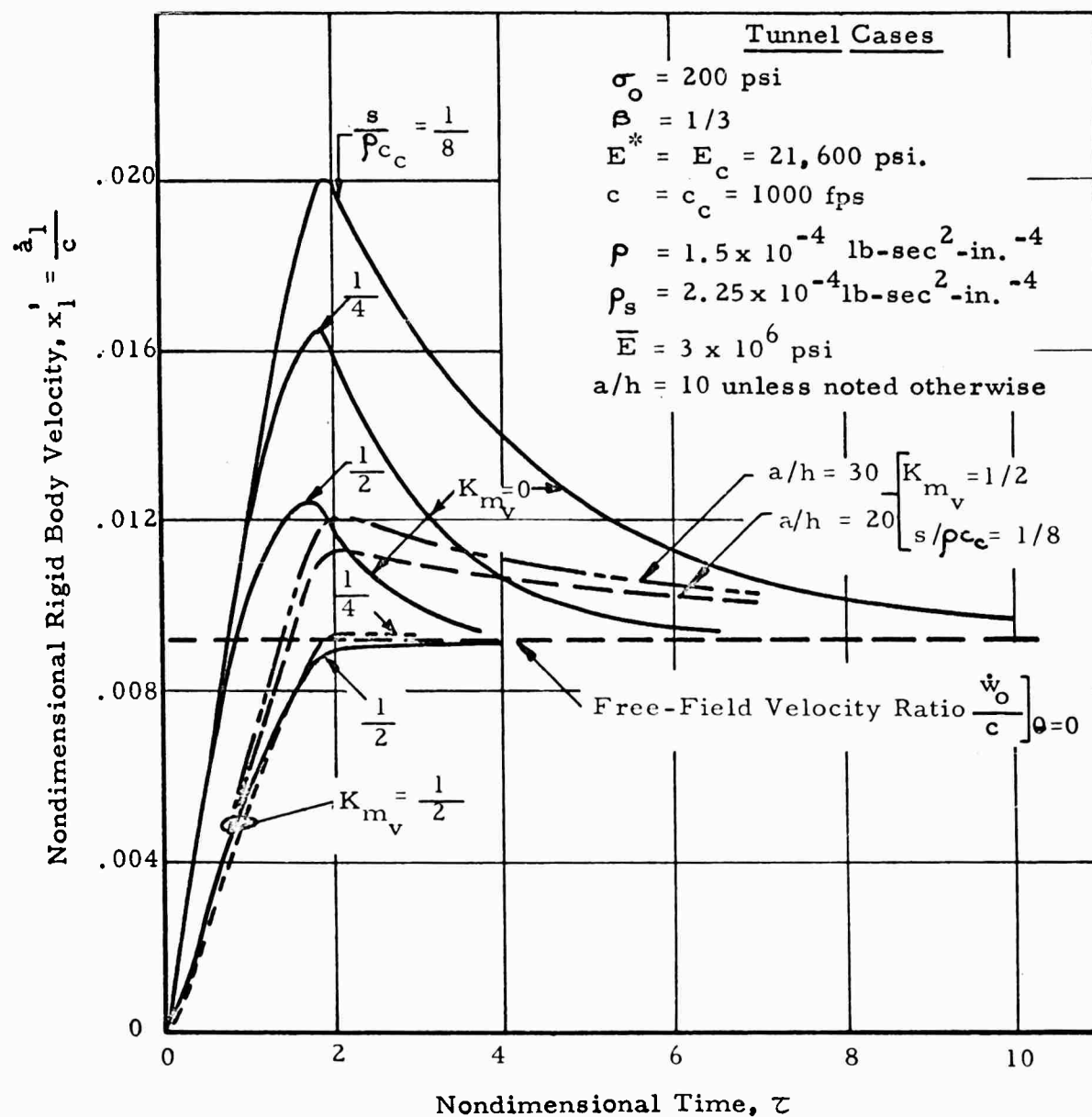


Fig. 7 VELOCITY-TIME VARIATION (TUNNEL)

Table 2

MAXIMUM DISPLACEMENT, STRESS AND PRESSURE FOR SILO CASES

Case	Shell Material	E* (psi)	$\frac{a}{h}$	c (fps)	ka (psi)	$\sigma_o$ (psi)	Max Relative Displacement		Max Combined Stress		Max Press. Ratio	
							Static $x_2^{**}$	D. L. F. @ $\tau_{max}$	Static $\frac{f_D + f_B}{\sigma_o}^{**}$	D. L. F. @ $\tau_{max}$	$\sum_{o=1}^5 \frac{P_n}{\sigma_o}$ @ $\tau_{max}$	$\tau_{max}$
32	I	$5 \times 10^5$	10	4810	5000	200	.0001502	1.35	10.22	1.01	1.202	.2
33	*				5000	100	.00007191	1.42	10.21	1.01	1.202	.2
34					500	200	.0000465	4.32	10.09	1.04	1.204	.2
35	Concrete	$5 \times 10^5$		4810		100	.00002041	4.99	10.08	1.04	1.204	.2
36		86,400	10	2000		200	.000269	4.73	10.62	1.17	1.245	.2
37	I		20				.00319	.460	23.59	.91	1.247	.2
38	Steel	86,400	60	2000	500	200	.1909	.0076	775.9	.0835	1.204	.2

\*\* See Equations 57 and 58

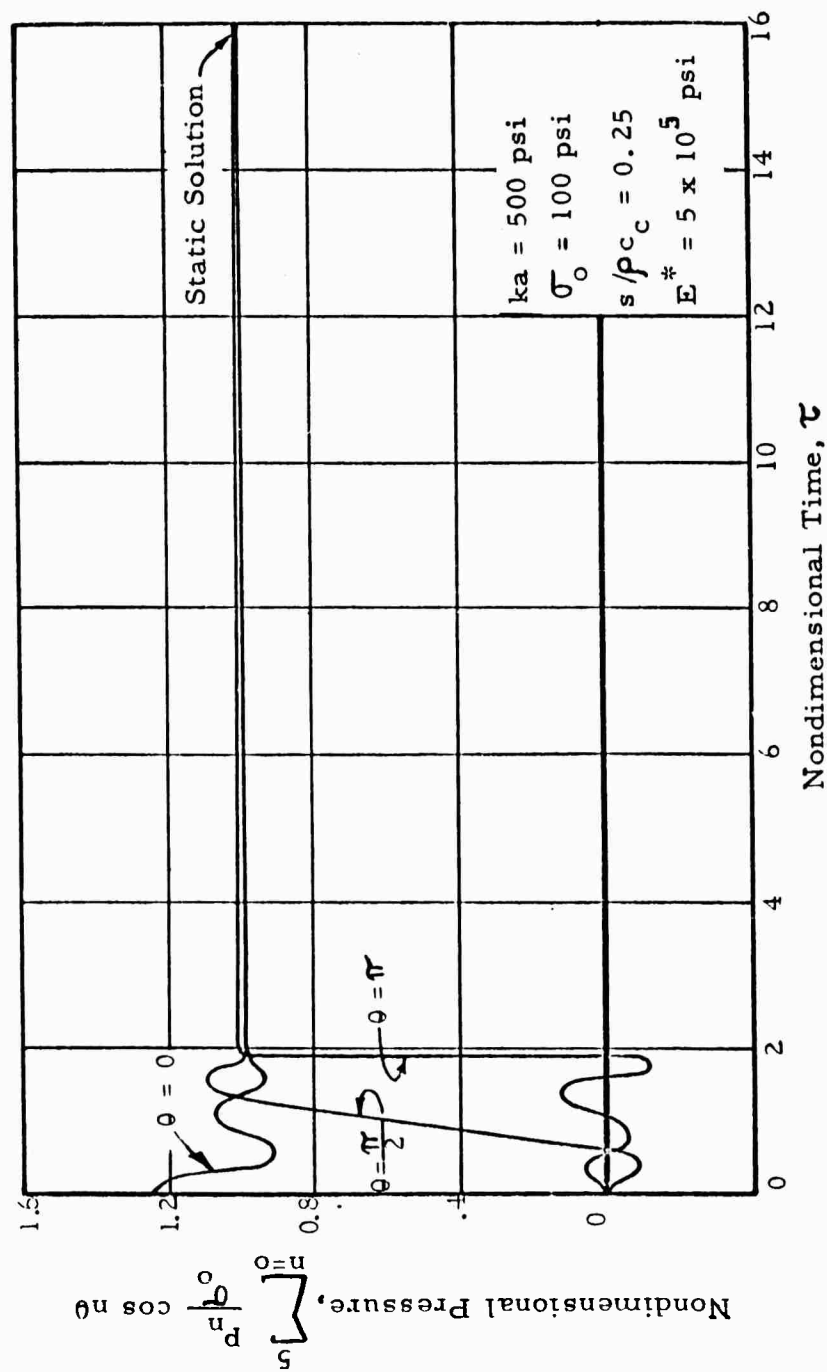


Fig. 8a PRESSURE-TIME VARIATION (CASE 35)

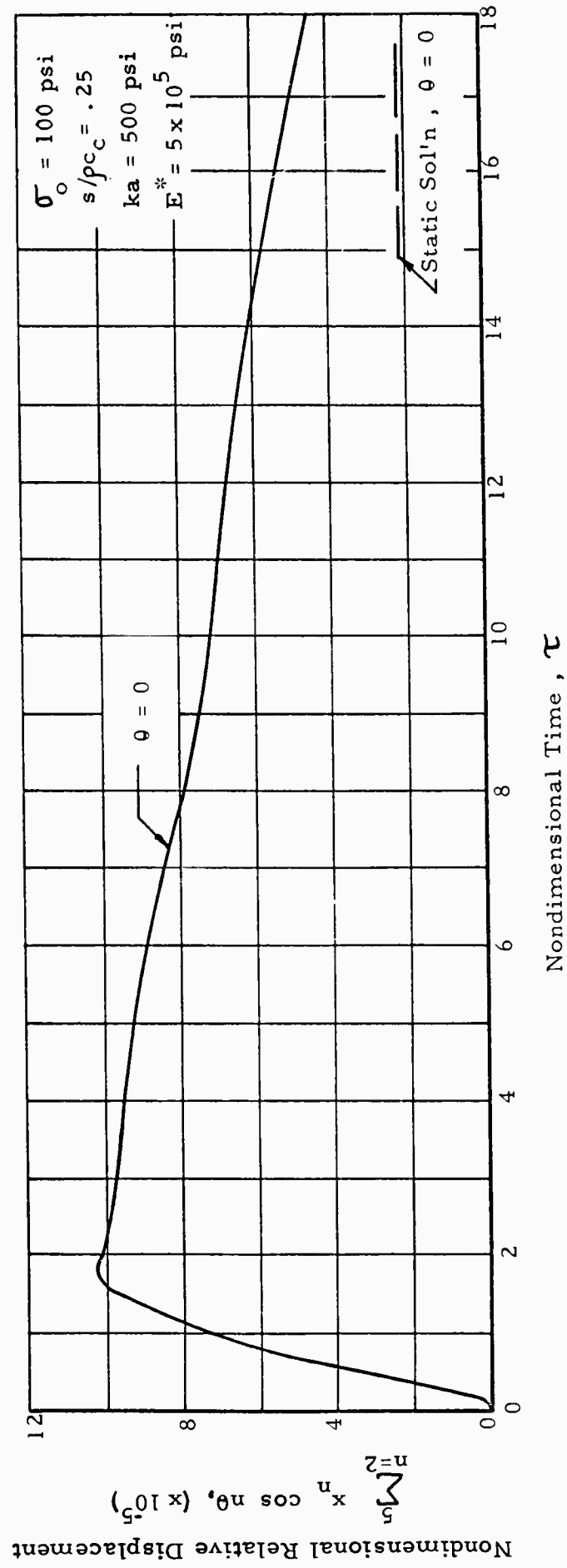


Fig. 8b RELATIVE DISPLACEMENT-TIME VARIATION (CASE 35)

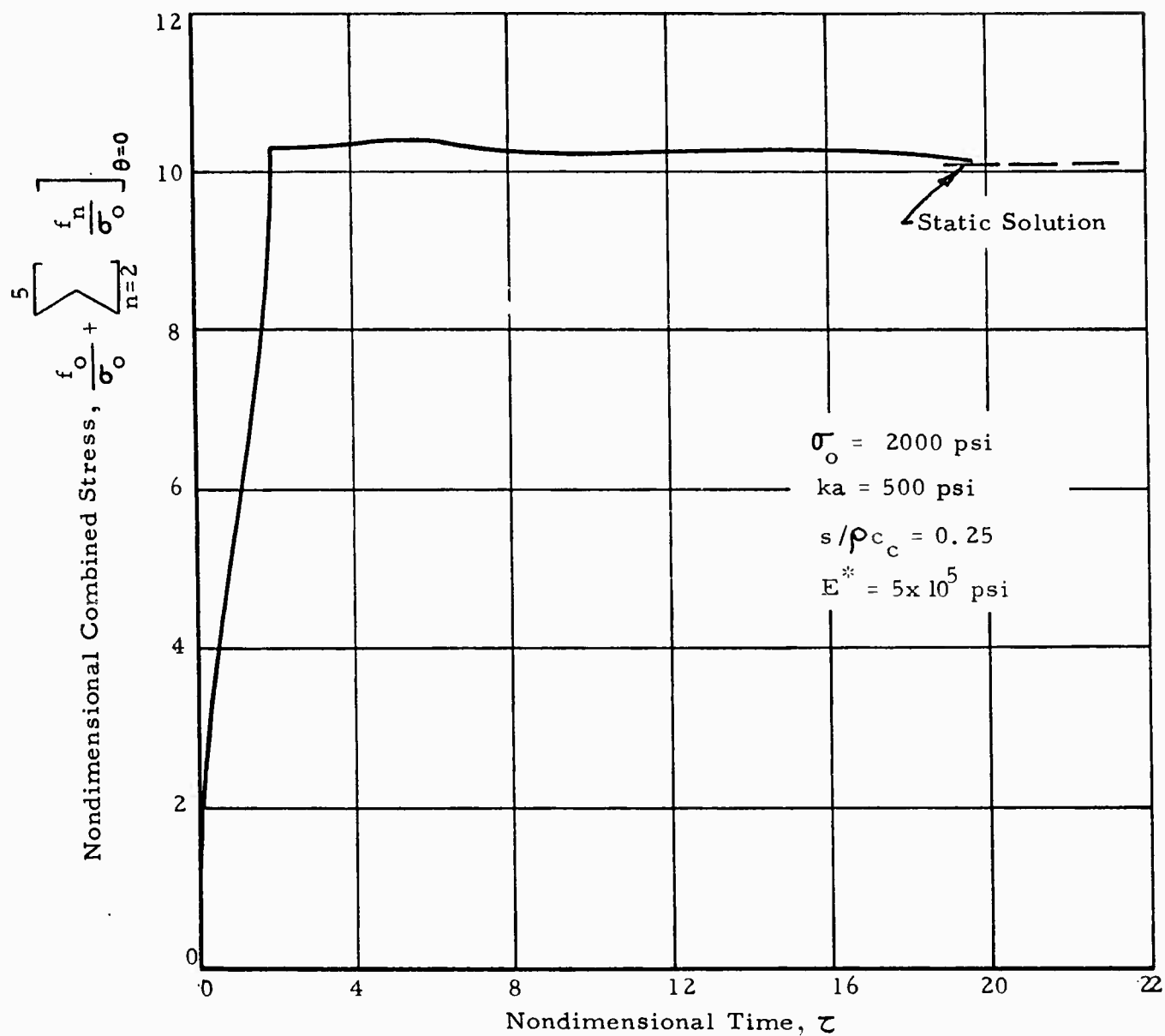


Fig. 8c COMBINED STRESS-TIME VARIATION (CASE 35)

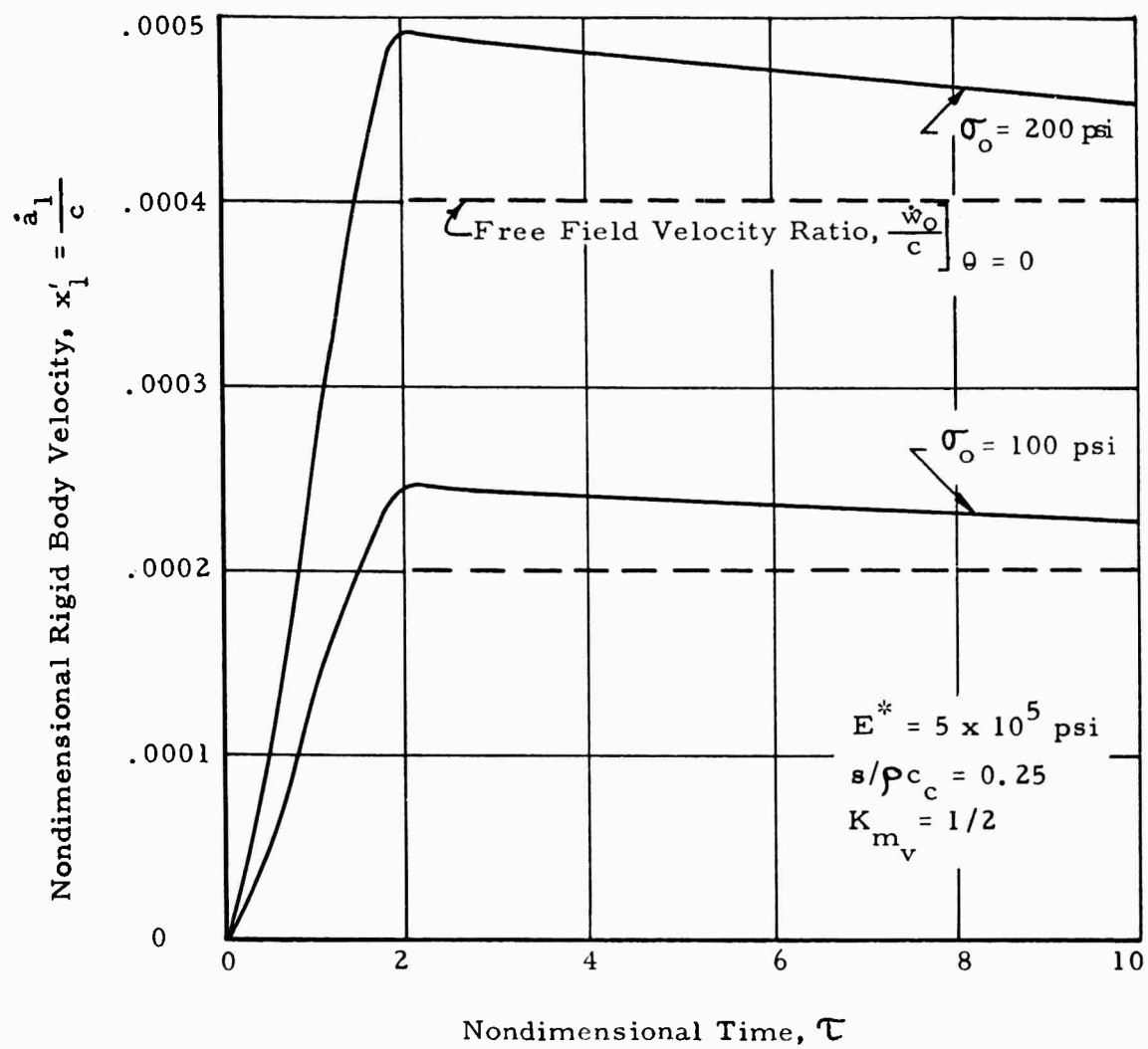


Fig. 9 VELOCITY-TIME VARIATION (SILO)

A biaxiality ratio of unity has been chosen since the plane of the ring for a silo lining is horizontal and the free-field pressures in the x and y directions (see Fig. 1) are both normal to the air-blast overpressure loading acting on the ground surface. The apparent soil modulus,  $E^*$ , has been based on equation 2 and is determined once the engulfment speed,  $c$ , is selected. For an air-blast overpressure of 300 psi, a value of  $c = 4810$  fps is obtained for a standard sea level atmosphere. This value is used for the four cases (cases 32 through 35) selected to study the effect of  $\sigma_0$  and  $ka$  variations. An engulfment speed ( $c$ ) of 2000 fps was used to investigate the effects of lining thickness variations (Cases 36, 37 and 38) to accentuate the dynamic effects. This engulfment speed grossly underestimates the speed associated with the peak free-field stress of 200 psi considered in the thickness variation study since an air blast overpressure of only 37.5 psi produces an air shock front velocity of 2000 fps.

Typical curves of pressure, relative displacement, and combined stress-versus-time are given in figures 8a, b and c and rigid body velocity-versus-time curves in figure 9. The peak values of the response quantities and the time of occurrence are listed in table 2.

#### G. Discussion of Results

The ratios of maximum dynamic-to-static values (D.F.L.) of peak combined stress and relative displacement are given in tables 1 and 2 for the tunnel and silo cases respectively. The tunnel cases show that the introduction of a relative velocity component greatly reduces the maximum response. In the cases where  $ka = 500$  psi, the D. L. F. for stress is reduced from approximately 1.8 for zero damping to a point where the static values are not even attained during five transit times ( $\tau = 10$ ) when the value of  $s/\rho c_c = 0.5$ . It is also noted that even relatively small values of  $s/\rho c_c$  result in large D. L. F. reductions. The effect obtained by increasing  $s/\rho c_c$  for all cases studied corresponds to the belief that the response of buried structures is heavily damped. Since all solutions are for constant peak free-field stress of  $\sigma_0$ , the effects of a decaying pulse will be considerably less if the decay is substantial in four or five transient times.

The value of  $s/\rho c_c$  determines the reflected pressure at the head-on



point at  $\tau = 0$ , and reflection factors accompanying the heavily damped response are small enough to seem realistic. When the pulse has a rise time of  $\tau_1 = 2.0$ , the reflection effects are nearly eliminated.

The effect of adding virtual mass is to increase the maximum response for the step pulse considered. The increase in the D. L. F. is less than 0.26 for all cases when  $s/\rho c_c \leq 0.125$ . Mass effects would be much more pronounced for more realistic loading (decaying free-field stress wave). Decreasing the wall thickness (increasing  $a/h$  from 10 to 20 then 30) decreases the dynamic effects for all values of  $ka$  considered. The reduction in D. L. F. is less than 0.28 for values of  $ka$  equal to 5000 and 2000 psi; however, a very pronounced effect is noted when  $ka = 500$  psi. It is observed that the static relative displacement and stress enlarge to intolerable values for both  $a/h$  increases; however, the static values are not obtained within five transit times. The large response times associated with these cases could conceivably result in acceptable displacements and stress for a decaying free-field stress pulse.

For the silo cases considered, the peak free-field stress variations (Cases 32-35, Table 2) slightly increase the dynamic-to-static values of maximum relative displacement and have no effect on the combined stress D. L. F. All absolute dynamic displacements are low for concrete linings, even for the large D. L. F. 's associated with Cases 34-36, since the static displacement is very small for reasonable lining diameters. Bending stresses are almost trivial for the concrete lining cases. These low values can be attributed to the hydrostatic free-field stress ( $\beta = 1$ ) and the large apparent soil modulus and engulfment speed. Even the unrealistic reductions of  $c$  and  $E^*$  considered in Cases 36 and 37 do not generate appreciable displacement or bending stress response values. When a steel shell with  $a/h$  of 60 is assumed (Case 38) static solutions are intolerable (e. g., static combined stress of  $775.9 \times 200 = 155$  ksi); however, the dynamic relative displacement and bending stress are less than 0.01 times the static values up to 10 transit times ( $\tau = 20$ ). Again, just as it was noted for the tunnel cases, the large response times associated with flexible linings will have an appreciable effect on the response values for a decaying pulse.

ARMOUR RESEARCH FOUNDATION OF ILLINOIS INSTITUTE OF TECHNOLOGY

The curves of velocity in the rigid body mode, given in figure 7 for the tunnel study, indicate that in cases where the virtual mass is zero, the velocity overshoots the free-field value. The addition of virtual mass results in what appears to be more "realistic" behavior, that is, the velocity of the structure approaches the free-field value asymptotically. However, it remains for experimentation to show what "realistic" behavior is.

#### H. Solution for Static Loading

The results of the preceding section show that in the cases considered the maximum dynamic stress exceeds the stress under static load by less than 40 percent when damping of  $s/\rho c_c \geq 0.125$  is included. In the dynamic case a numerical integration of the equations of motion is required for the determination of the displacement amplitudes,  $x_n$ ; however, for the static case they are given by the simple formula

$$x_n = g/f_o, \quad n=2, 3, \dots, \dots,$$

where equations 47 and 48 define  $f_o$  and  $g$  respectively. Since  $g=0$  for  $n \geq 2$  there is no bending in the higher modes ( $n \geq 2$ ). The maximum combined stress is therefore equal to the sum of the direct stress,  $f_D$ , plus the bending stress in the first bending mode ( $n = 2$ ),  $f_B$ .

The direct stress is equal to

$$f_D = \frac{a}{h} \sum \frac{p_n}{n^2 - 1} \cos n \theta, \quad n=0, 2, 3, \dots \quad (56)$$

The value  $p_o$  is given in equation 42. From equation 32, ignoring dynamic effects,

$$p_n = b_n + ka(c_n - x_n), \quad n \geq 1$$

Substituting from equations 27 and 28 and noting that  $x_n = 0$  for  $n \geq 2$  we find

$$\begin{aligned} \frac{f_D}{\sigma_o} \frac{h}{a} = & \frac{-(1+\beta+ka/E^*)}{2(1+\frac{ka}{Eh})} + \frac{1}{3} \left[ \frac{1-\beta}{2} + \frac{ka}{2E^*} + \right. \\ & \left. - \frac{ka}{\sigma_o} x_2 \right] \cos 2\theta, \end{aligned} \quad (57)$$

where positive direct stress denotes tension.

The displacement ratio in the first bending mode is obtained by neglecting the dynamic terms in equation 44, thus

$$x_2 = g/f_o$$

Using equations 47 and 48 this may be expressed as

$$x_2 = \frac{\sigma_o}{6} \frac{1 - \beta + ka/E^*}{3 \frac{\bar{E} I}{a^3} + \frac{ka}{3} - \sigma_o \frac{1 + \beta + ka/E^*}{2(1 + ka^2/\bar{E}h)}}$$

or

$$x_2 = \frac{\sigma_o \left(1 + \frac{ka^2}{\bar{E}h}\right) \left(1 - \beta + \frac{ka}{E^*}\right) / \left(1 + \beta + \frac{ka}{E^*}\right)}{3 \left\{ \frac{2(1 + ka^2/\bar{E}h)}{1 + \beta + ka/E^*} \left[ 3 \frac{\bar{E} I}{a^3} + \frac{ka}{3} \right] - \sigma_o \right\}} \quad (58)$$

The denominator in equation 58 becomes zero when  $\sigma_o$  reaches the value required to cause buckling in the mode  $n = 2$

$$\sigma_{cr2} = \frac{2(1 + \frac{ka^2}{\bar{E}h})}{1 + \beta + \frac{ka}{E^*}} \left( 3 \frac{\bar{E} I}{a^3} + \frac{ka}{3} \right) \quad (59a)$$

Equation 58 can also be written

$$x_2 = \frac{\alpha_2}{1 - \alpha_2} \left[ \frac{1 - \beta + \frac{ka}{E^*}}{3(1 + \beta + \frac{ka}{E^*})} \right] \left( 1 + \frac{ka^2}{\bar{E}h} \right) \quad (59b)$$

where

$$\alpha_2 = \sigma_o / \sigma_{cr2} \quad (59c)$$

The buckling pressure  $\sigma_{cr2}$  is so large for reasonable values of  $ka$  that the effect of direct stress on bending in the second mode can generally be neglected. In this case  $\alpha_2 \ll 1$  and the approximation that

$$\frac{\alpha_2}{1 - \alpha_2} \approx \alpha_2 \quad (59d)$$

can be used.

Then

$$x_2 \approx \sigma_0 \frac{1 - \beta + ka/E^*}{6 \left( \frac{3\bar{E}I}{a^3} + \frac{ka}{3\bar{E}} \right)} \quad (60)$$

The bending stress in the second mode is equal to the static bending stress, or

$$f_B = \frac{3\bar{E}h}{2a} x_2 \cos 2\theta$$

Using the approximation for  $x_2$  (Eq. 60)

$$f_B \approx \frac{\sigma_0 h}{a} \left[ \frac{1 - \beta + ka/E^*}{4 \left( \frac{3I}{a^3} + \frac{ka}{3\bar{E}} \right)} \right] \cos 2\theta. \quad (61)$$

Figure 10 gives curves of nondimensional combined bending plus direct stress at the head on point,  $\theta = 0$ ,

$$\left[ \frac{f_D + f_B}{\sigma_0} \right]_{\theta = 0}$$

for four values of the biaxiality ratio ( $\beta$ ) and values of the radius to thickness ratio ( $a/h$ ) from 10 to 30. The second order contribution of the bending mode ( $n = 2$ ) to the direct stress has been neglected in the calculations (i.e., the second term in the right hand member of equation 57 is neglected). Values of  $\bar{E} = 3 \times 10^6$  psi,  $E^* = ka$  and four values of the foundation modulus ( $ka = 500, 2000, 5000$  and  $20,000$  psi) have been used in the computation.

The solid curves of figure 10 represent the nondimensional combined stress when the effects of axial ring force on bending are neglected (i.e., utilizing the approximation for  $f_B$  given in Eq. 61). These curves give good approximations to the combined stress when the buckling pressure,  $\sigma_{cr2}$ , is large compared to  $\sigma_0$ , or when,  $\alpha_2 = \sigma_0/\sigma_{cr2} \approx 0$ . The dashed curves give the exact combined stress for an applied pressure of

ARMOUR RESEARCH FOUNDATION OF ILLINOIS INSTITUTE OF TECHNOLOGY

$\sigma_0 = 200$  psi and indicate the error involved in the approximation. Observe that, for large values of the foundation modulus, the approximate solution yields nearly the same combined stress as the exact solution for the parameters selected.

The effects on maximum combined stress of increasing the wall thickness while holding the radius fixed can be seen from the curves in figure 10. These results show that maximum combined stress can actually be increased by increasing the wall thickness (decreasing  $a/h$ ). Further examination of the curves reveals that variations of the radius to thickness ratio from 10 to 30 have a relatively minor effect on the combined stress for  $2000 < ka < 5000$ . As expected, increasing the biaxiality ratio and the foundation modulus give reductions in combined stress. However, when  $ka = 20,000$  psi and  $a/h \gtrsim 15$ , increasing the biaxiality ratio actually increases the combined stress. This occurs because the bending stress becomes relatively unimportant for sufficiently high values of  $ka$  and  $\beta$  and the direct stress (which increases with  $\beta$ ) dominates the combined stress expression.

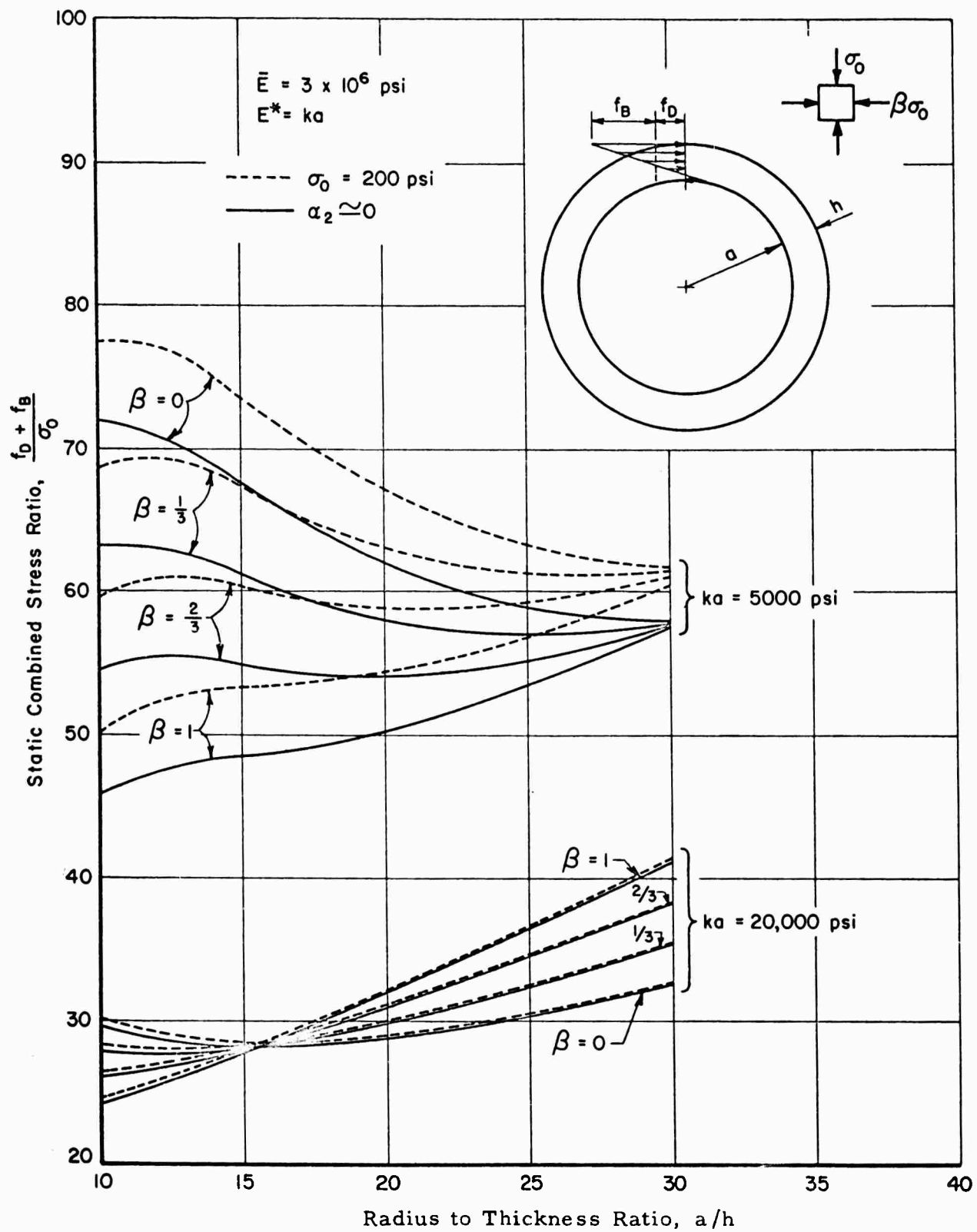


Fig. 10a STATIC COMBINED STRESS-RADIUS TO THICKNESS RATIO VARIATION

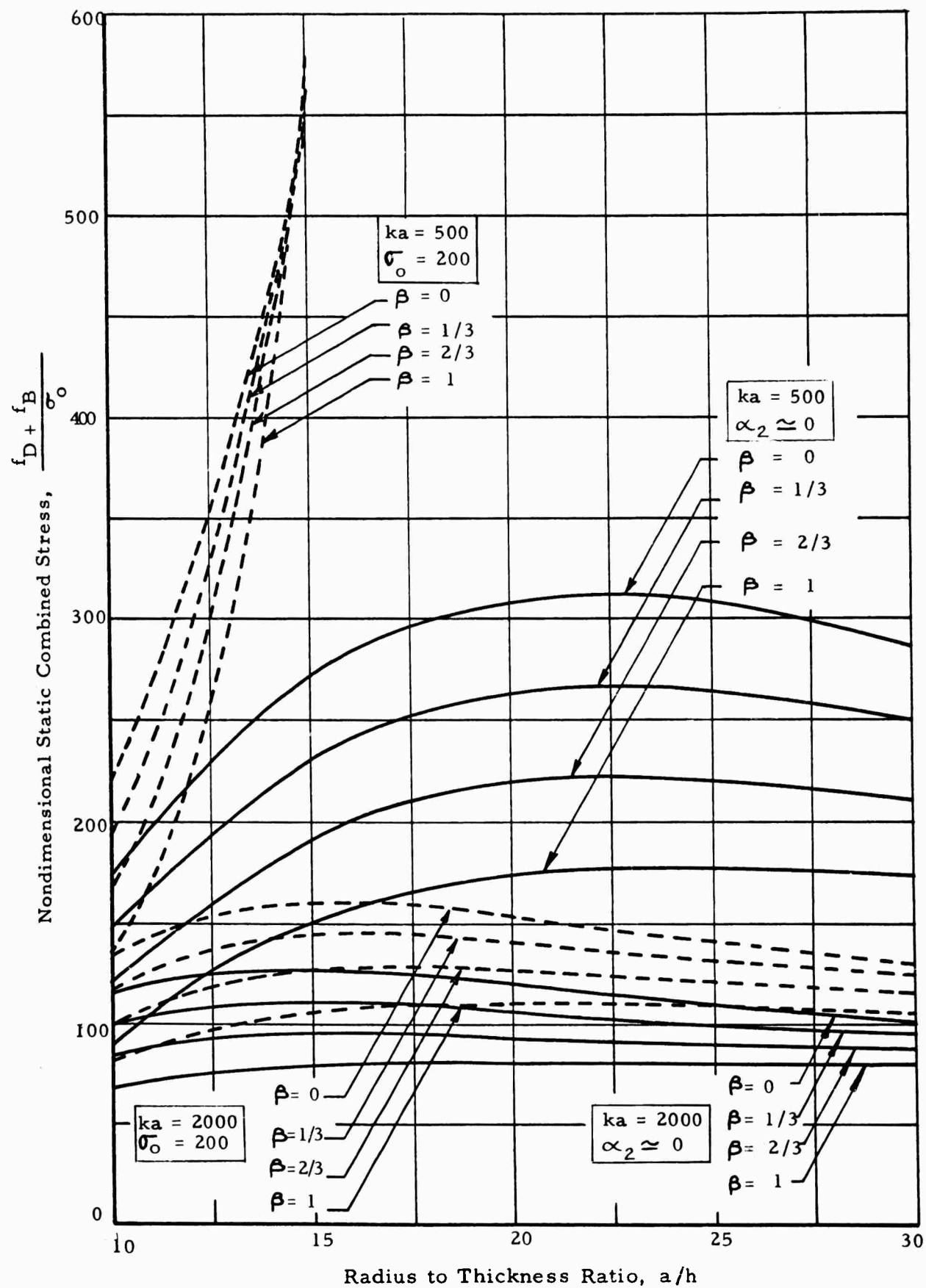


Fig. 10b STATIC COMBINED STRESS-RADIUS TO THICKNESS RATIO VARIATION

# SYMBOL INDEX

## Section II

a	shell radius	t <sub>1</sub>	rise time of stress wave
a <sub>n</sub>	peak shell modal displacement	u	free-field displacement
b <sub>i</sub>	Fourier series coefficients of $\sigma_{rr}$	U	strain energy
c	engulfment velocity of shell section	v	shell tangential displacement
c <sub>c</sub>	soil compression wave velocity	w	shell radial displacement
c <sub>i</sub>	Fourier series coefficients of w <sub>o</sub>	w <sub>o</sub>	free-field radial displacement at shell surface
d <sub>i</sub>	Fourier series coefficients of $\dot{w}_o$	W <sub>e</sub> , W <sub>i</sub>	external and internal work
E	Young's modulus of shell	x, y	coordinates
$\bar{E}$	$E/(1 - \nu^2)$	x <sub>n</sub>	a <sub>n</sub> /a
E	apparent modulus of soil	$\alpha_2$	$\sigma_o/\sigma_{cr2}$
E <sub>c</sub>	soil modulus in confined compression	$\beta$	free - field stress biaxial ratio
f <sub>o</sub> , f <sub>1</sub> , f <sub>2</sub>	equation of motion coefficients	$\epsilon$	free - field strain in x-direction
f <sub>D</sub>	shell static direct stress	$\epsilon_o$	peak free-field strain in x-direction
f <sub>B</sub>	shell static bending stress	$\epsilon'$	free-field strain in direction of stress wave propagation
g	equation of motion coefficient	$\eta, \xi, \psi$	closed form solution constants
h	shell thickness	$\theta$	angular coordinate of point on shell
k	foundation modulus	$\nu$	Poisson's ratio
K <sub>m<sub>v</sub></sub>	virtual mass coefficient	$\rho$	soil density
m <sub>v<sub>n</sub></sub>	virtual mass	$\rho_s$	shell density
n	shell displacement mode	$\sigma$	free-field pressure in x-direction
p	pressure normal to shell surface	$\sigma_o$	peak free-field pressure in x-direction
P <sub>n</sub>	peak modal normal pressure	$\sigma_{cr2}$	shell buckling pressure in second mode
P <sub>o</sub>	uniform radial pressure	$\sigma_{rr}$	radial free-field pressure at shell surface
r	c/c <sub>c</sub>	$\sigma'$	free-field pressure in direction of stress wave propagation
s	coefficient of damping	$\tau$	ct/a
s <sub>cr</sub>	critical damping coefficient	$\tau_1$	ct <sub>1</sub> /a
S <sub>i</sub> , S' <sub>i</sub>	Fourier series arguments	$\theta, \theta_1$	angular coordinates
t	time	$\chi$	angle between shell axis and stress wave front



### III. STATIC LOAD TESTS ON TUNNELS

#### A. Introduction

As part of the investigation of silo and tunnel linings, a series of static tests on 6-inch diameter tubes (horizontally oriented) buried in dense, dry Ottawa sand were performed. The objective of the test program was to investigate the ability of the analysis given in the Section II H (Static Response of Silo and Tunnel Linings to Radial Pressure) to predict stresses and displacements under static load. These experiments are a necessary preliminary to dynamic tests and also serve to point out some of the problems associated with small tunnel model testing.

Tests were performed on steel cylinders with radius to thickness ratios of 60 and 40 (one each) and an aluminum cylinder with a ratio of 60 in a sand-filled pressure vessel three feet in diameter and height. The test setup, test results and discussion of the results with respect to the theory are presented in the following sections.

Tunnel model strains and radial displacement measurements were taken near the center of the model. Instrumentation for the tests included both electronic and mechanical systems. Electronic measurements were made of radial displacements, and bending and direct strain in the tunnel lining. Mechanical measurements were made to ascertain applied pressures, soil surface deflections and rigid body tunnel displacements.

#### B. Test Setup and Instrumentation

All tests of the tunnel models were performed in a 3-ft inside diameter, 3-ft high flanged steel cylinder (Fig. 11). The inside surface of the 1/2-in. cylinder wall was lined with two unbonded sheets of Teflon (0.01-in. thickness) to reduce vertical soil restraint at the containment vessel wall to a tolerable value. Experiments (8) indicate that such a treatment is worthwhile even though it does not completely eliminate wall friction. Cover plates 2-1/8 in. thick bolted to the cylinder flanges with thirty-six 1/2 in.-diameter high-strength bolts and a rubber sealing membrane placed over the sand surface and between the cylinder flange and upper cover plate complete the containment vessel. Surface loading is accomplished by

ARMOUR RESEARCH FOUNDATION OF ILLINOIS INSTITUTE OF TECHNOLOGY

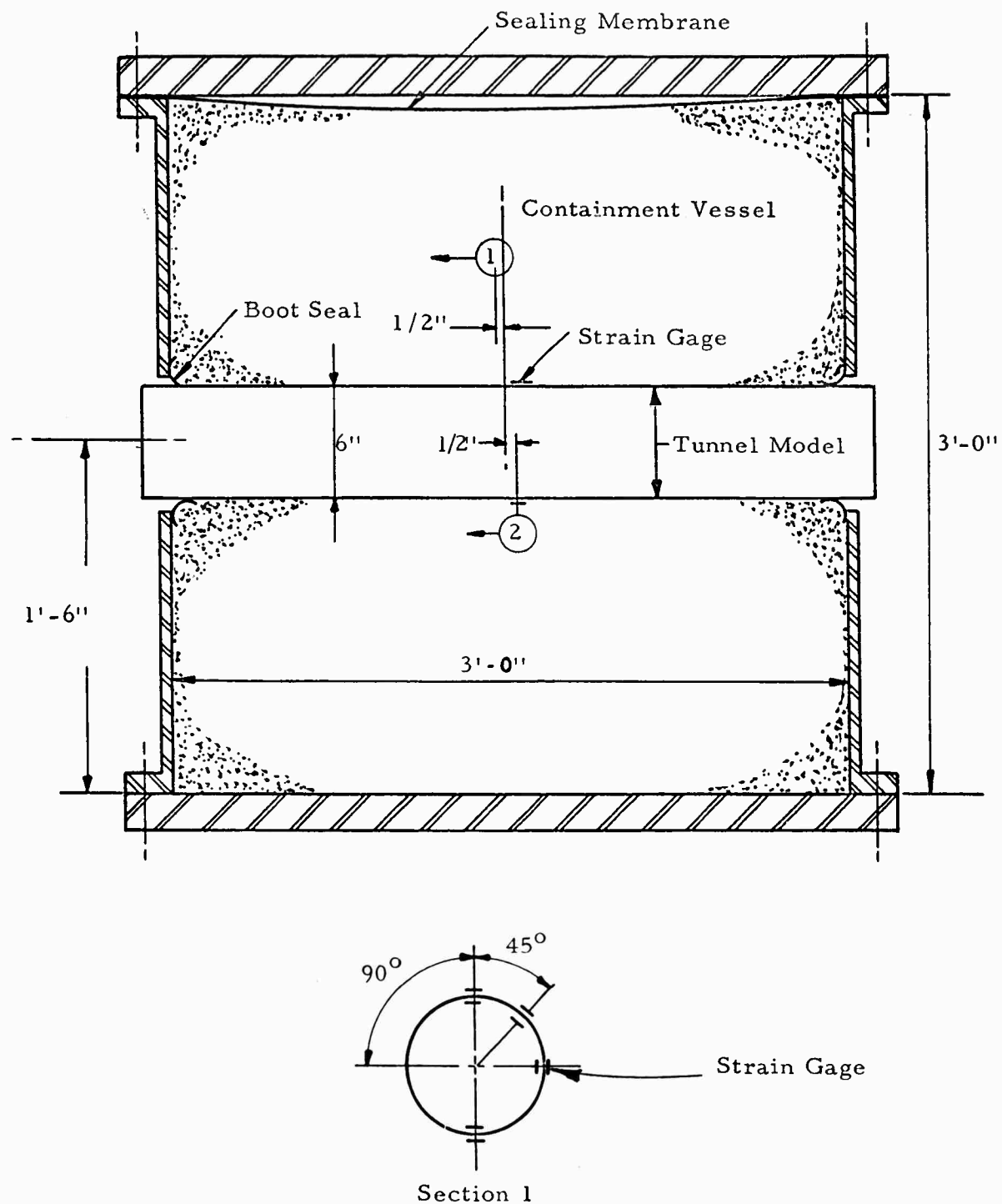


Fig. 11 TUNNEL MODEL TEST ARRANGEMENT

admitting air pressure between the membrane and the cover. Two diametrically opposite holes (7-in. diameter) are located at mid-depth in the cylinder wall. The tunnel model extends through these openings and projects approximately 1-1/2 in. past the wall at each opening. Leather boot seals were provided at the model-containment vessel interface to prevent soil loss in a manner that did not appreciably restrict the model or soil motions. A sketch of the pressure vessel with tunnel model in place is shown in figure 11. An overall view of the test setup is shown in figure 12a and the model just prior to burial in figure 12b.

All models were cold-finished from cold rolled-sheet stock. Two models were fabricated from mild steel with radius to thickness ratios of 40 and 60 (0.075 and 0.05 in. wall thicknesses respectively). The third model was 6061-6T aluminum with a yield stress of 35,000 psi and radius to thickness ratio of 60 (0.05 in. wall thickness).

All strain gages used for the test series were temperature-compensated and epoxy backed. A single layer of Scotch tape was placed over each outer gage for protection purposes. Bending and direct stress were determined from strain measurements made with Budd etched foil strain gages, type C6-141. These gages are produced from thin alloy foil sheet by photo-etching techniques similar to those used in producing printed circuits. The gage is designed to be sensitive to the normal stress in steel in the direction of the gage. The grid length, width and the overall gage width are 0.25 in. and the overall gage length is 0.503 in. Gages were located in pairs on the inner and outer surface of the shell to measure hoop strain. For each of the three tunnel lining models gage pairs were located in the invert, one spring line, 45 degrees above the spring line and the crown as shown in Section 1, in figure 11. Strain gages are also mounted at Section 2 on the outside surface at the crown and invert to measure longitudinal strain. A Baldwin SR-4 battery operated strain indicator was used to obtain readings of each gage for all surface pressures.

The radial displacements of the tunnel model were measured at the Section 2 location shown in figure 11. A sketch of the device used for these measurements is shown in figure 13. The displacement gage consists of a Schaevitz differential transformer with a 1/2-in. range mounted normal

ARMOUR RESEARCH FOUNDATION OF ILLINOIS INSTITUTE OF TECHNOLOGY

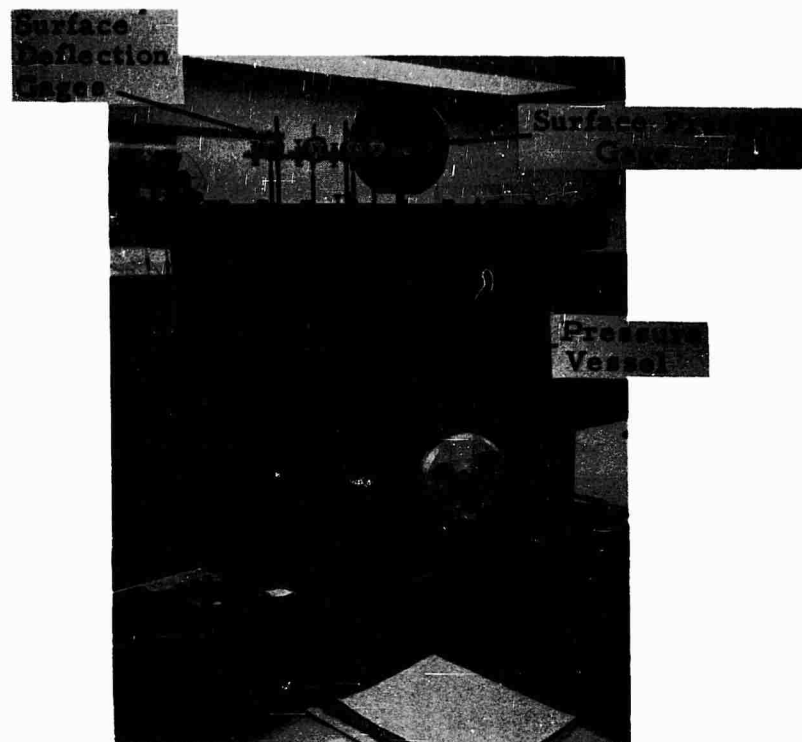


Fig. 12a TUNNEL MODEL TEST SETUP

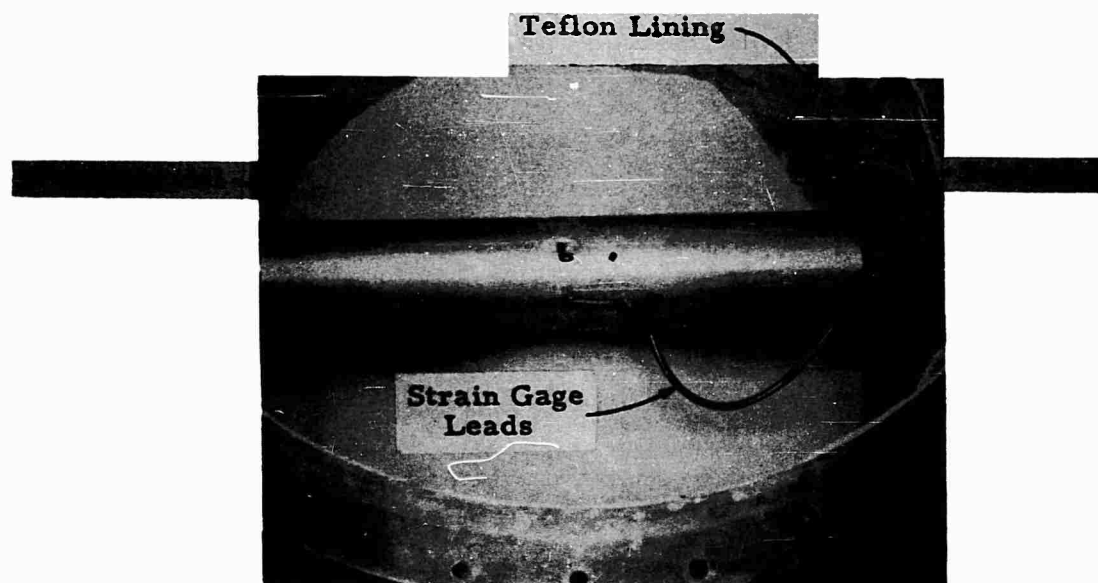


Fig. 12b TUNNEL MODEL PRIOR TO SAND PLACEMENT

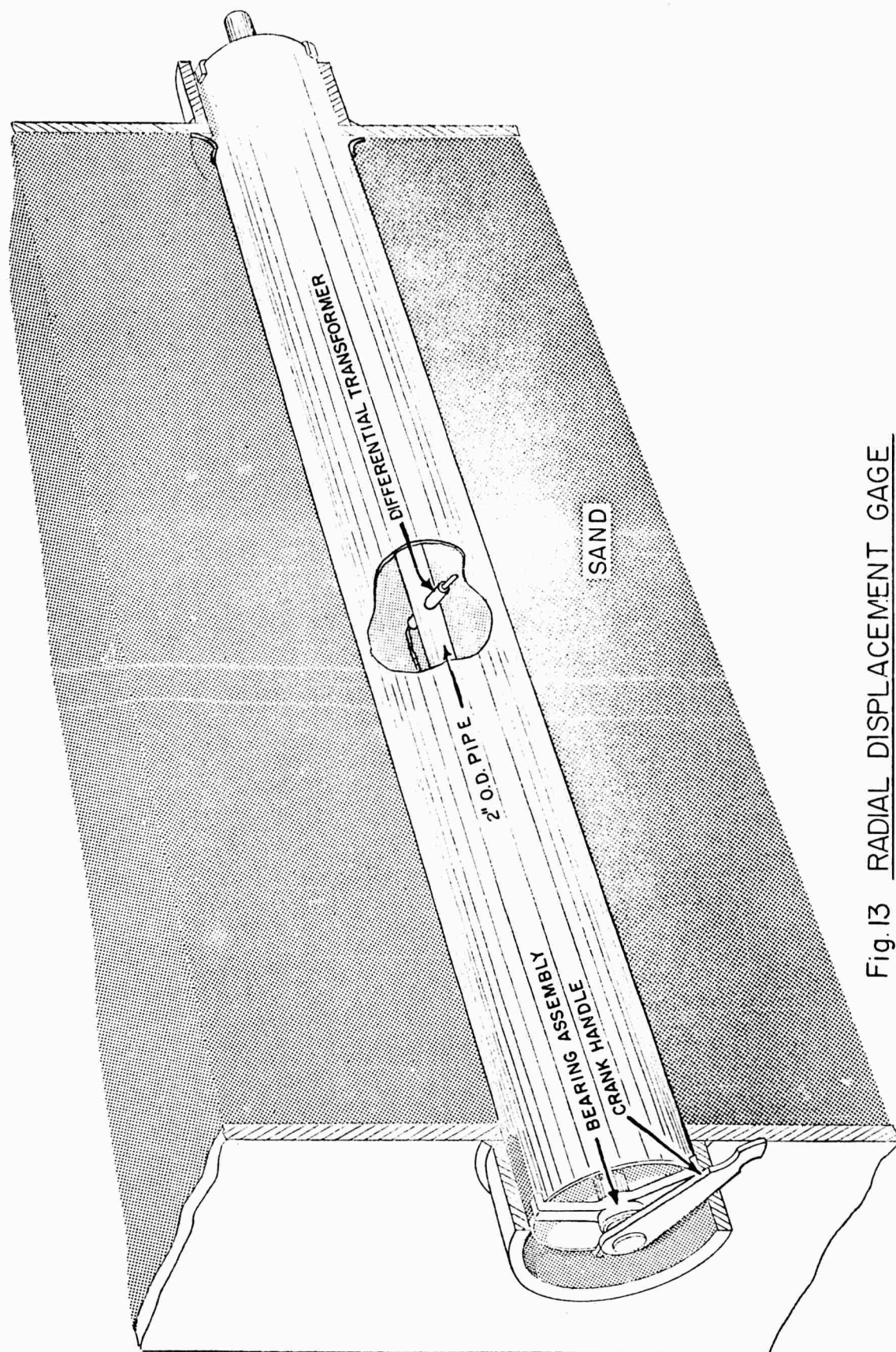


Fig. 13 RADIAL DISPLACEMENT GAGE

to the axis of a 2-in. outside diameter (10 B. W. gage) steel pipe supported at the ends of the tunnel lining model by spherical bearings. A pointer was attached to one end of the pipe to indicate the position of the displacement probe. Adjusting screws were provided at the bearing assembly to initially center the rotation axis at the displacement measurement station. Figure 14 shows three views of the radial displacement gage and the Daytronic amplifier-indicator used to indicate the displacement reading.

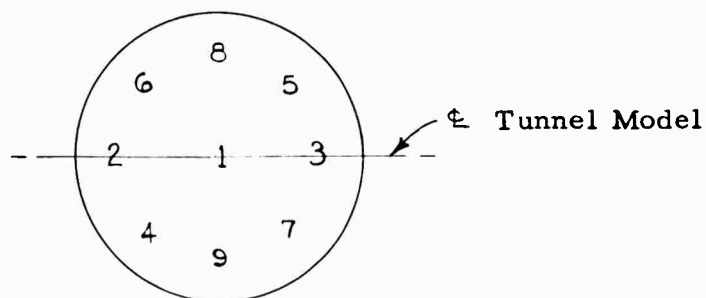
Displacements of the upper soil surface were obtained for each test by dial gage readings that indicated the displacement of four threaded rods mounted to the pressure vessel cover as shown in figure 15. The threaded rods were screwed down until contact of the rod with a small brass disk cemented to the sealing membrane completed a simple electrical light circuit. The rods were located on a ray, normal to the tunnel axis, emanating from the center of the pressure vessel cover. Gages were positioned, zero, 2, 6, and 10 in. from the center. Dial gages were also used to obtain the rigid body tunnel displacement. A gage was attached to the containment vessel at the points where the tunnel model protruded and measurements were made of the radial displacement gage support plate (which was rigidly attached to the end of the tunnel model), (Fig. 14b),

The soil used for all tests was dense Ottawa sand with grain size distribution as in figure 16. A one-horsepower, 10,000-rpm concrete vibrator was used to obtain an average density of 109.0 pcf for each test.

The soil placement procedure was as follows:

#### Step 1

Soil was placed to the tunnel invert (15-in. lift) and compacted by penetration of the vibrator probe to the lift depth in the following pattern:



ARMOUR RESEARCH FOUNDATION OF ILLINOIS INSTITUTE OF TECHNOLOGY

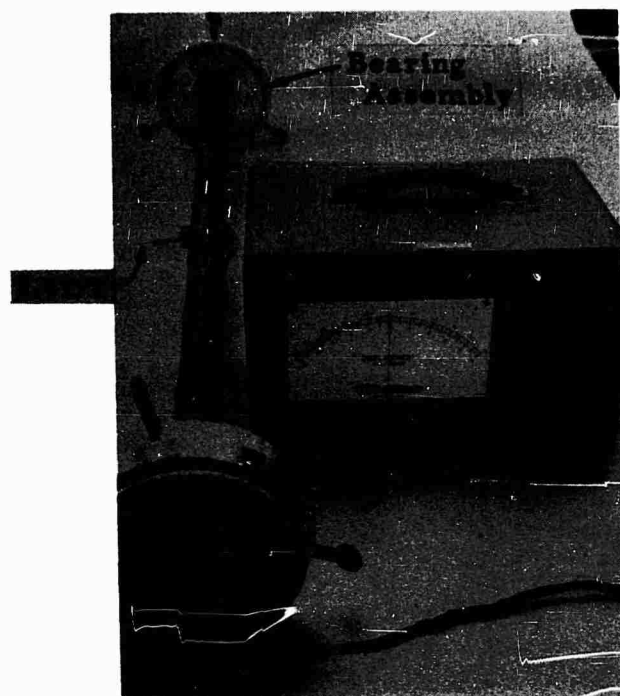


Fig. 14a RADIAL DISPLACEMENT  
GAGE ASSEMBLY AND AMPLIFIER

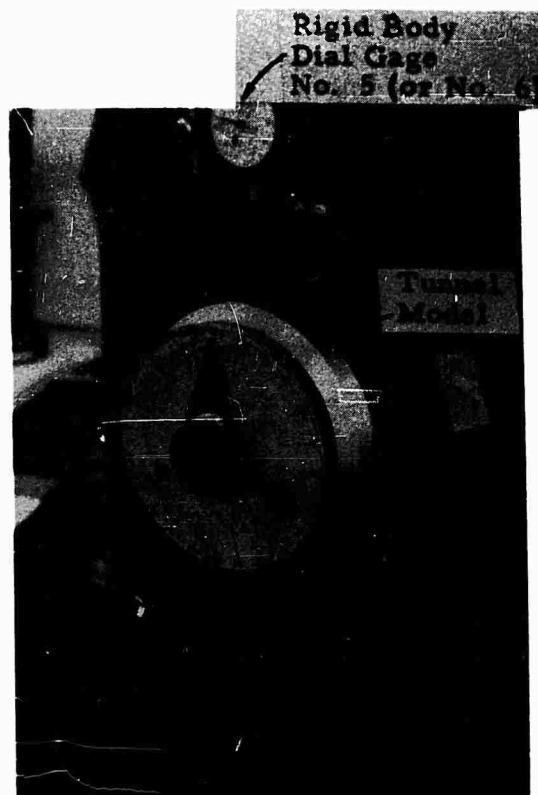


Fig. 14b DISPLACEMENT  
GAGE POSITION POINTER



Fig. 14c DIFFERENTIAL  
TRANSFORMER PROBE

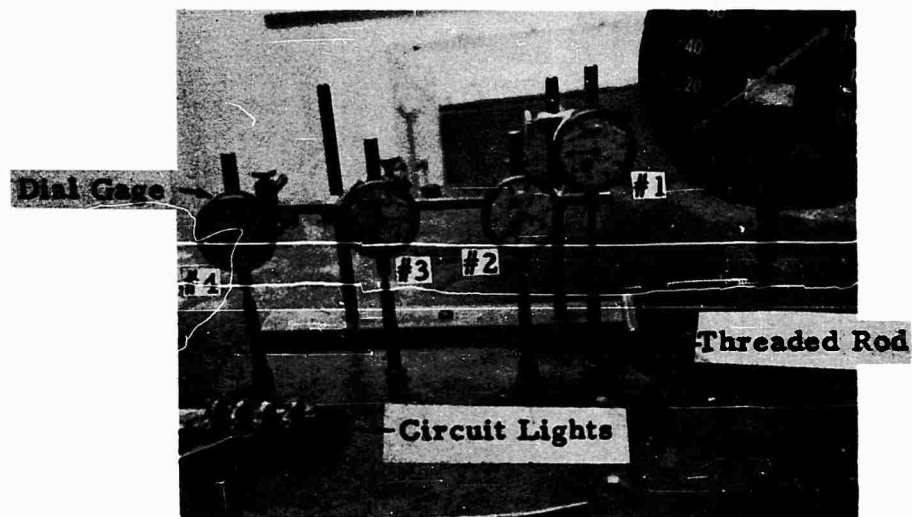


Fig. 15 SURFACE DISPLACEMENT GAGES



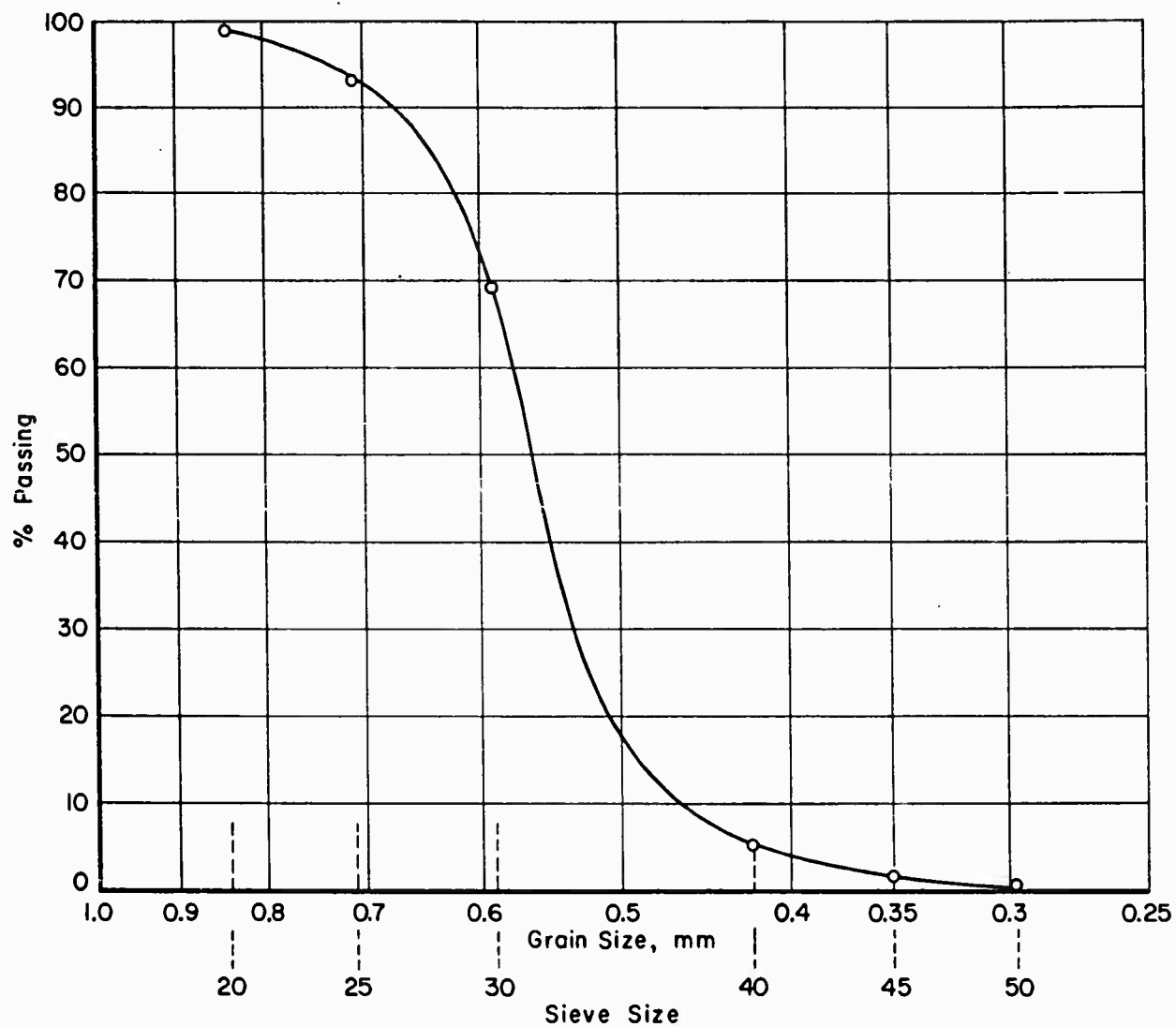


Fig. 16 GRAIN SIZE DISTRIBUTION, OTTAWA SAND

### Step 2

With the tunnel model in position, soil was placed to a height of one tunnel diameter above the crown (12-in. lift) and compacted by penetration of the probe, to a depth of one tunnel diameter below the invert 18-in. penetration in the above pattern exclusive of positions 1, 2 and 3.

### Step 3

Soil was placed to containment vessel flange (9-in. lift) and compacted by penetration of probe to tunnel crown in the pattern shown in step 1.

Density measurements made after each step indicated that the placement technique gave uniform densities.

### C. Test Results

A total of six tests were performed on the two steel and single aluminum tunnel model (two tests per model). Table 3 lists the tunnel model properties and the average soil density for each test. After preparation and placement of each tunnel model in the containment vessel, as described in subsection III B, the first test (denoted by the A suffix) was executed by pressurizing the sand surface in 10 and 20 psi increments up to the maximum pressure of 100 psi. Readings from all instrumentation were recorded for each pressure level during both the loading and unloading cycle. Approximately one day after the first test, without disturbing or recompacting the sand, the procedure was repeated to yield the second test results (B suffix). Thus, two tests were performed on each tunnel model. Applied surface pressure-displacement curves are presented for each dial gage for test 1B in figure 17. Gages 1 through 4 are surface displacement gages (shown in figure 15), located zero, 2, 6 and 10 in. from the center and normal to the tunnel center line. Gages 5 and 6 give the vertical tunnel motions at the points of protrusion.

The surface displacement variation indicated by the curves (gages 1 through 4, figure 17) is qualitatively representative for all tests conducted (i.e., the largest displacements occurred at the center and outer gage points); however, the largest percentage difference, between maximum and minimum displacement, occurred for Test 1B.

ARMOUR RESEARCH FOUNDATION OF ILLINOIS INSTITUTE OF TECHNOLOGY

Table 3

TUNNEL MODEL PROPERTIES

Test	Shell Material	$\frac{a}{h}$	$h$ (in.)	E (psi)	D* (in-lb)	Soil Density** (pcf)
1A	Steel	60	0.05	$3 \times 10^7$	312.5	109.0
1B	Steel	60	0.05	$3 \times 10^7$	312.5	109.0
2A	Steel	40	0.075	$3 \times 10^7$	1055	109.0
2B	Steel	40	0.075	$3 \times 10^7$	1055	109.0
3A	Aluminum <sup>†</sup>	60	0.05	$10^7$	104.	109.0
3B	Aluminum <sup>†</sup>	60	0.05	$10^7$	104.	109.0

\* Flexural Rigidity,  $\frac{E h^3}{12}$

\*\* Dry Ottawa Sand

† 6061-T6, Yield Stress = 35 ksi

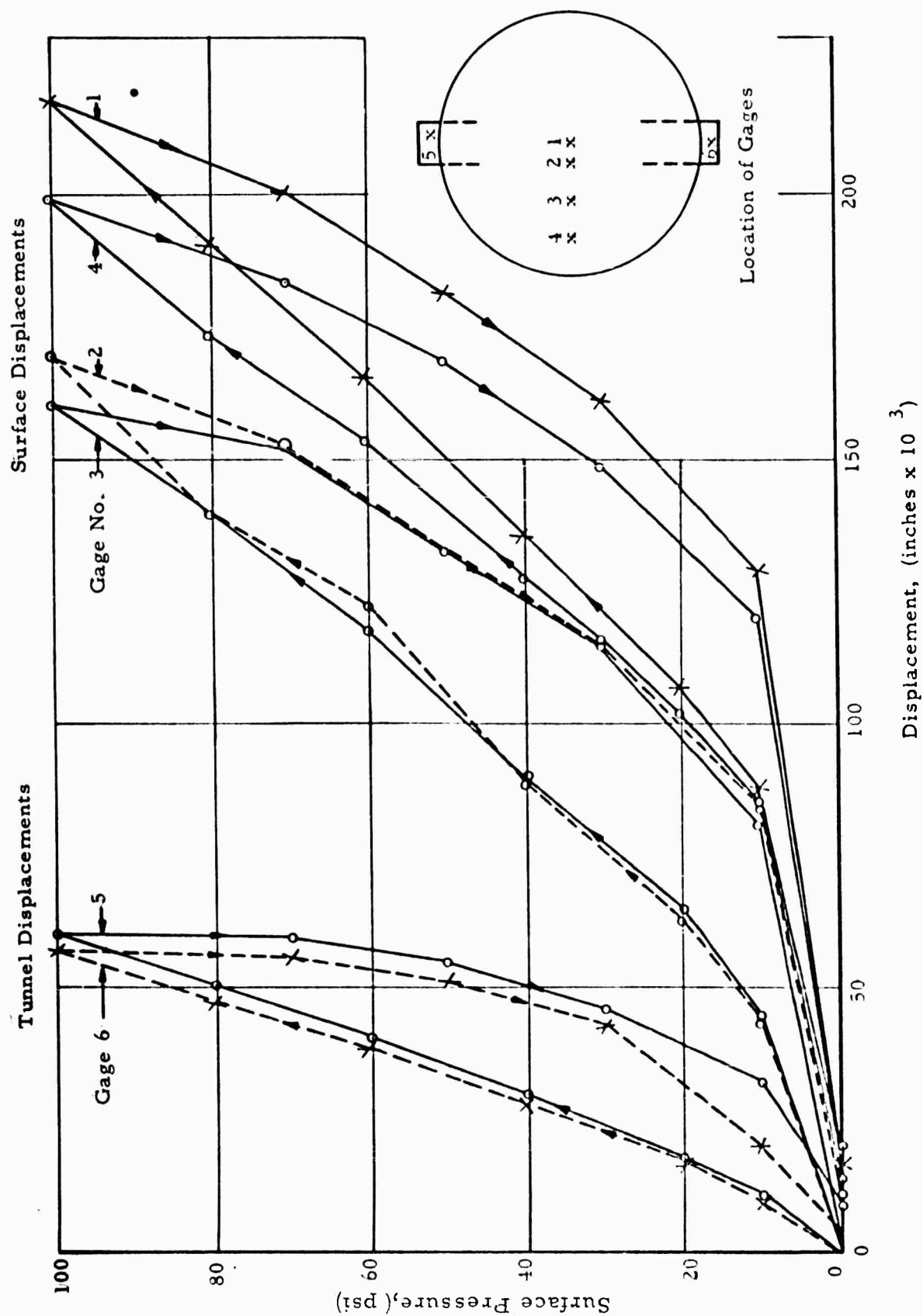


Fig. 17 SURFACE PRESSURE - DISPLACEMENT VARIATION, TEST 1B,  
STEEL TUNNEL MODEL,  $a/h = 60$

Curves of pressure versus average surface displacement (average of Gages 1 through 4) are given in figure 18 for each test. The average vertical tunnel model displacement (average of Gages 5 and 6) is also shown in the figure 18 for each test. It is possible to estimate the tunnel axis curvature from radial displacement gage measurements when the probe is vertically oriented. These measurements yield the middle ordinate deflection of the axis from a straight line connecting the ends of the tunnel. This ordinate plus the average displacement of Gages 5 and 6 represent the rigid body vertical displacement component of the center section (Section 2, figure 11). A maximum middle ordinate deflection of 0.012 in. was observed at the 100-psi pressure level for Test 3A. This displacement is 20 percent of the average end displacement indicating that the rigid body displacement at the center section is slightly larger than the displacement given by the average of Gages 5 and 6.

Diameter changes from the initial position (zero surface pressure) for each test are given in tables 4a through 4f. These values were found from radial displacement gage measurements taken at 15 deg intervals for each surface pressure level. The total diameter change for each position was found by adding the set of measurements obtained 180 deg apart. Figure 19 shows average radial displacements for three surface pressure levels (pressure increasing) for Test 1B.

Bending and direct stress at the crown, 45 deg below crown, springing line and the invert are presented for each test in tables 5a through 5f. These stresses were computed from the strain measurements taken from the gages shown in figure 11. The hoop stresses presented in the table have been corrected to eliminate the longitudinal strain effects from the variation of longitudinal loading. These variations arise primarily from the containment vessel wall friction. Thus the listed stresses are those resulting from loads that do not vary along the tunnel axis.

Consolidation tests were run on the Ottawa sand used in the experiments. The objective of the tests was to obtain appropriate values of the confined modulus ( $E_c$ ) of the soil. Two load cycles with peak stress of 100 psi were applied to the soil sample. The soil density was 109 pcf. The following ratios of stress to strain ( $E_c$ ) during loading were obtained:

ARMOUR RESEARCH FOUNDATION OF ILLINOIS INSTITUTE OF TECHNOLOGY

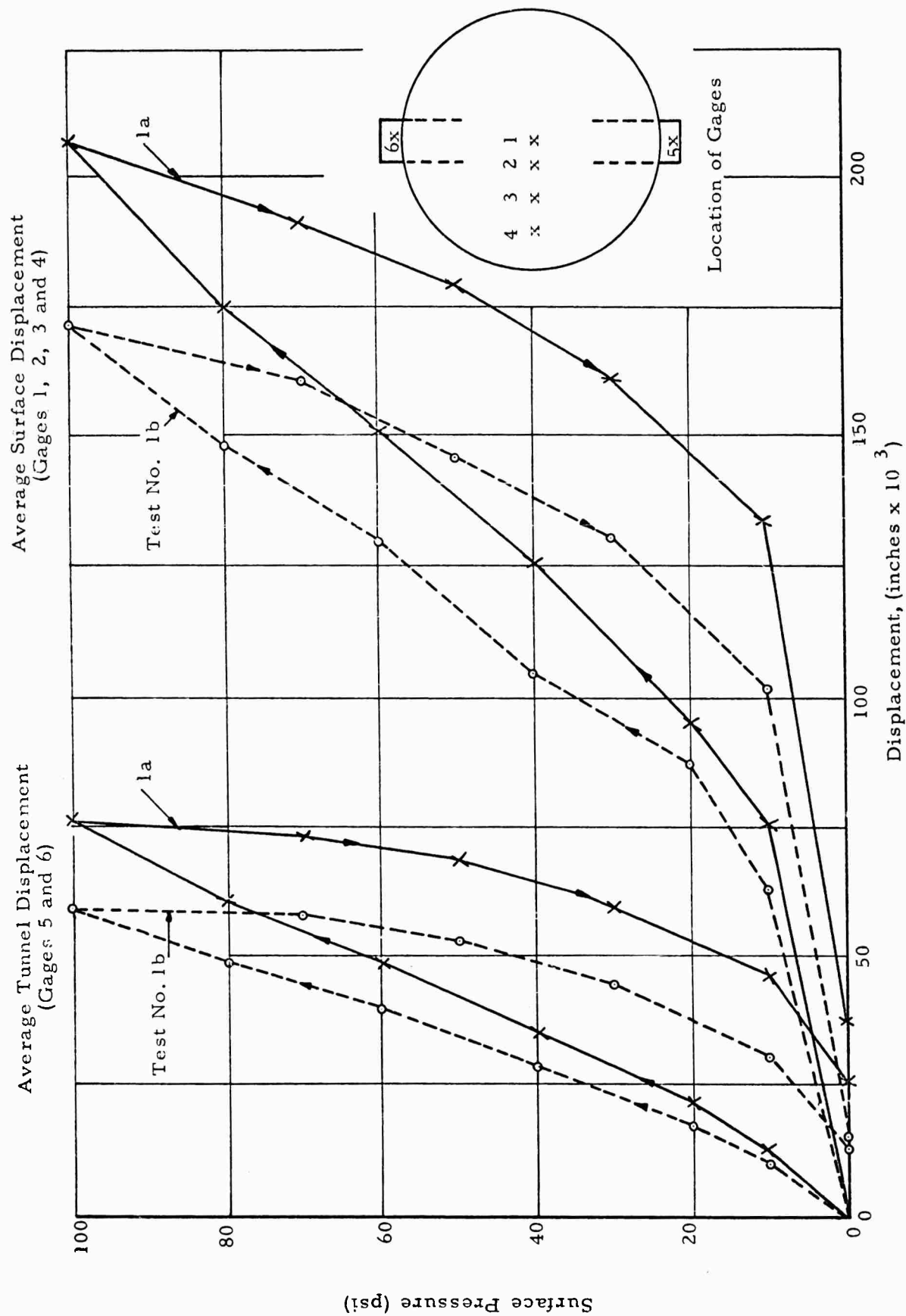


Fig. 18a SURFACE PRESSURE-AVERAGE DISPLACEMENT VARIATION  
STEEL TUNNEL MODEL,  $a/h = 60$

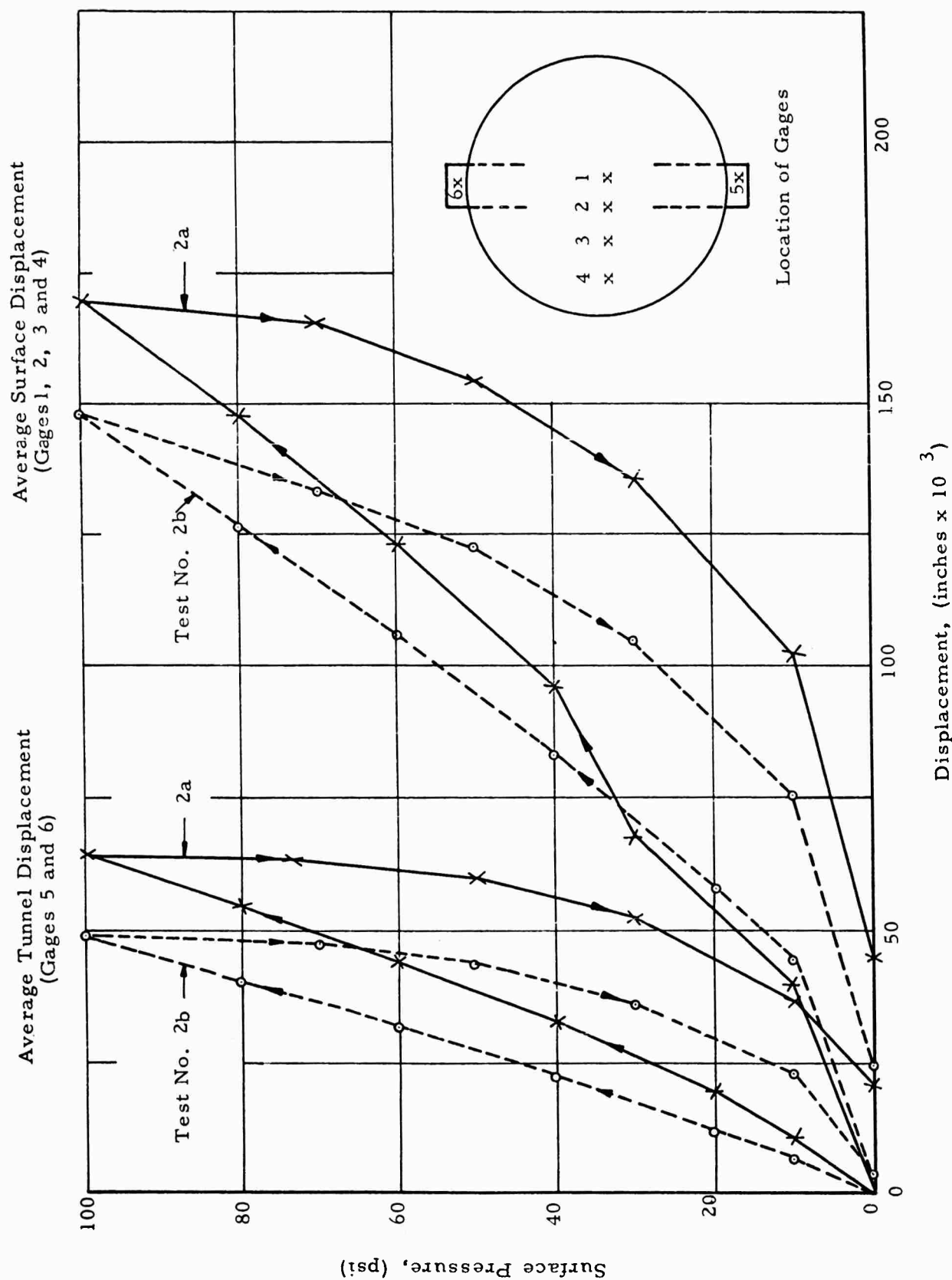


Fig. 18b SURFACE PRESSURE-AVERAGE DISPLACEMENT VARIATION  
STEEL TUNNEL MODEL,  $a/h = 40$

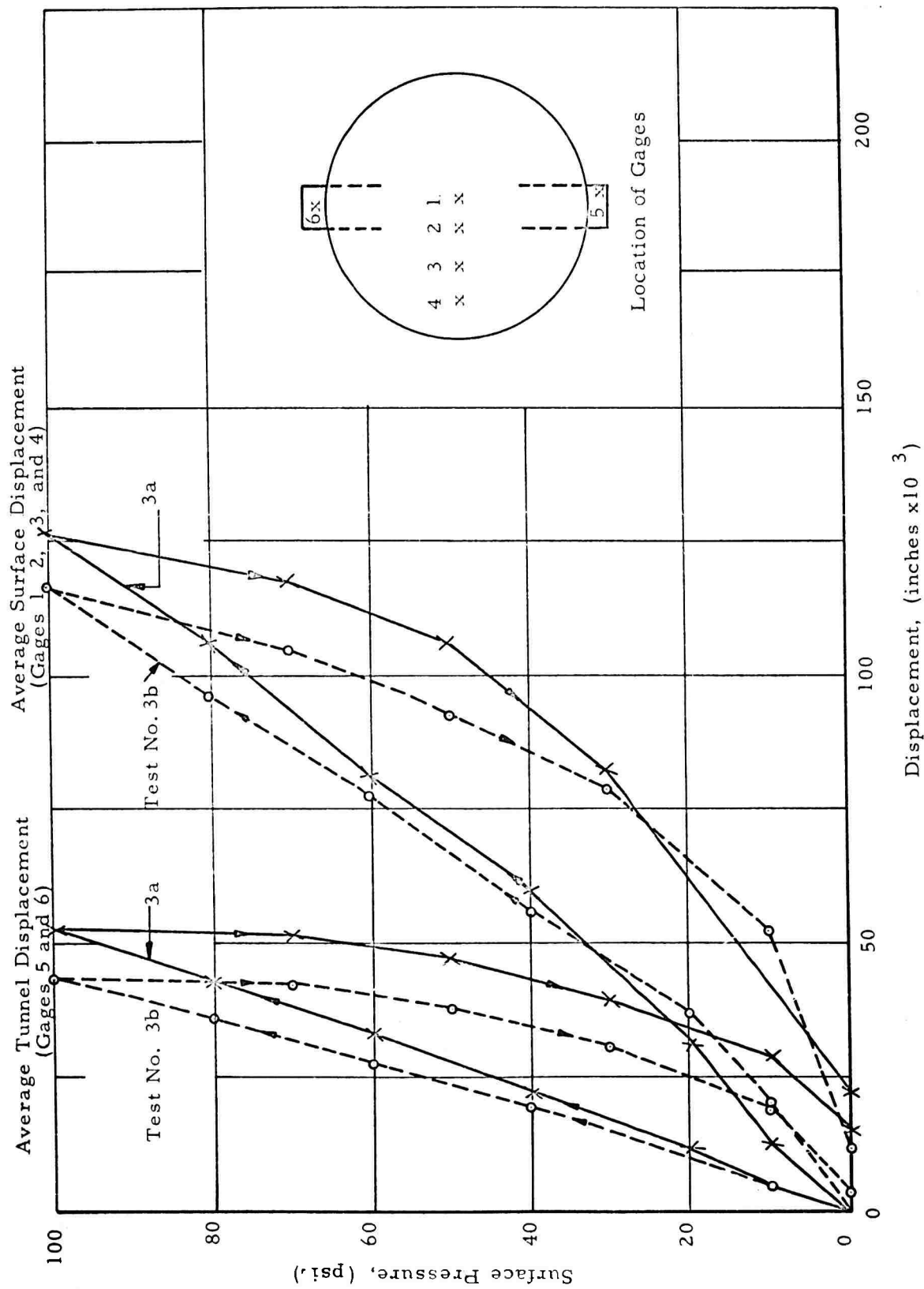


Fig. 18c SURFACE PRESSURE-AVERAGE DISPLACEMENT VARIATION  
ALUMINUM TUNNEL MODEL,  $a/h \approx 60$



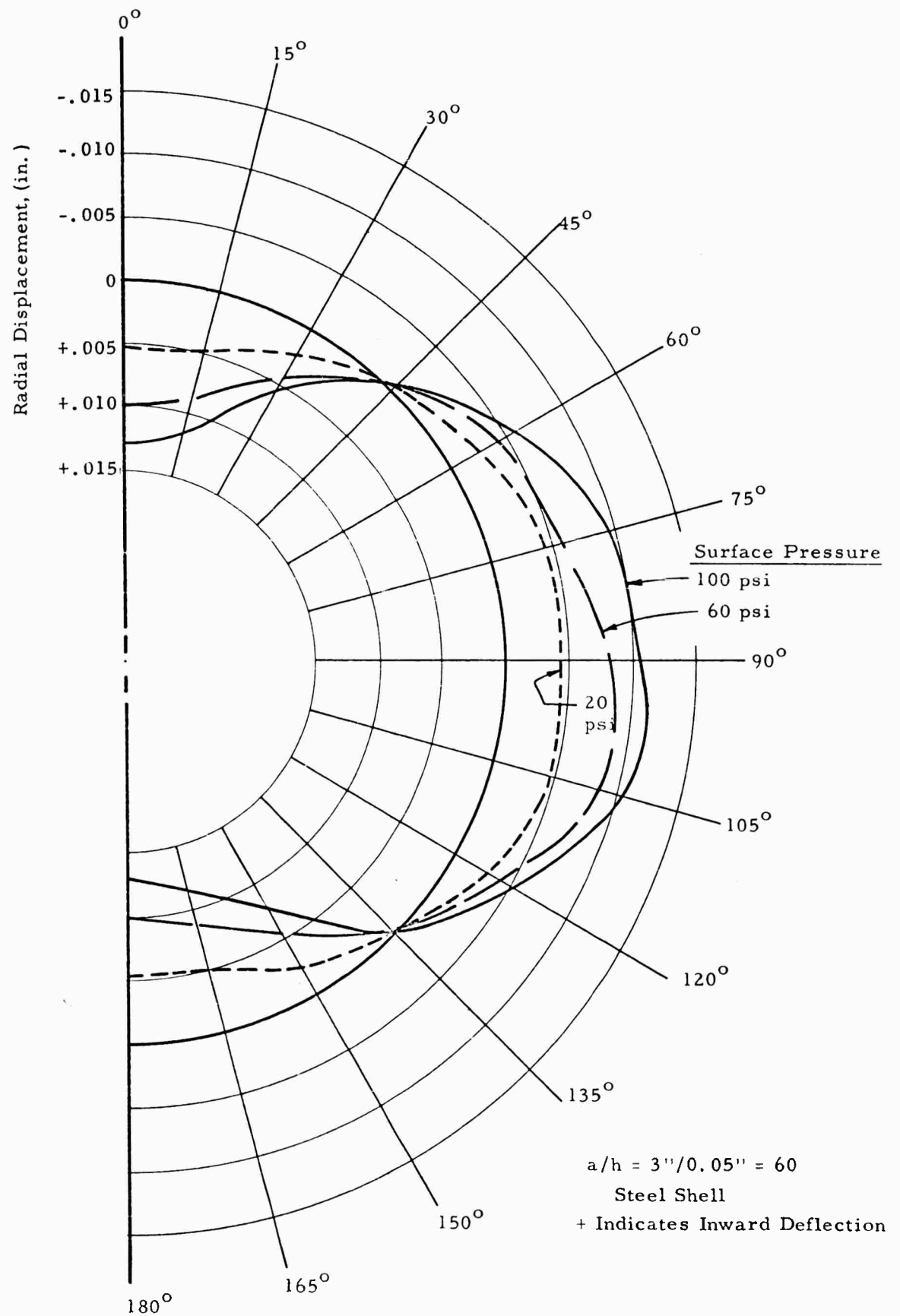


Fig. 19 RADIAL DISPLACEMENTS FOR 15-DEG SEGMENTS

Test 1B

Table 4a  
DIAMETRIC DISPLACEMENT, INCHES X 10<sup>4</sup>  
Test 1A Steel Tunnel Model, a/h = 60

θ, (Deg) (From Vert. Diameter)	Surface Pressure, (psi)											
	Increasing						Decreasing					
	10	20	40	60	80	100	70	50	30	10	0	
0 (Vert.)	55	90	144	194	229	284	264	249	218	171	64	
15	55	84	136	174	200	244	229	218	189	151	52	
30	35	46	75	90	110	133	128	119	104	78	38	
45	- 3	0	0	- 9	- 12	- 15	- 15	- 15	- 15	- 15	3	
60	- 32	- 55	- 70	- 93	- 107	- 139	- 128	- 128	- 116	- 93	- 29	
75	- 52	- 75	- 116	- 154	- 180	- 220	- 212	- 194	- 186	- 145	- 55	
90 (Horiz.)	- 52	- 93	- 131	- 174	- 203	- 249	- 232	- 228	- 200	- 165	- 67	
105	- 52	- 96	- 121	- 154	- 183	- 220	- 209	- 209	- 189	- 151	- 64	
120	- 38	- 58	- 84	- 90	- 143	- 128	- 133	- 116	- 125	- 99	- 75	
135	- 3	- 6	- 3	0	3	0	- 3	- 6	- 3	- 6	- 17	
150	29	55	78	107	125	154	145	133	122	84	23	
165	70	99	136	183	209	26	246	232	203	157	41	

Note: + indicated decrease in diameter.

Table 4b  
DIAMETRIC DISPLACEMENT, INCHES X 10<sup>4</sup>  
Test 1B Steel Tunnel Model, a/h = 60

θ, (Deg) (From Vert. Diameter)	Surface Pressure, (psi)											
	Increasing						Decreasing					
	10	20	40	60	80	100	70	50	30	10	0	
0 (Vert.)	72	107	154	194	223	258	244	226	200	151	35	
15	64	96	136	174	197	229	209	203	174	133	35	
30	29	44	67	81	99	110	107	96	84	58	17	
45	-9	-9	-9	-14	-17	-17	-20	-17	-14	-14	-3	
60	-32	-52	-70	-90	-102	-122	-110	-107	-96	-72	-9	
75	-58	-87	-17	14	-174	-197	-188	-177	-157	-122	-29	
90 (Horiz.)	-58	-90	-128	-171	-186	-218	-200	-194	-165	-139	-32	
105	-61	-93	-119	-180	-177	-212	-186	-200	-160	-128	-38	
120	-29	-55	-78	-81	-96	-104	-99	-97	-93	-67	-35	
135	6	0	0	3	3	-3	0	0	-3	-3	-17	
150	32	46	78	104	119	145	130	119	104	75	6	
165	64	99	142	174	197	232	220	203	174	218	32	

Note: + Indicates decrease in diameter.

Table 4c  
DIAMETRIC DISPLACEMENT, (INCHES X 10<sup>4</sup>)  
Test 2A Steel Tunnel Model, a/h = 40

θ, (Deg) (From Vert. Diameter)	Surface Pressure, (psi)										
	Increasing					Decreasing					
	10	20	40	60	80	100	70	50	30	10	0
0 (Vert.)	+67	+104	+160	+206	+252	+281	+270	+249	+220	+145	+52
15	+64	+110	+162	+203	+226	+255	+246	+232	+203	+148	+52
30	+55	+90	+110	+139	+148	+168	+157	+154	+128	+102	+46
45	+14	+17	+12	+29	+17	+20	+23	+26	+26	+14	+6
60	-64	-72	-96	-125	-122	-128	-130	-136	-125	-104	-70
75	-32	-58	-102	-128	-157	-180	-171	-165	-148	-104	-35
90 (Horiz.)	-46	-78	-119	-174	-200	-235	-223	-209	-191	-130	-58
105	-46	-78	-125	-157	-183	-218	-203	-194	-177	-133	-61
120	-29	-52	-84	-107	-130	-151	-142	-139	-128	-99	-46
135	-9	-9	-14	-17	-35	-38	-44	-32	-35	-35	-23
150	+23	+35	+61	+84	+93	+104	+104	+87	+70	+46	+3
165	+55	+78	+125	+174	+197	+215	+220	+191	+165	+113	+29

Note: + Indicates decrease in diameter.

Table 4d  
DIAMETRIC DISPLACEMENTS, INCHES X 10<sup>4</sup>  
Test 2B Steel Tunnel Model, a/h = 40

0, (Deg) (From Crown)	Surface Pressure (psi)											
	Increasing						Decreasing					
	10	20	40	60	80	100	70	50	30	10	0	
0 (Crown)	+61	+96	+142	+180	+209	+235	+218	+200	+174	+116	+3	
15	+58	+93	+130	+157	+180	+206	+191	+171	+151	+104	+9	
30	+35	+49	+75	+93	+107	+119	+110	+99	+84	+46	-6	
45	+6	+12	0	+6	+14	0	+3	-9	-12	-17	-6	
60	-20	-44	-58	-67	-81	-110	-87	-102	-81	-64	-17	
75	-35	-58	-96	-125	-145	-162	-154	-151	-136	-96	-17	
90 (Springing)	-49	-75	-116	-148	-171	-194	-183	-177	-160	-116	-26	
105	-44	-67	-104	-133	-41	-180	-168	-160	-145	-104	-17	
120	-26	-46	-64	-90	-104	-119	-113	-113	-102	-70	-14	
135	-3	-9	-6	-6	-17	-20	-26	-23	-23	-23	-12	
150	+29	+41	+61	+78	+90	+104	+96	+84	+70	+44	0	
165	+55	+84	+125	+154	+177	+171	+183	+171	+148	+99	+6	

Note: + Indicates decrease in diameter.

Table 4e

DIAMETRIC DISPLACEMENTS, INCHES X 10<sup>4</sup>

Test 3A Alum. Tunnel Model, a/h = 60

$\theta$ , (Deg) (From Crown)	Surface Pressure (psi)											
	Increasing						Decreasing					
	10	20	40	60	80	100	70	50	30	10	0	
0 (Crown)	+41	+75	+130	+180	+218	+258	+232	+218	+188	+136	+32	
15	+35	+67	+116	+162	+194	+232	+215	+194	+168	+122	+26	
30	+23	+41	+70	+93	+116	+133	+125	+113	+93	+64	+12	
45	0	-3	+3	+3	+12	+14	+9	+6	+3	-6	-9	
60	-20	-32	-58	-75	-87	-93	-96	-93	-84	-70	-29	
75	-32	-110	-136	-157	-174	-186	-183	-177	-148	-142	-44	
90 (Springing)	-35	-64	-107	-139	-165	-188	-183	-174	-162	-128	-52	
105	-32	-61	-96	-125	-148	-171	-168	-157	-148	-119	-52	
120	-26	-41	-64	-81	-93	-110	-107	-107	-101	-87	-46	
135	-23	-17	-20	-23	-9	-17	-3	-32	-23	-29	-49	
150	+12	+29	+58	+90	+110	+133	+116	+104	+84	+55	0	
165	+32	+61	+116	+160	+197	+229	+212	+194	+168*	+119	+32	

Note: + Indicates decrease in diameter.

Table 4f

DIAMETRIC DISPLACEMENTS, INCHES X 10<sup>4</sup>  
 Test 3B Alum. Tunnel Model, a/h = 60

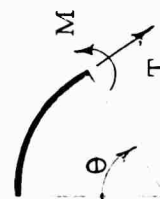
$\theta$ , (Deg) (From Crown)	Surface Pressure (psi)											
	Increasing						Decreasing					
	10	20	40	60	80	100	70	50	30	10	0	
0 (Crown)	+52	+87	+133	+171	+200	+232	+218	+197	+174	+122	+14	
15	+49	+75	+122	+151	+183	+206	+191	+180	+151	+107	+9	
30	+20	+41	+70	+84	+104	+119	+110	+102	+81	+55	+3	
45	0	+58	+3	+6	+6	+12	+9	+6	+3	-6	-6	
60	-23	-38	-55	-67	-75	-87	-84	-81	-72	-58	-17	
75	-38	-55	-110	-128	-139	-142	-148	-142	-133	-87	-20	
90(Springing)	-38	-64	-96	-122	-139	-160	-151	-229	-128	-99	-23	
105	-35	-55	-87	-107	-125	-139	-133	-325	-116	-84	-20	
120	-23	-35	-110	-64	-75	-78	-78	-81	-72	-61	-17	
135	0	0	+20	+29	+38	+23	+12	+20	+23	+14	+23	
150	+26	+46	+70	+90	+113	+130	+113	+104	+90	+55	0	
165	+41	+72	+113	+151	+180	+206	+191	+177	+154	+104	+9	

Note: + Indicates decrease in diameter.

Table 5a

**DIRECT AND BENDING STRESSES, PSI**  
**Test 1A, Steel Tunnel Model,  $a/h = 60$**

$\theta$ , (Deg) (From Crown)	Surface Pressure, (psi)													
	Increasing							Decreasing						
	10	20	40	60	80	100	70	50	30	10	0			
0 (Crown)	$f_D$	- 465	- 600	- 1740	- 2390	- 3100	- 4170	- 3680	- 3080	- 2310	- 1370	- 555		
	$f_B$	+ 975	+ 1500	+ 2400	+ 3080	+ 3680	+ 4500	+ 4130	+ 3830	+ 3450	+ 2630	+ 675		
45	$f_D$	- 360	- 675	- 1520	- 2310	- 3080	- 4230	- 3700	- 2800	- 2180	- 1080	- 360		
	$f_B$	- 150	- 225	- 375	- 450	- 525	- 600	- 600	- 525	- 525	- 3900	+ 300		
90 (Springing)	$f_D$	- 630	- 1125	- 2030	- 3000	- 3980	- 5180	- 3900	- 3080	- 2030	- 1130	- 450		
	$f_B$	- 570	- 810	- 1425	- 1800	- 2180	- 2480	- 2400	- 2480	- 2180	- 1880	- 750		
180 (Invert)	$f_D$	- 285	- 900	- 1265	- 2040	- 2820	- 3930	- 3450	- 3230	- 2490	- 1410	- 495		
	$f_B$	+ 1125	+ 1650	+ 2400	+ 3150	+ 3450	+ 4200	+ 3900	+ 3830	+ 3450	+ 2850	+ 1870		



$$f_B = \frac{6M}{h^2}, + \text{ indicates compression on outside fibers.}$$

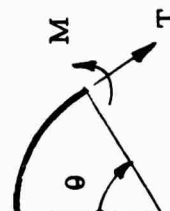
$$f_D = \frac{T}{h}, + \text{ indicates tension.}$$



Table 5b  
DIRECT AND BENDING STRESSES, PSI

Test 1B - Steel Tunnel Model,  $a/h = 60$

$\theta$ , (Deg) (From Crown)		Surface Pressure, (psi)											
		Increasing						Decreasing					
		10	20	40	60	80	100	70	50	30	10	0	
0 (Crown)	$f_D$	-435	-795	-1515	-2160	-2960	-3450	-3120	-1665	-1845	-1095	-165	
	$f_B$	+1575	+2025	+2775	+3450	+3825	+4500	+4050	+3075	+3525	+2625	+525	
45	$f_D$	-510	-915	-1640	-2520	-3330	-3870	-3225	-2505	-1920	-1095	-15	
	$f_B$	-300	-375	-600	-750	-900	-750	-825	-675	-750	-525	+375	
90 (Springing)	$f_D$	-600	-1125	-2020	-3220	-3980	-4870	-3600	-2550	-1650	-900	0	
	$f_B$	-600	-675	-1125	-1575	-1725	-1575	-1800	-1650	-1650	-1350	-600	
180 (Invert)	$f_D$	-435	-705	-1410	-2120	-2740	-3450	-2955	+15	+120	+1020	+1815	
	$f_B$	+675	+1275	+1950	+2325	+2775	+3150	+3075	375	300	150	-1125	



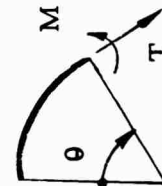
$$f_B = \frac{6M}{h}, + \text{ indicates compression on outside fibers.}$$

$$f_D = \frac{T}{h}, + \text{ indicates tension.}$$

Table 5c

DIRECT AND BENDING STRESSES, PSITest 2A - Steel Tunnel Model,  $a/h = 40$ 

$\theta, (\text{Deg})$ (From Crown)	Surface Pressure, (psi)											
	Increasing						Decreasing					
	10	20	40	60	80	100	70	50	30	10	0	
0 (Crown)	$f_D$	-150	-465	-720	-1185	-1590	-1965	-1605	-1290	-930	-135	-15
	$f_B$	+1650	+2475	+4050	+5175	+6000	+6825	+6525	+6300	+5850	+4425	+1125
45	$f_D$	-420	-705	-1275	-1980	-2550	-3090	-2520	-1965	-1440	-510	+60
	$f_B$	-450	-975	-1425	-1950	-2400	-2550	-2400	-2175	-1800	-900	+450
90 (Springing)	$f_D$	-375	-825	-1500	-2175	-2775	-3450	-2550	-2025	-1425	-600	-150
	$f_B$	-525	-975	-1500	-1875	-2325	-2550	-2400	-2325	-2175	-1800	-900
180 (Invert)	$f_D$	-75	-345	-630	-915	-1260	-1635	-1470	-1335	-945	-465	-135
	$f_B$	+975	+1635	+2550	+3375	+3900	+4575	+4350	+4125	+3825	+2925	+1275



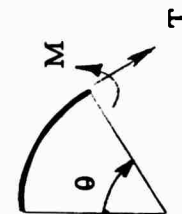
$$f_B = \frac{6M}{h^2}, \text{ + indicates compression on outside fibers.}$$

$$f_D = \frac{T}{h}, \text{ + indicates tension.}$$

Table 5d  
DIRECT AND BENDING STRESSES, FSI

Test 2B - Steel Tunnel Model,  $a/h = 40$

$\theta$ , (Deg) (From Crown)	Surface Pressure, (psi)											
	Increasing						Decreasing					
	10	20	40	60	80	100	70	50	30	10	0	
0 (Crown)	$f_D$	-990	-510	-780	-1185	-1635	-1890	-1500	-1245	-795	-240	-30
	$f_B$	+2175	+3000	+4050	+5025	+5625	+6300	+6000	+5775	+5325	+4200	+300
45	$f_D$	-315	-825	-1200	-1785	-2430	-2925	-2145	-1725	-2550	-435	+45
	$f_B$	-975	-1425	-2040	-2475	-2850	-3075	-2775	-2475	-2100	-1425	+75
90 (Springing)	$f_D$	-375	-750	-1575	-1930	-2775	-3300	-2250	-1800	-300	-450	+75
	$f_B$	-225	-600	-975	-1200	-1425	-1650	-1500	-1350	-600	-1050	-225
180 (Invert)	$f_D$	-30	-240	-645	-765	-1065	-1185	-1050	-855	-405	-135	+180
	$f_B$	+900	+1350	+2175	+2775	+3375	+3975	+3750	+3525	+3225	+2175	+450



$$f_B = \frac{6M}{h^2}, + \text{ indicates compression on outside fibers.}$$

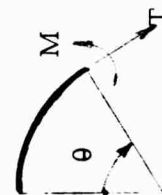
$$f_D = \frac{T}{h}, + \text{ indicates tension.}$$

Table 5e

## DIRECT AND BENDING STRESSES, PSI

Test 3A Aluminum Tunnel Model,  $a/h = 60$ 

	$\theta$ , (Deg) (From Crown)	Surface Pressure, (psi)										
		Increasing						Decreasing				
		10	20	40	60	80	100	70	50	30	10	0
0 (Crown)	$f_D$	-250	- 540	-1005	-1505	-2020	-2560	-2185	-1810	-1355	- 740	+120
	$f_B$	+150	+ 350	+ 625	+ 875	+1000	+1100	+1075	+1100	+1075	+1000	+450
	$f_D$	-365	- 800	-1500	-2295	-3005	-3800	-3085	-2430	-1720	- 895	-110
45	$f_B$	-125	- 250	- 350	- 325	- 475	- 550	- 475	- 450	- 400	- 275	0
	$f_D$	-500	-1000	-1850	-2850	-3675	-4600	-3600	-2750	-1775	- 750	- 50
90 (Springing)	$f_B$	- 50	- 100	- 150	- 200	- 375	- 400	- 400	- 350	- 275	- 250	- 50
	$f_D$	-200	- 485	- 795	-1670	-2205	-2925	-2715	-2215	-1720	- 910	- 80
180 (Invert)	$f_D$	+100	+ 175	+ 575	+ 450	+ 425	+ 575	+ 525	+ 425	+ 400	+ 150	0
	$f_B$											



$$f_B = \frac{6M}{h^2}, \quad + \text{ indicates compression on outside fibers.}$$

$$f_D = \frac{T}{h}, \quad + \text{ indicates tension.}$$

Table 5f

DIRECT AND BENDING STRESSES,  $P_{CI}$

Test 3B Aluminum Tunnel Model,  $a/h = 60$

$\theta$ , (Deg) (From Crown)	Surface Pressure, (psi)											
	Increasing						Decreasing					
	10	20	40	60	80	100	70	50	30	10	0	
0 (Crown)	$f_D$	-255	-535	-975	-1460	-2005	-2440	-2130	-1770	-1310	-730	-90
	$f_B$	+325	+525	+675	+800	+925	+950	+950	+950	+950	+850	+250
45	$f_D$	-485	-855	-1625	-2280	-3030	-3705	-3070	-2455	-1730	-930	-155
	$f_B$	-175	-225	-375	-450	-500	-575	-500	-475	-400	-300	-25
90 (Springing)	$f_D$	-515	-1055	-1950	-2875	-3800	-4625	-3650	-2800	-1800	-775	-25
	$f_B$	+15	-45	-150	-175	-200	-275	-250	-200	-200	-125	+25
180 (Invert)	$f_D$	-270	-565	-1100	-1665	-2195	-2710	-2495	-2230	-1740	-895	+65
	$f_B$	+150	+275	+400	+525	+625	+650	+625	+600	+500	+375	+80

$$f_B = \frac{6M}{h^2}, \quad + \text{ indicates compression on outside fibers.}$$

$$f_D = \frac{T}{h}, \quad + \text{ indicates tension.}$$



Stress, (psi)	$E_c$ (1st Cycle) (psi)	$E_c$ (2nd Cycle) (psi)
10	3700	4450
20	3750	5050
40	4500	5850
60	5450	6700
80	6400	7600
100	7500	8800

#### D. Discussion of Results

According to the theory presented in Section II H, a knowledge of the apparent modulus ( $E^*$ ), foundation modulus ( $k$ ), biaxiality ratio ( $\beta$ ), and the stress ( $\sigma_0$ ) together with the shell properties ( $\bar{E}$  and  $a/h$ ) will enable one to determine the stresses in and the displacements of a buried cylinder. The value of  $\sigma_0$  at the point where the tunnel radial displacements and stresses were measured is assumed equal to the surface pressure for all calculations in this section. Direct determination of  $\sigma_0$  and  $\beta$  requires the measurement of lateral and vertical soil pressures; however, at present no acceptable gage exists for measuring static soil pressure.

From equation 57 it is noted that,  $\frac{ka^2}{\bar{E}h} \angle \frac{9000(60)}{10^7} = 0.054$

when  $ka \leq E^*$ , for all of the tunnel models. Thus neglecting  $\frac{ka^2}{\bar{E}h}$  in equation 57 and solving for the direct stress at the tunnel crown ( $\theta = 0^\circ$ ) and springing ( $\theta = 90^\circ$ ) and then adding and subtracting the resulting two equations give,

$$- \frac{f_D(0^\circ) + f_D(90^\circ)}{\sigma_0 a/h} = 1 + \beta + \frac{ka}{E^*}, \quad (62a)$$

and

$$\frac{f_D(0^\circ) - 2 f_D(90^\circ)}{\sigma_0 a/h} = 1 + \frac{ka}{E^*} - \frac{ka}{E^*} \frac{E^*}{\sigma_0} x_2 \quad (62b)$$

where  $f_D(0^\circ)$  is the crown direct stress. From these equations, it is possible to solve for  $ka/E^*$  and  $\beta$  since all other values are known for the test series (assuming  $\sigma_0$  equals the surface pressure). Presumably, the values of  $ka/E^*$  and  $\beta$  are constant for a given surface pressure level for each tunnel model;

ARMOUR RESEARCH FOUNDATION OF ILLINOIS INSTITUTE OF TECHNOLOGY

however, attempts to evaluate the quantities from equations 62 result in rather wide variations. The discrepancies occur primarily because the soil is not in a state of uniaxial strain. This is evident since the rigid body tunnel motions (Figure 18) are only about 1/3 the surface displacements instead of 1/2 (Tunnel located at mid-depth). Also, the average stress to strain ratio of the soil, based on surface displacements and pressures, results in values of  $E^*$  that are 2 to 4 times those measured in the consolidometer. The conclusion is that there exists appreciable shear stresses at the soil-containment vessel interface.

The primary source of error encountered in attempting to solve for  $\beta$  and  $ka/E^*$  from equations 62, arises from the evaluation of the parameter  $E^*x_2/\sigma_0$ . This parameter represents (2nd mode tunnel displacement ratio/free-field strain) which cannot be obtained with sufficient precision since the free-field strain at the tunnel is not accurately known.

From equation 62a we observe that

$$R = - \frac{f_D(0^\circ) + f_D(90^\circ)}{\sigma_0 a/h}$$

should be nearly the same for each test if  $\beta$  and  $ka/E^*$  are invariant. From the measured values of direct stress (table 5) at the 20, 60 and 100-psi surface pressure levels, the following values for the ratio (R) are obtained:

Test	Surface Pressure			Average
	20 psi	60 psi	100 psi	
1A	1.56	1.45	1.54	1.52
1B	1.56	1.49	1.39	1.48
2A	1.54	1.34	1.31	1.40
2B	1.41	1.22	1.21	1.28
3A	1.26	1.23	1.22	1.24
3B	1.34	1.23	1.20	1.26

Overall Average (R) = 1.36

All values are within 15 percent of the overall average value. The accuracy of the value  $R$  is somewhat questionable in view of the assumption that the vertical free-field pressure ( $\sigma_o$ ) equals the surface pressure. It is also noted that both the ratio  $R$  and the average soil surface deflections (see Fig. 18) decrease with progressive tests. This indicates that the free-field vertical pressure  $\sigma_o$ , at the tunnel model instrumentation section, decreases with progressive tests due to increased friction at the containment vessel wall. Wall friction is obviously a function of the Teflon lining condition which had increased wrinkling with each test. Based on these observations it seems plausible that the value of  $\sigma_o$ , used in calculating the ratio  $R$ , becomes increasingly smaller with each test. This effect would yield a more nearly constant value for the ratio  $R$  than calculated above. Thus, it appears that this aspect of the theory ( $R = \text{constant for a given soil}$ ) is acceptable.

According to equation 57, the direct stress at the crown and invert ( $\theta = 0$ , and  $180^\circ$ ) are equal. Examination of table 5 reveals that the crown stress is larger for Tests 1 and 2 and the invert stress larger for Test 3. This is probably due, in part, to the manner in which the stresses were corrected to eliminate the longitudinal loading effects. Generally the differences are less than 15 percent at the 100-psi pressure level. It is also noted that the vertical diameter shortening is larger than the horizontal increase. Some difference is expected from theory since the radial displacement is given by

$$w = a_o + a_2 \cos 2\theta$$

where

$$a_o \simeq \frac{\sigma_o a^2}{2 E h} \left( 1 + \beta + \frac{ka}{E^*} \right)$$

Thus a difference in orthogonal diameter change of

$2(w \Big|_{\theta} + w \Big|_{\theta + 90^\circ}) = 4a_o$  can be accounted for from the theory. For  $\sigma_o = 100$  psi and assuming  $1 + \beta + \frac{ka}{E^*} < 2$  the following maximum diametric displacement differences ( $4a_o$ ) for each test are reasonable.



<u>Test</u>	<u>max <math>4a_o</math>, (in.)</u>
1A, B (Steel model, $a/h = 60$ )	$24 \times 10^{-4}$
2A, B (Steel model, $a/h = 40$ )	$16 \times 10^{-4}$
3A, B (Aluminum model, $a/h = 60$ )	$72 \times 10^{-4}$

The value  $72 \times 10^{-4}$  is not exceeded for the most flexible tunnel model (tests 3A and B) when the surface pressure equals 100 psi. The value  $24 \times 10^{-4}$  is slightly exceeded for the "near" vertical-horizontal diameters for tests 1A and B. The largest variations from the value were obtained in the tests on the model with the highest bending rigidity (Test 2A and 2B).

It is interesting to note that the Iowa Formula (11) for flexible pipe culverts with a bedding angle of 180 deg gives

$$x_2 = \frac{1.5 \sigma_o}{\frac{18 \bar{E} I}{a^3} + 1.1 ka}$$

as compared to equation 60

$$x_2 = \frac{\sigma_o (1 - \beta + ka/E^*)}{\frac{18 \bar{E} I}{a^3} + 2 ka}$$

The expression for  $ka/E^*$  from equation 60 is

$$\frac{ka}{E^*} = \frac{1 - \beta - \frac{18 \bar{E} I}{a^3} \frac{x_2}{\sigma_o}}{\frac{2x_2}{\sigma_o/E^*} - 1} \quad (62c)$$

Assuming a free-field strain ( $\sigma_o/E^*$ ) at the tunnel instrumentation section equal to the average strain, based on the soil surface displacements, there results,

$$\frac{ka}{E^*} = \frac{1 - \beta - \frac{1.5 \bar{E} I}{a^3} \frac{\delta_o - \delta_{90}}{\sigma_o}}{\frac{6(\delta_o - \delta_{90})}{\Delta_{sur}} - 1} \quad (62d)$$

where

$\delta_o$  = vertical tunnel diametric deflection ( Table 4,  $\theta = 0$  deg)

$\delta_{90}$  = horizontal tunnel diametric deflection ( Table 4,  $\theta = 90$  deg)

$\Delta_{sur}$  = average surface displacement ( Fig. 18)

The third term in the numerator of equations 62c and 62d is small compared to unity for all tests and can be neglected. The denominator has the following maximum and minimum values for increasing and decreasing surface pressures greater than 20 psi.

Test	$\frac{6(\delta_o - \delta_{90})}{\Delta_{sur}} - 1$	
	Max	Min
1A, B	.73	.46
2A, B	.91	.73
3A, B	1.45	.74

The average denominator value for all tests, with pressure greater than 10 psi, is 0.854. Since  $k_a, E^*$  and  $\beta$  are soil properties and the numerator of equation 62d is  $\simeq 1 - \beta$ , the value  $6(\delta_o - \delta_{90})/\Delta_{sur}$  and hence the numerator of equation 62d should remain invariant for the test series, according to the theory. It is believed that the variation in the denominator (indicated by the tabulated maximum and minimum values) is the direct result of the assumption made for the free-field strain ( $\sigma_o/E^*$ ). In reality, the free-field strain at the tunnel instrumentation section is certainly larger than the average strain and the ratio of free-field strain at the tunnel to average strain probably increases with increasing wall friction. If these hypotheses are assumed, the numerator of equation 62d would tend to a more stable value.

## SYMBOL INDEX

### Section III

$a$	shell radius
$a_n$	peak shell modal displacement
$E$	Young's modulus of shell
$\bar{E}$	$E/(1 - \nu^2)$
$E^*$	apparent modulus of soil
$E_c$	soil modulus in confined compression
$f_D(\theta)$	shell static direct stress
$f_B(\theta)$	shell static bending stress
$h$	shell thickness
$k$	foundation modulus
$w$	shell radial displacement
$x_n$	$a_n/a$
$\beta$	free-field stress biaxial ratio
$\theta$	angular coordinate from crown
$\sigma_o$	peak free-field pressure in x-direction

#### IV. EFFECTS OF DIFFERENTIAL HORIZONTAL SOIL DISPLACEMENTS

##### A. Introduction

The analysis given in this section can be used to estimate longitudinal bending and shear stresses in silo linings resulting from given differential horizontal soil displacements. The rigidity of the silo lining lies between two obvious extremes, infinite and zero rigidity. A lining with no rigidity will conform to the free-field displacements as shown in figure 20b and no longitudinal bending or shear stresses would be introduced while a lining with infinite bending rigidity remains straight and does not conform to the free-field displacements. The latter approach clearly yields maximum stresses. The following investigation uses the energy method and treats the general case of silo linings that possess both bending and shear flexibility. This analysis follows closely the method presented in reference 2. The primary addition is the inclusion of rigid body shell rotation to account for an unsymmetrical free-field displacement profile.

##### B. Analysis

If a lining has longitudinal rigidity it will tend to remain straight and not conform to the free-field profile. It is assumed that the force exerted by the soil on the lining is directly proportional to the relative radial displacement of the lining and the corresponding free-field particles (elastic foundation).

The displacement of the lining is obtained by assuming expressions for orthogonal displacement components that contain undetermined coefficients that satisfy the boundary conditions. The free-field deviations from a straight line, AB, (Fig. 20c) can be represented as a Fourier series. The shell displacement coefficients are then obtained by minimizing the strain energy of the shell-foundation system.

The radial, tangential and axial displacements of the middle surface of the shell shown in figure 21 are assumed as

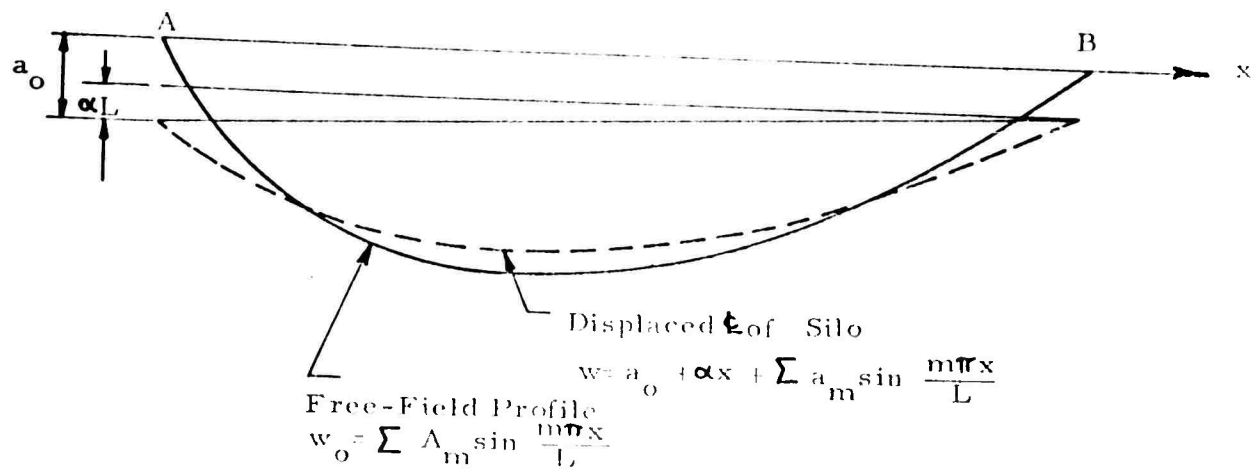
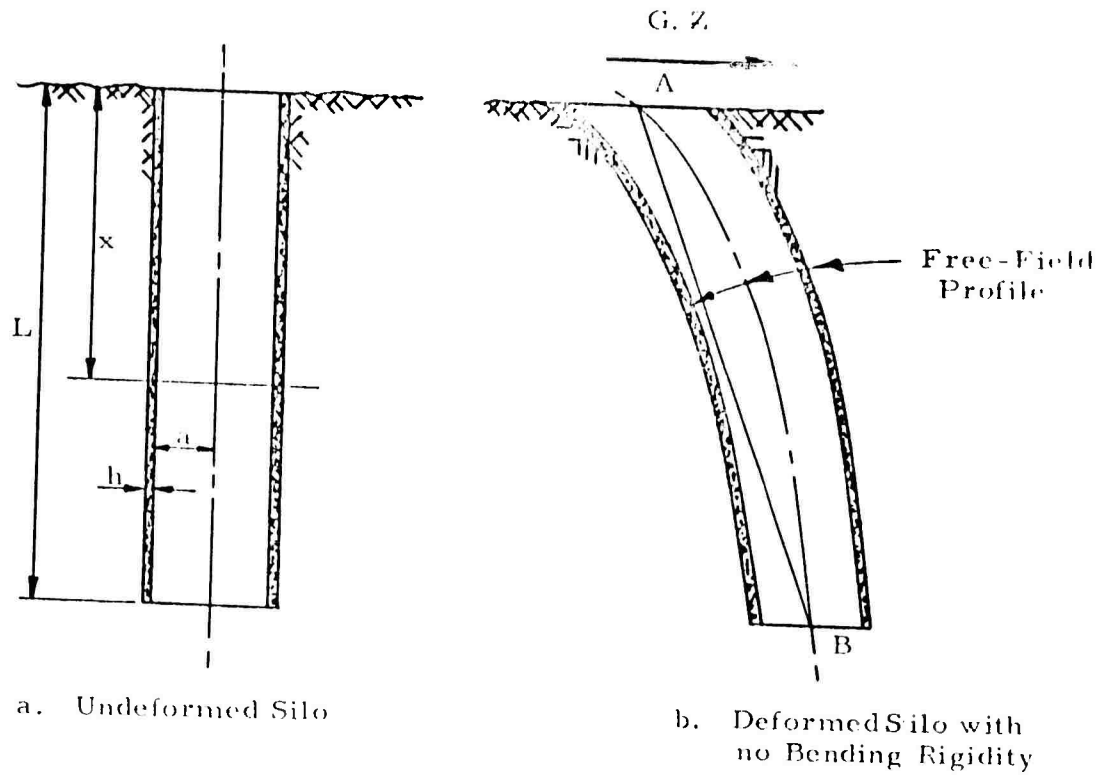


Fig. 20 SECTIONAL ELEVATIONS OF SILO LINING

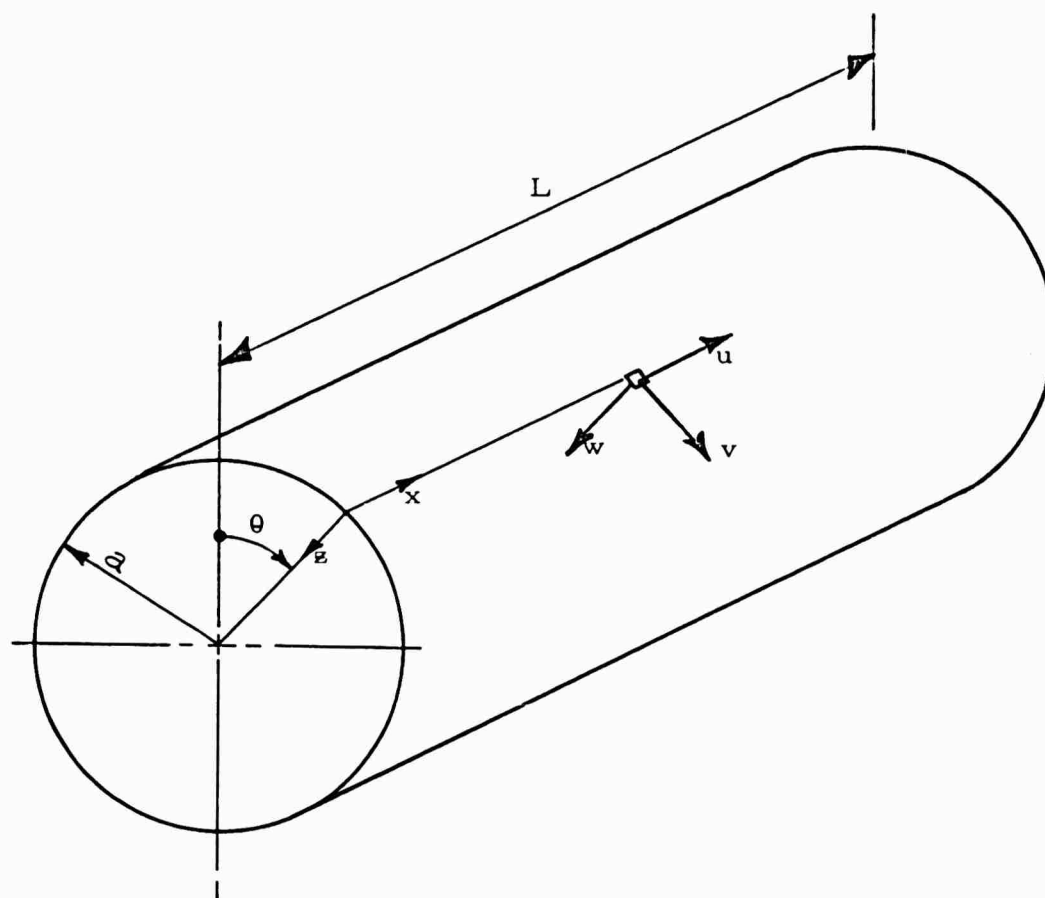


Fig. 21 SHELL COORDINATE SYSTEM

$$\left. \begin{aligned} w &= (a_o + \alpha x) \cos \theta + \sum_{m,n=1}^{\infty} a_{mn} \sin \frac{m\pi x}{L} \cos n\theta \\ v &= (a_o + \alpha x) \sin \theta + \sum_{m,n=1}^{\infty} \frac{a_{mn}}{n} \sin \frac{m\pi x}{L} \sin n\theta \\ u &= \alpha a \cos \theta + \sum_{m,n=1}^{\infty} b_{mn} \cos \frac{m\pi x}{L} \cos n\theta \end{aligned} \right\} \quad (63)$$

where  $\alpha$ ,  $a_o$ ,  $b_{mn}$  and  $a_{mn}$  are undetermined coefficients.

The undisturbed radial displacements of the free-field at a position corresponding to the middle surface of the shell is

$$w_o = \sum_{m=1}^{\infty} A_m \sin \frac{m\pi x}{L} \cos \theta \quad (64)$$

where  $A_m$  are given free-field displacement amplitudes from the straight line AB connecting the shell end sections (figures 20b and 20c).

An expression for the strain energy of the shell is given (10) as

$$\begin{aligned} U_s &= \frac{\bar{E} h a}{2} \int_0^L \int_0^{2\pi} \left[ u_x^2 + \frac{(v_\theta - w)^2}{a^2} + \frac{2\nu}{a} u_x (v_\theta - w) + \frac{1-\nu}{2} \left( v_x + \frac{u_\theta}{a} \right)^2 \right] dx d\theta + \\ &+ \frac{\bar{E} h^3 a}{24} \int_0^L \int_0^{2\pi} \left[ w_{xx}^2 + \frac{(w_{\theta\theta} + w)^2}{a^4} + \frac{2\nu}{a^2} w_{xx} (w_{\theta\theta} + w) + \right. \\ &\left. + \frac{2(1-\nu)}{a^2} \left( w_{x\theta} + \frac{v_x}{2} - \frac{u_\theta}{2a} \right)^2 \right] dx d\theta \end{aligned} \quad (65a)$$

where

$$u_x = \frac{\partial u}{\partial x}, \quad w_{x\theta} = \frac{\partial^2 w}{\partial x \partial \theta}, \quad \text{etc.}$$

Substituting the expressions for the shell displacements (equations 63) into equation 65a and performing the indicated operations gives the following shell strain energy expression,

$$\begin{aligned}
 U_s = & \frac{\bar{E} h a L \pi}{4} \sum_{m, n=1}^{\infty} \left[ \frac{m^2 \pi^2}{L^2} b_{mn}^2 + \frac{1-\nu}{2} \left( \frac{\pi m}{n L} a_{mn} - \frac{n}{a} b_{mn} \right)^2 \right] + \\
 & + \frac{\bar{E} h^3 a L \pi}{48} \sum_{m, n=1}^{\infty} \left\{ \left[ \frac{m^4 \pi^4}{L^4} + \frac{(n^2-1)^2}{a^4} + \frac{2\nu}{a^2} \frac{m^2 \pi^2}{L^2} (n^2-1) \right] a_{mn}^2 + \right. \\
 & \left. + \frac{2(1-\nu)}{a^2} \left[ \left( \frac{m \pi}{2 n L} - \frac{m n \pi}{L} \right) a_{mn} + \frac{n}{2 a} b_{mn} \right]^2 \right\}, \quad (65b)
 \end{aligned}$$

The strain energy of the foundation is

$$U_F = \frac{k a}{2} \int_0^L \int_0^{2\pi} (w - w_o)^2 dx d\theta, \quad (66a)$$

or, upon substitution of equation 63 and 64,

$$\begin{aligned}
 U_F = & \frac{k a L \pi}{4} \left\{ 2 \left( \frac{\alpha^2 L^2}{3} + \alpha a_o L + a_o^2 \right) + \frac{8 a_o + 4 \alpha L}{\pi} \sum_{m=1, 3, 5}^{\infty} \frac{a_{m1} - A_m}{m} \right. \\
 & \left. - \frac{4 \alpha L}{\pi} \sum_{m=2, 4, 6}^{\infty} \frac{a_{m1} - A_m}{m} + \sum_{m, n=1}^{\infty} (a_{mn}^2 - 2 a_{m1} A_m - A_m^2) \right\} \quad (66b)
 \end{aligned}$$

The total energy is

$$U = U_s + U_F. \quad (67a)$$



The undetermined shell displacement amplitudes are evaluated by application of Castigliano's Theorem of Least Work, thus

$$\frac{\partial U}{\partial \alpha} = \frac{\partial U}{\partial a_0} = \frac{\partial U}{\partial a_{mn}} = \frac{\partial U}{\partial b_{mn}} = 0 \quad m, n = 1, 2 \dots \quad (67b)$$

From equations 65b, 66b, 67a and the last two equations of 67b we obtain a set of linear algebraic equations in  $a_{mn}$  and  $b_{mn}$ . For  $n > 1$  the equations are homogeneous and the result is

$$a_{mn} = b_{mn} = 0, \quad n > 1. \quad (68)$$

For  $n = 1$  and dropping the  $n$  subscript since it is always unity, we obtain, after algebraic manipulation to eliminate  $b_m$ ,

$$\left\{ \frac{m^2 \pi a}{L} \left( 1 + \frac{h^2}{12a^2} \right) + \frac{m^4 \pi^3 a h^2}{6(1-\nu)L^3} + \frac{2kaL}{\pi \bar{E} h(1-\nu)} + \right. \\ \left. - \frac{m^2 \pi a (1-\nu) \left( 1 + \frac{h^2}{12a^2} \right)}{2L \left[ \frac{m^2 \pi^2 a^2}{L^2} + \frac{(1-\nu)}{2} \left( 1 + \frac{h^2}{12a^2} \right) \right]} \right\} a_m = \\ \frac{2kaL}{\pi \bar{E} h(1-\nu)} \left\{ \begin{aligned} &A_m + \frac{8}{m \pi^2} \sum_{n=1, 3, 5}^{\infty} \frac{a_n - A_n}{n}, \quad m \text{ Odd} \\ &A_m + \frac{4L}{m \pi^2 \left[ \frac{\bar{E} h a (1-\nu)}{kaL} \left( 1 + \frac{h^2}{12a^2} \right) + \frac{L}{6} \right]} \sum_{n=2, 4, 6}^{\infty} \frac{a_n - A_n}{n}, \quad m \text{ Even} \end{aligned} \right. \quad (69a)$$

$$(69b)$$

Equations 69a and 69b respectively produce two sets of simultaneous equations sufficient to determine all  $a_m$  ( $m = 1, 2, 3 \dots$ ). It is important to note that if all even (or odd)  $A_m$  are zero, all even (or odd)  $a_m$  equal zero.

From the first and second of equations 67b and with all  $a_m$  determined from equations 69a and 69b we find the rigid body coefficients of the shell displacements,

$$\alpha = \frac{12}{\pi L} \sum_{m=2,4,6}^{\infty} \frac{a_m - A_m}{m} \quad (69c)$$

$$a_0 = -\frac{L}{2} \alpha - \frac{2}{\pi} \sum_{m=1,3,5}^{\infty} \frac{a_m - A_m}{m} \quad (69d)$$

Also

$$b_m = \frac{(1 + \frac{h^2}{12a^2}) m \pi a (1 - \nu)}{\frac{2\pi^2 m^2 a^2}{L} + (1 - \nu) L (1 + \frac{h^2}{12a^2})} a_m, \quad m = 1, 2, \dots \quad (69e)$$

The shell displacements can now be obtained from equations 63 where summation over  $n$  is neglected or  $n$  is set equal to unity. The resulting expressions for displacement can be used to determine stresses directly; however, several displacement modes are generally required to accurately determine stresses. Obviously the solution of the simultaneous equations (69a and 69b) will require a major effort if a large number of coefficients ( $a_n$ ) are required. The work required to find stresses accurately is significantly reduced by employing the computed shell displacements to determine the shell loading using only a limited number of the lower displacement modes. The shear and moment are then readily determined from this loading.

The radial pressure acting on the surface of the shell is

$$P = k(w_0 - w)$$

$$P = k \left[ -\alpha x - a_0 + \sum_{n=1}^{\infty} (A_n - a_n) \sin \frac{n\pi x}{L} \right] \cos \theta. \quad (70a)$$

The resultant lateral load per unit length of the shell is

$$F = \int_0^{2\pi} p a \cos \theta d\theta$$

$$F = \pi k a \left[ -\alpha x - a_0 + \sum_{n=1}^{\infty} (A_n - a_n) \sin \frac{n\pi x}{L} \right]. \quad (70b)$$

The shear and bending moment are found from

$$V = \int_0^x F dx$$

$$V = \pi k a \left[ -\alpha \frac{x^2}{2} - a_0 x + \frac{L}{\pi} \sum_{n=1}^{\infty} \frac{A_n - a_n}{n} (1 - \cos \frac{n\pi x}{L}) \right], \quad (70c)$$

and

$$M = \int_0^x V dx$$

$$M = \pi k a \left[ -\alpha \frac{x^3}{6} - a_0 \frac{x^2}{2} + \frac{L}{\pi} \sum_{n=1}^{\infty} \frac{A_n - a_n}{n} \left( x - \frac{L}{n\pi} \sin \frac{n\pi x}{L} \right) \right]. \quad (70d)$$

The elastic extreme fiber bending stresses and the maximum shear stress for a reinforced concrete silo lining with no axial load can be found from the following formulas: (Uniform distribution of the reinforcing steel at each face and a distance of 4-in. between the center of the bar and the concrete surface is assumed)

$$f_c = \frac{Mc_c}{I}, \text{ Concrete Stress}$$

$$f_s = \frac{nMc_s}{I}, \text{ Reinforcing Steel Stress} \quad (71)$$

$$\tau = \frac{VQ}{2Ih}, \text{ Shear Stress (Cracked Section)}$$

where (see Fig. 22),

$$c_c = a + \frac{h}{2} - \bar{y}$$

$$c_s = a + \frac{h}{2} + \bar{y} - 4"$$

$$\bar{y} = a \cos \theta$$

$$I = (\theta + \sin \theta \cos \theta) \left( a^2 + \frac{h^2}{4} \right) ah + \pi hnp \left( a^3 + \frac{3}{4} ah^2 + 12 ah + \right. \\ \left. + 48a \right) - 2 ha^3 \left( 1 + \frac{h^2}{12a^2} \right) \sin \theta \cos \theta$$

$$Q = 2npa^2h \left\{ (\pi - \theta) \cos \theta + \left[ 1 + \left( \frac{h}{2a} \right)^2 - \frac{4h}{a^2} \right] \sin \theta \right\}$$

$n$  = ratio of modulus of elasticity of steel to that of concrete

$p$  = ratio of total longitudinal steel area to gross concrete area.

and  $\theta$  is found as a root to the equation

$$\theta - \left( 1 + \frac{h^2}{12a^2} \right) \tan \theta + \pi np = 0. \quad (72)$$

ARMOUR RESEARCH FOUNDATION OF ILLINOIS INSTITUTE OF TECHNOLOGY

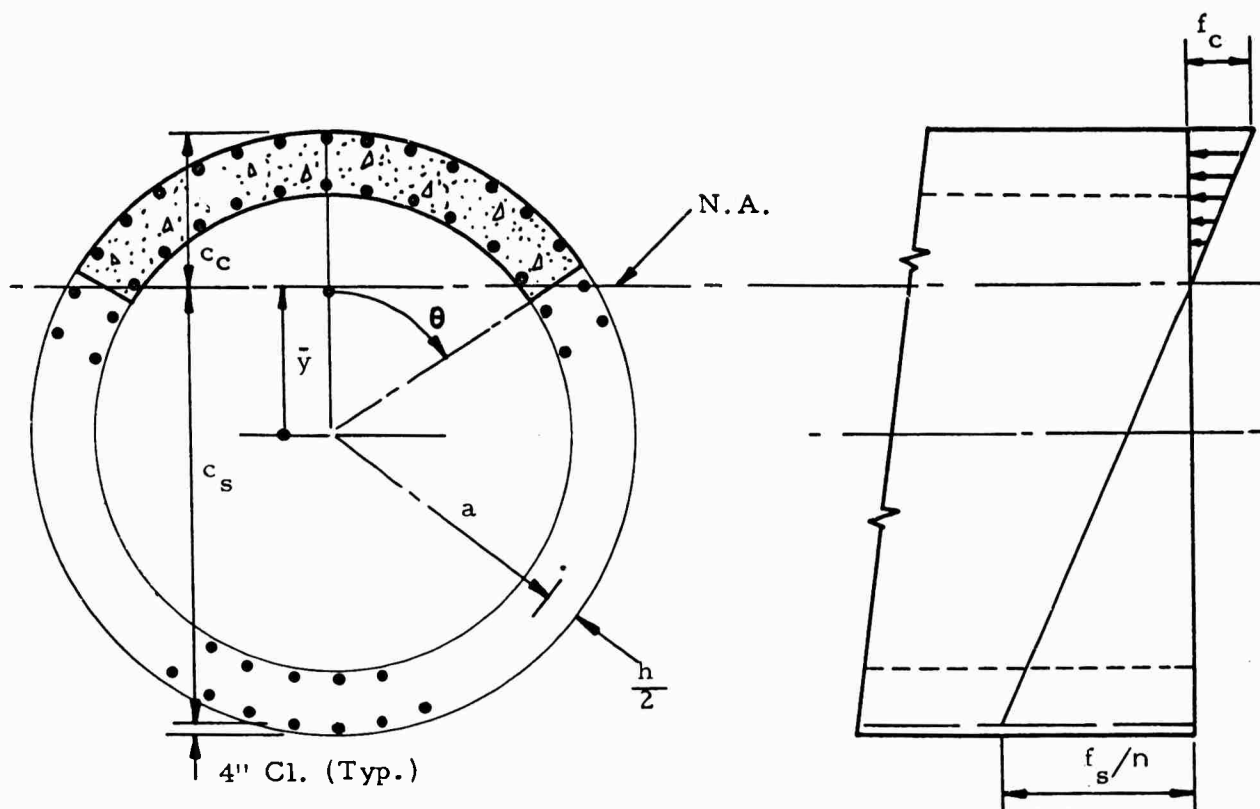


Fig. 22 REINFORCED CONCRETE SHELL PARAMETERS  
(ELASTIC STRESSES)

A plastic analysis has been employed to obtain the following expression for the ultimate resisting moment of the silo lining. A constant concrete compressive stress of  $0.85 f'_c$  and constant compressive and tension steel stress of  $f_{yp}$  is assumed.

$$M_{ult.} = 2 p f_{yp} a^2 h (\pi - \theta_p) \cos \theta_p + \left[ 1 + \left( \frac{h}{2a} \right)^2 + \left( \frac{2}{a} \right)^2 - \frac{4h}{a^2} \right] \sin \theta_p \quad (73)$$

where

$f_{yp}$  = yield stress of reinforcing steel

$$\theta_p = \pi p / (2p + 0.85 \frac{f'_c}{f_{yp}})$$

ARMOUR RESEARCH FOUNDATION OF ILLINOIS INSTITUTE OF TECHNOLOGY

The procedure is illustrated in the following example for a concrete silo 40 ft in diameter, 160 ft deep with a 24-in wall thickness. A homogeneous shell with  $E = 3 \times 10^6$  psi and  $\nu = 0$  and a value of  $ka = 5000$  psi is assumed. A typical horizontal displacement profile of the free-field is shown in figure 23. A three term approximation of the given profile is used in this example defined by the following coefficients,

$$A_1 = 0.75 \text{ in.}$$

$$A_2 = 0.185 \text{ in.}$$

$$A_3 = 0.113 \text{ in.}$$

$$A_n = 0, n > 3$$

From equations 69a and 69b and considering only five displacement modes we obtain as the solution of the simultaneous equations

$$a_1 = 0.0860 \text{ in.}$$

$$a_4 = 0.0158 \text{ in.}$$

$$a_2 = 0.0881 \text{ in.}$$

$$a_5 = -0.0011 \text{ in.}$$

$$a_3 = -0.0024 \text{ in.}$$

Substituting these values into equations 69c and 69d,

$$\alpha = -0.888 \times 10^{-4} \text{ in. /in.}$$

$$a_0 = 0.5326 \text{ in.}$$

The displaced center line of the silo lining using these coefficients is illustrated in figure 23. The displaced center line of a rigid silo is also shown. The rigid silo displacement coefficients ( $a_0$  and  $\alpha$ ) are found from equation 69c and 69d where all  $a_n = 0$  for  $n > 0$ . The resultant load, shear, and bending moment are shown in figure 23 for three flexibility assumptions, (1) the rigid silo, (2) three displacement modes  $a_1 \dots a_3 \neq 0$  and (3) five displacement modes  $a_1 \dots a_5 \neq 0$ . It is important to note that only minor differences exist between the three and five mode curves.

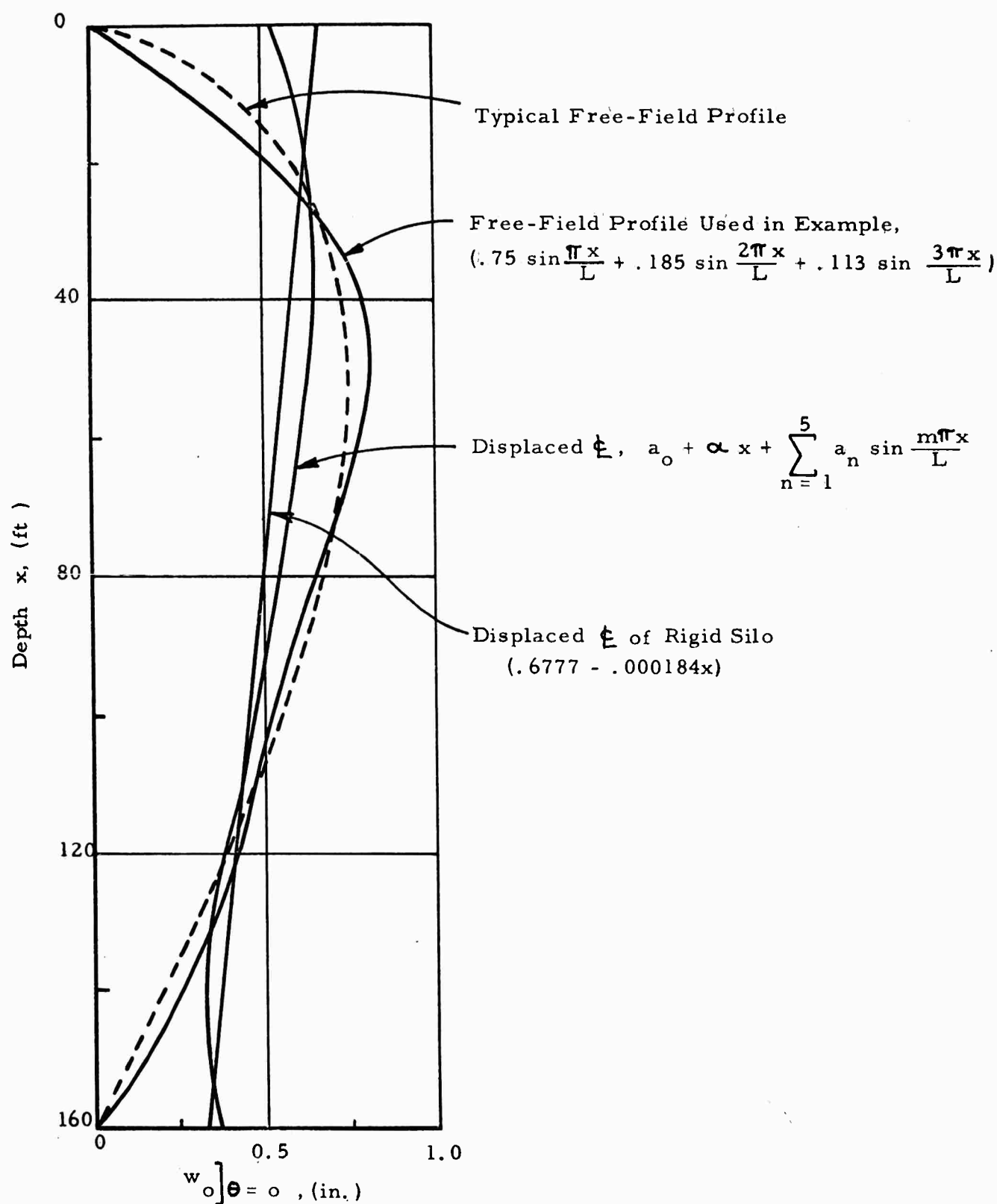


Fig. 23 FREE - FIELD AND SILO HORIZONTAL DISPLACEMENTS

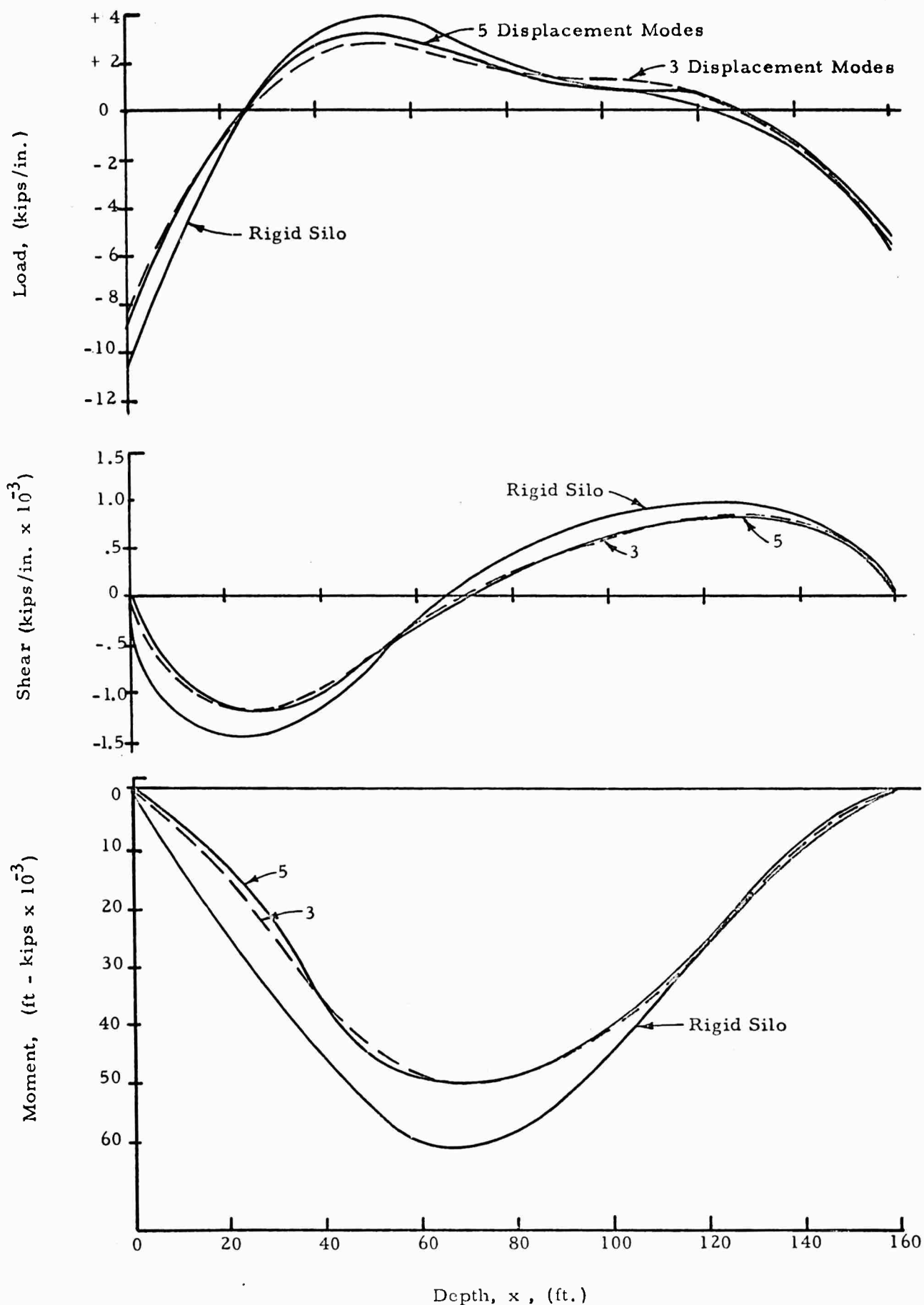


Fig. 24 LOAD, SHEAR AND MOMENT DIAGRAM



The ultimate resisting moment, ratio of maximum computed moment to ultimate resisting moment, and maximum elastic stresses for three percentages of longitudinal reinforcing steel are given in table 6 for the example utilizing the five displacement mode results.

Table 6  
DIFFERENTIAL HORIZONTAL DISPLACEMENT RESULTS, SUMMARY

for  $a = 20$  ft,  $h = 2$  ft,  $L = 160$  ft,  $E = 3 \times 10^6$  psi,  $k_a = 5000$  psi,  $\nu = 0$

$A_1 = 0.75$  in,  $A_2 = 0.185$  in,  $A_3 = 0.113$  in.

Max Radial Pressure = 11.2 psi

Max Lateral Load = 8.4 kips per in.

Max Shear = 1200 kips

Max Moment = 50,000 ft-kips

Max  $\frac{VQ}{2Ih} = 0.066$  ksi

Five Mode Results  
(see Figure 24)

Percentage of Longitudinal Steel	Resisting Moment, (ft-kips) (Ultimate Strength)*	Max. Applied Mom. Ult. Resist. Mom.	Elastic Stresses (ksi)**	
			Max $f_s$	Max $f_c$
0.5	134,500 <sup>1k</sup>	.456	20.15	.336
1.0	257,000 <sup>1k</sup>	.238	13.55	.326
2.0	467,000 <sup>1k</sup>	.131	9.02	.310
				.067
				.086
				.109

\*  $f'_c = 3000$  psi,  $f_{yp} = 38,000$  psi

\*\*  $n = 10$

## SYMBOL INDEX

### Section IV

$a$	Shell Radius
$A_m$	Free-Field Displacement Coefficients
$a_{mn}, a_m$ $b_{mn}, b_m$	Shell Displacement Coefficients
$c_c, c_s$	Distance from Neutral Axis to Extreme Concrete and Steel Fibers
$E$	Young's Modulus of Shell
$\bar{E}$	$= E/(1 - \nu)$
$F$	Lateral Load
$f_c, f_s$	Concrete and Steel Stress
$f_{yp}$	Yield Stress of Reinforcing Steel
$h$	Shell Thickness
$k$	Foundation Modulus
$L$	Shell Length
$M$	Bending Moment
$n$	Ratio of Steel Area to Gross Concrete Area
$p$	Ratio of Young's Modulus of Steel to that of concrete
$P$	Radial Pressure
$U_s, U_F$	Shell and Foundation Strain Energy
$u, v, w$	Shell Displacements
$V$	Shear
$w_o$	Free-Field Radial Displacement
$x, z$	Shell Coordinate
$\alpha$	Shell Displacement Coefficient
$\theta$	Shell Coordinate
$\nu$	Poisson's Ratio
$\tau$	Shear Stress

## V. AXIAL LOADING OF SILO LININGS

### A. Introduction

As discussed in Section I, the silo lining will be subjected to axial loading generated by blast pressure applied directly to the silo cover and by longitudinal surface shear or skin friction between the structure and the surrounding soil medium. When the silo cover is supported directly on the silo lining (monolithic cover), axial loads are transmitted directly to the lining by air-blast pressure on the cover. The dynamic effects of the rapid application of this cover load are discussed in Appendix A. The axial loading of silo linings considered in this section is treated as a static problem, i. e., the air-blast pressure surface loading is taken as a static pressure. Since silo linings have much more rigidity in the vertical direction than the soil they replace, there is relative vertical motion between the structure and the surrounding soil medium. This relative motion, illustrated schematically in figure 25, generates shearing stresses at the silo-soil interface that produce axial silo loads in their own right.

For a silo with monolithic cover, the skin friction produces axial loading in addition to that generated from the cover loading. When the silo cover is supported on a foundation independent of the silo lining, the skin friction is the only source of axial loading. Often the axial loads are sufficiently large to control the thickness of the lining. An empirical method that is commonly employed for determining skin friction magnitudes involves two simplifying assumptions; 1) the normal stress acting on the lining is the same as the free-field horizontal stress, 2) the friction stress is found by multiplying the normal stress by the tangent of the soil's angle of internal friction. The skin friction analysis presented in this section considers the equilibrium of a conical wedge of soil adjacent to the silo that is in a state of impending downward motion relative to the silo. Expressions are derived for upper bound values of the surface shear stress for silo structures with both independent and integral covers.

Push-out tests of walls embedded in sand were presented in the first interim report (7) to determine the usefulness of the upper bound value

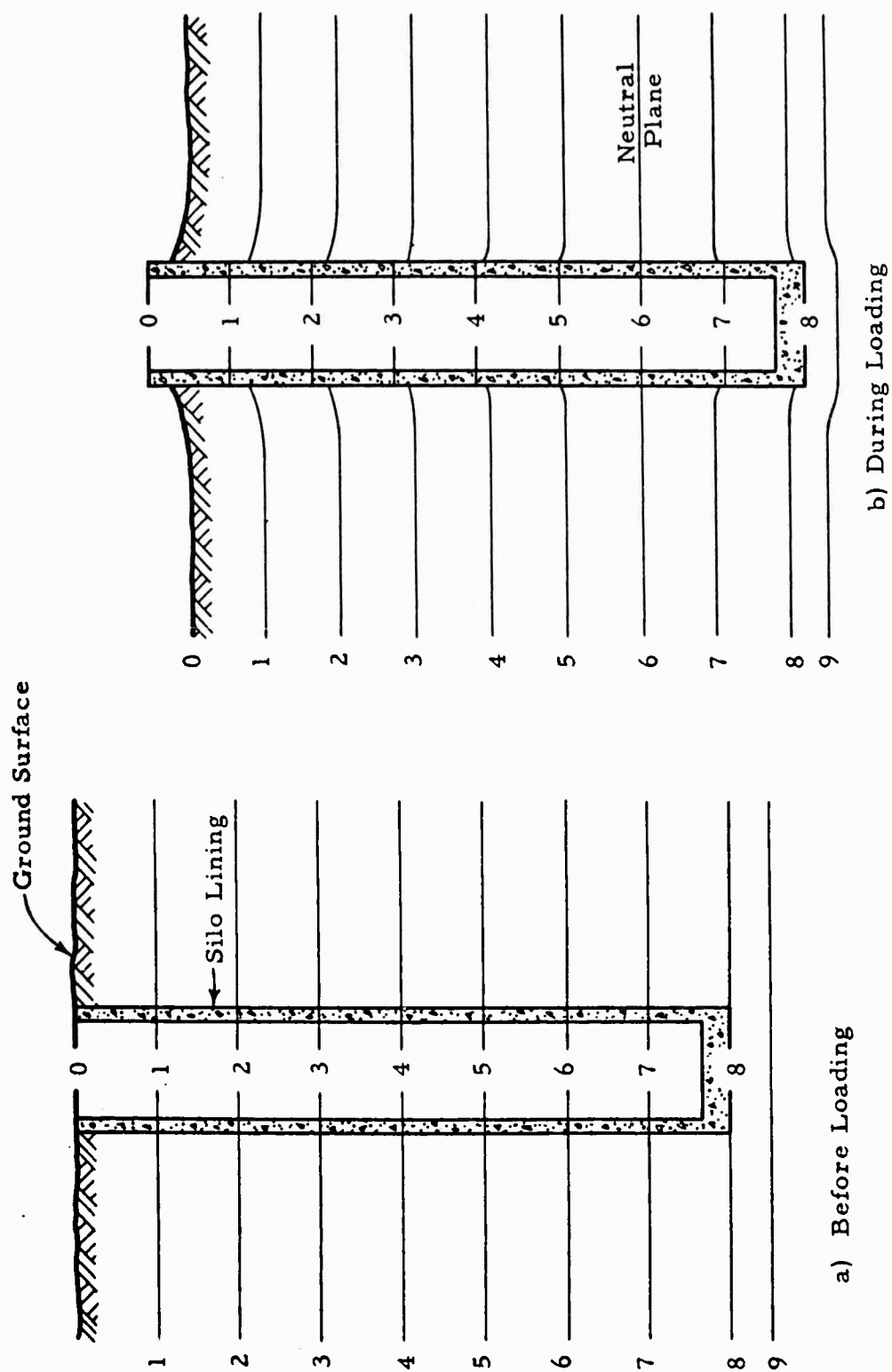


Fig. 25 RELATIVE VERTICAL DISPLACEMENT OF SOIL AND STRUCTURE

given by the theory. Good comparison was obtained between test results and the theory. Similar push-out tests have been performed on a small silo model. Comparison between the measured and theoretical skin friction is fair for the silo model push-out test series but cannot be considered as entirely satisfactory in view of the difference encountered; i. e., the measured friction force was approximately 20 percent higher for some of the tests than the value given by the upper bound theory. Tests on a segmented silo model with surface pressure up to 275 psi are also given. These tests were inconclusive since the axial rigidity of the model was too low for the soil employed (dense Ottawa sand).

### B. Analysis

It is clear from the preceding discussion that axial load will be transmitted through the soil to the structure by shear, since the silo lining has much more axial rigidity than the soil it replaces. That is, relative vertical displacement of the soil adjacent to the lining with respect to the structure (see figure 25) causes shear stress at the interface. Under loading there is a downward displacement of the soil with respect to the structure extending from the surface to the neutral plane, (the plane at which there is no relative motion). Below the neutral plane, the relative displacement of the soil with respect to the structure is upward. The location of the neutral plane is determined by the requirement that the structure be in equilibrium under the action of vertical forces. The axial force in the lining is a maximum at the neutral plane and will be equal to the sum of the loads transmitted directly by the cover plus the sum of the friction forces above this plane. Thus, the resulting problem becomes the determination of the sum of the friction forces acting on the silo above the neutral plane. The following analyses apply to cases where the silo cover is supported independent of the lining (independent cover case) and where the silo cover is an integral part of the silo lining (monolithic cover case).

In both instances the analyses involve the assumption that there exists a region of impending failure bounded by the cylindrical surface of the silo lining (AB) and a conical surface (BC) through the soil extending upward from the neutral plane at an angle  $\theta$  with the horizontal (see figure 26).

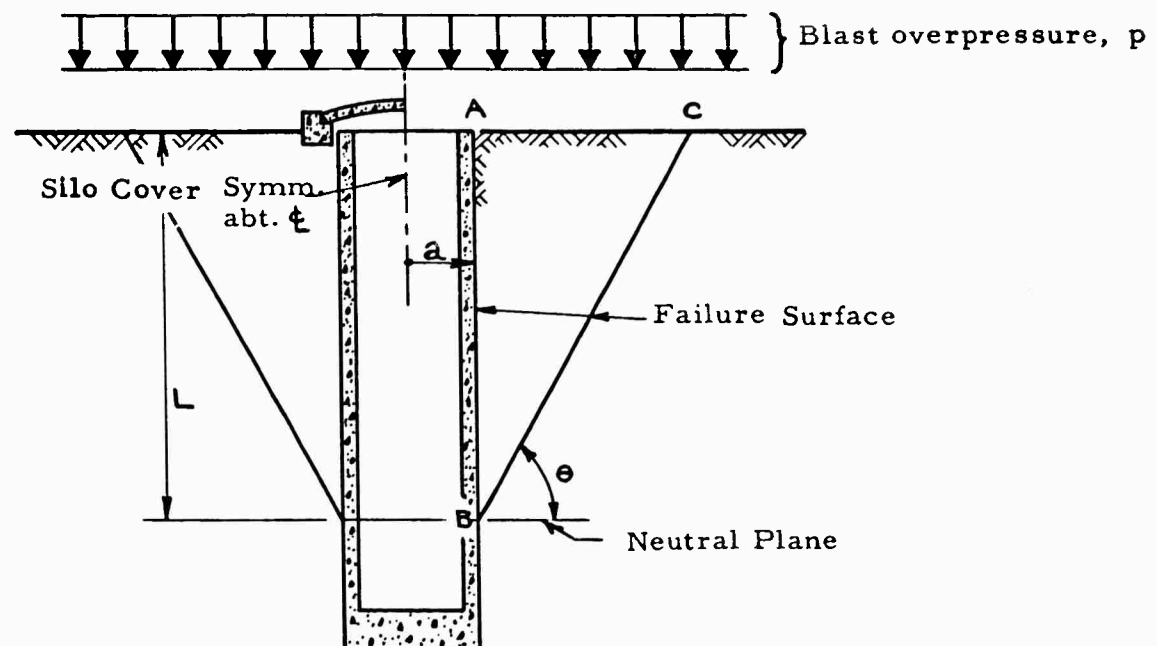


Fig. 26 SECTION THROUGH SILO SHOWING ASSUMED FAILURE SURFACE

The following assumptions are also made:

- 1) The soil outside the conical surface (BC) is in a state of impending downward motion relative to the soil inside the surface. The motion of the soil adjacent to the silo, above the neutral plane, is downward relative to the lining.
- 2) The full shearing strength of the soil is mobilized at the silo surface (AB) and the conical surface (BC) and is given by Coulomb's Law,

$$\tau = c + n \tan \phi \quad (74)$$

where

- $\tau$  is the unit shearing strength,
- $c$  is the unit "no-load" shearing strength or unit cohesion,
- $n$  is the applied normal stress at the failure surface, and
- $\phi$  is the angle of internal friction of the soil.

Consider an elemental wedge cut from the region of failure by vertical planes as shown in figure 27. The wedge is in equilibrium under the action of the following resultant forces.

- $W$  the weight of the soil wedge ABC
- $P$  the resultant of the surface pressures acting on the face AC
- $F_1$  the resultant of the friction stresses acting on BC
- $F_2$  the resultant of the friction stresses acting on AB
- $C_1$  the resultant of the cohesive stress on BC
- $C_2$  the resultant of the cohesive stress on AB
- $F_3$  the resultant of the circumferential stresses acting on the vertical surfaces of the wedge.

The surface pressure resultant for a silo with an independently supported cover is

$$P = \frac{p}{2} (a + L \cot \theta)^2 d\alpha \quad (75)$$





This equation assumes that the total surface pressure acting on the cross sectional area of the lining (elemental area OA, figure 27) is applied to the surface AC.

For a silo with monolithic cover,

$$P = \frac{pL \cot \theta}{2} (2a + L \cot \theta) d\alpha \quad (76)$$

The soil wedge weight is,

$$W = wL \cot \theta \left( a + \frac{L \cot^2 \theta}{3} \right) d\alpha, \quad (77)$$

where  $w = \rho L/2$  and  $\rho$  is soil density. The resultant cohesive forces are,

$$C_1 = \frac{cL}{\sin \theta} \left( a + \frac{L}{2} \cot \theta \right) d\alpha \quad (78)$$

and

$$C_2 = caL d\alpha \quad (79)$$

The friction forces  $F_1$  and  $F_2$  can be specified in terms of the unknown force  $F_3$ , through the conditions of vertical and horizontal equilibrium. If the ratios  $F_1/F_3$  and  $F_2/F_3$  are known, the angle  $\theta$  that minimizes  $F_2$  can be found.  $F_2$  obtained in this way is correct provided the failure surface is the proper one. The determination of  $F_3$  requires a detailed consideration of equilibrium throughout the wedge; however, an upper bound on the resultant  $F_2$  can be found by assuming  $F_3 = 0$ . For this case, the equations of equilibrium in the horizontal and vertical directions are

$$C_1 \cos \theta + F_1 \sin (\theta + \phi) - F_2 \cos \phi = 0 \quad (80)$$

$$P + W + C_1 \sin \theta - C_2 - F_1 \cos (\theta + \phi) - F_2 \sin \phi = 0. \quad (81)$$

Eliminating  $F_1$  from equations 80 and 81 and solving for  $F_2$  yields,

$$F_2 = \frac{P + W + C_1 [\sin \theta + \cos \theta \cot (\theta + \phi)] - C_2}{\sin \phi + \cos \phi \cot (\theta + \phi)} \quad (82)$$

The average shear stress attributed to friction at the silo-soil interface is

$$n \tan \phi = \frac{F_2 \sin \phi}{a L d \alpha} \quad (83)$$

Substituting equations 75, 77, 78 and 79 into the nondimensional form of this equation results in (independent cover case),

$$\begin{aligned} \frac{n \tan \phi}{p} = & \left\{ \left[ \frac{1}{2} \frac{L}{a} \left( \frac{a}{L} + \cot \theta \right)^2 + \frac{c}{p} \cot \theta \left\{ \cot (\theta + \phi) + \right. \right. \right. \\ & \left. \left. + \frac{L}{2a} \left[ 1 + \cot \theta \cot (\theta + \phi) \right] \right\} + \frac{w}{p} \cot \theta \left( 1 + \frac{L}{3a} \cot^2 \theta \right) \right] \times \\ & \left. (\tan \theta + \tan \phi) \sin \phi \cos \phi \right\} \quad (84) \end{aligned}$$

The correct angle ( $\theta$ ) is that which produces a minimum value for  $n \tan \phi/p$ . The angle is readily found as a root to the equation,

$$\frac{d \left( \frac{n \tan \phi}{p} \right)}{d \cot \theta} = 0.$$

Performing the indicated operation yields

$$\tan^3 \theta + A \tan \theta + B = 0 \quad (85)$$

where

$$A = -\frac{2L}{a} \left[ \frac{c}{p} + \frac{1}{2} \frac{L}{a} + \frac{1}{3} \frac{w}{p} \frac{L}{a} + \left( 1 + \frac{w}{p} \right) \tan \phi \right]$$

and

$$B = -2 \frac{L^2}{a^2} \left[ \frac{c}{p} + \left( 1 + \frac{2}{3} \frac{w}{p} \right) \tan \phi \right].$$

Considerable simplification is afforded by neglecting the second-order effect of  $\frac{w}{p}$ ; thus when  $\frac{w}{p} = 0$

$$\tan \theta = \frac{L}{2a} \left[ 1 + \sqrt{1 + 8 \frac{a}{L} \left( \frac{c}{p} + \tan \phi \right)} \right]. \quad (86)$$

The resulting ratio of average shear stress at the silo interface to the surface overpressure,  $\tau/p$ , for the independent cover case is

$$\frac{\tau}{p} = \frac{c}{p} + \frac{n \tan \phi}{p}, \text{ Independent Cover} \quad (87)$$

where the second term in the right hand member is given by equation 84 with minor error involved when  $\theta$  from equation 86 is used. Curves  $\tau/p$  versus  $a/L$  are plotted in figure 28 for various values of  $\phi$  when  $w/p = c/p = 0$  for the independent cover case.

Substituting equations 76 through 79 into equation 83 yields, for the monolithic cover case,

$$\begin{aligned} \frac{n \tan \phi}{p} = \frac{1}{2} & \left[ \cot \theta \left( 1 + \frac{L}{2a} \cot \theta \right) + \frac{c}{p} \cot \theta \right. \\ & \left. \left\{ \cot (\theta + \phi) - \frac{L}{2a} \left[ 1 + \cot \theta \cot (\theta + \phi) \right] \right\} + \right. \\ & \left. + \frac{w}{p} \cot \theta \left( 1 + \frac{L}{3a} \cot^2 \theta \right) \right] (\tan \theta + \tan \phi) \sin \phi \cos \phi. \end{aligned} \quad (88)$$

Here, it makes no sense to seek the minimum value of equation 88 since the smallest realistic value of  $n \tan \phi/p$  occurs when  $\theta=90$  deg. For this angle, the failure zone can be thought of as a thin wedge with an infinitesimal opening angle, in which case, L' Hospital's rule is applied to the indeterminate  $0/0$  form of equation 88. The resulting ratio of average shear stress at the silo interface to the surface pressure for the monolithic cover case is

$$\frac{\tau}{p} = \frac{c}{p} + \frac{1}{2} \left[ 1 + \frac{w}{p} + \frac{c}{p} \left( \frac{L}{2a} - \tan \phi \right) \right] \sin 2 \phi, \quad (89)$$

Monolithic Cover.

### C. Silo Model Push-Out Tests

To determine the usefulness of the upper-bound skin friction theory given in the previous section, push-out tests have been conducted with a small silo model embedded in sand for comparison of measured values to those given by equations 87 and 89. Relative motion for these experiments similar to that described in the analysis, i. e., downward motion of the soil adjacent to the

ARMOUR RESEARCH FOUNDATION OF ILLINOIS INSTITUTE OF TECHNOLOGY

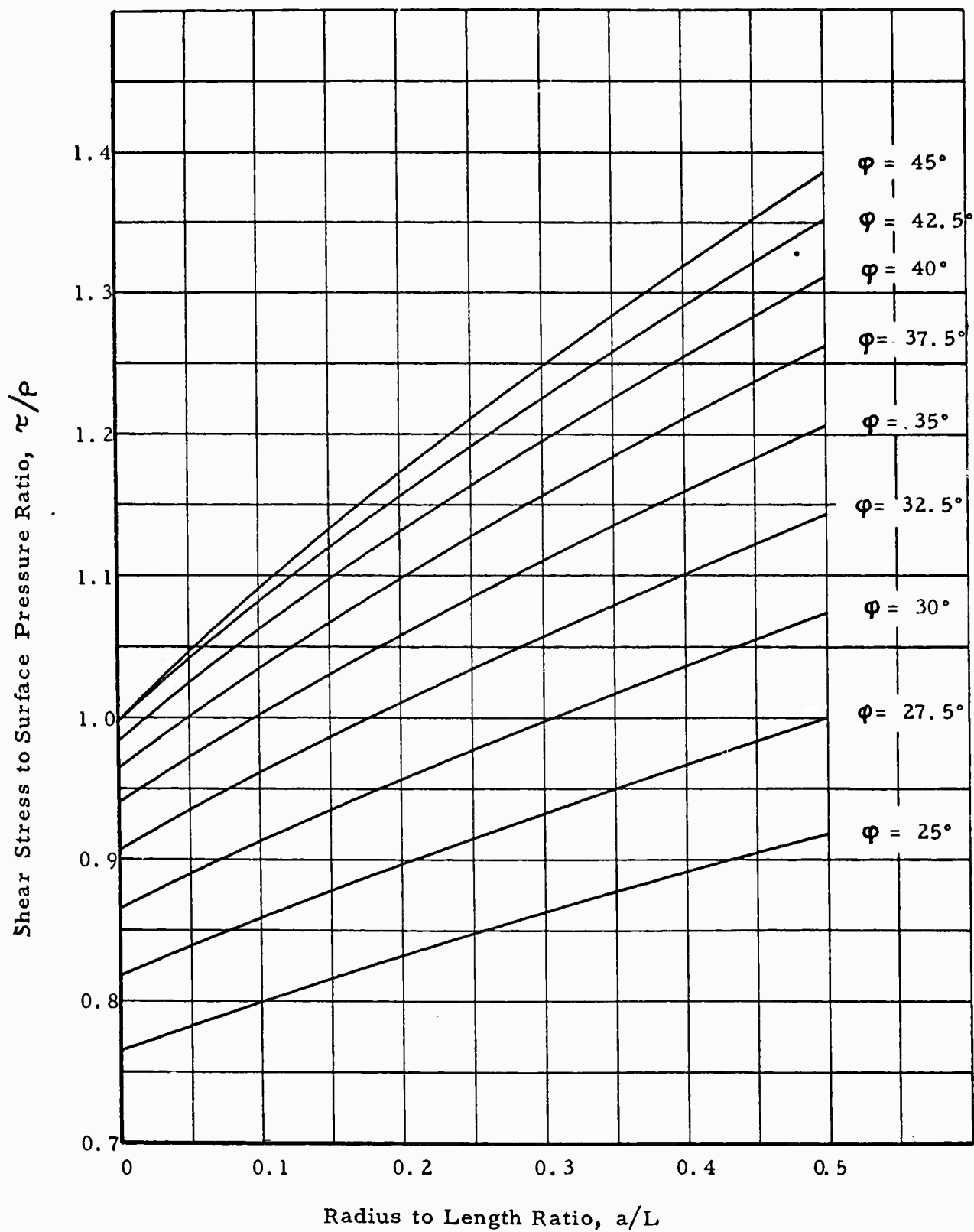


Fig. 28 INDEPENDENT COVER SILO SHEAR STRESS FOR  $w = c = 0$

lining, has been obtained by forcing the silo model up through the sand with a hydraulic jack. Eight tests were performed, two with an independent cover and six with monolithic or integral cover. Both loose and dense sand conditions were used and surface pressures from zero to 20 psi were applied prior to application of the silo model displacement load. A sketch of the test arrangement is shown in figure 29.

The tests were performed in the 3-ft diameter, 3-ft high containment vessel that was used for the tunnel model tests (section III B). The silo model was 2-ft long, 6-in. in diameter and weighed 45 lb. A 9-in. diameter cover was placed over the top of the model in two of the tests to simulate an independently supported cover. A small clearance was provided between the cover and silo model to permit relative motion between the two. The remainder of the tests were performed without the independent cover to simulate a silo with a monolithic cover the same diameter as the silo. Twenty V-grooves per inch (1/32-in. deep) were cut in the outside face of the silo model normal to the silo axis to assure a value of  $\phi$  equal to that of sand-on-sand at all failure surfaces. Direct shear tests confirm that  $\phi$  for the grooved surface is higher than the sand-on-sand value; consequently, failure occurs on a cylindrical surface, at the silo model wall, that has a radius slightly larger than the model radius.

Dry Ottawa sand with a grain-size distribution shown in figure 16 was used for all tests. Loose sand with average density ranging from 99 to 100.5 pcf were used for half the tests. The loose-sand condition was obtained by slowly pouring the sand in the pressure vessel with a hand-scoop in a uniform manner. Free-fall during placement was limited to less than 1 inch. Dense sand was obtained by penetration of a one-horsepower, 10,000 rpm concrete vibrator probe the depth of the sand-filled pressure vessel at several positions around the model. Average dense sand densities varied from 107.7 to 111.0 pcf. The relationship between the angle of internal friction and the sand density, given in figure 30 was determined from triaxial test data for confining pressures of 10 and 15 psi.

Table 7 gives the model arrangement, surface pressure, soil properties and the test results for the eight tests. Load-displacement curves

ARMOUR RESEARCH FOUNDATION OF ILLINOIS INSTITUTE OF TECHNOLOGY

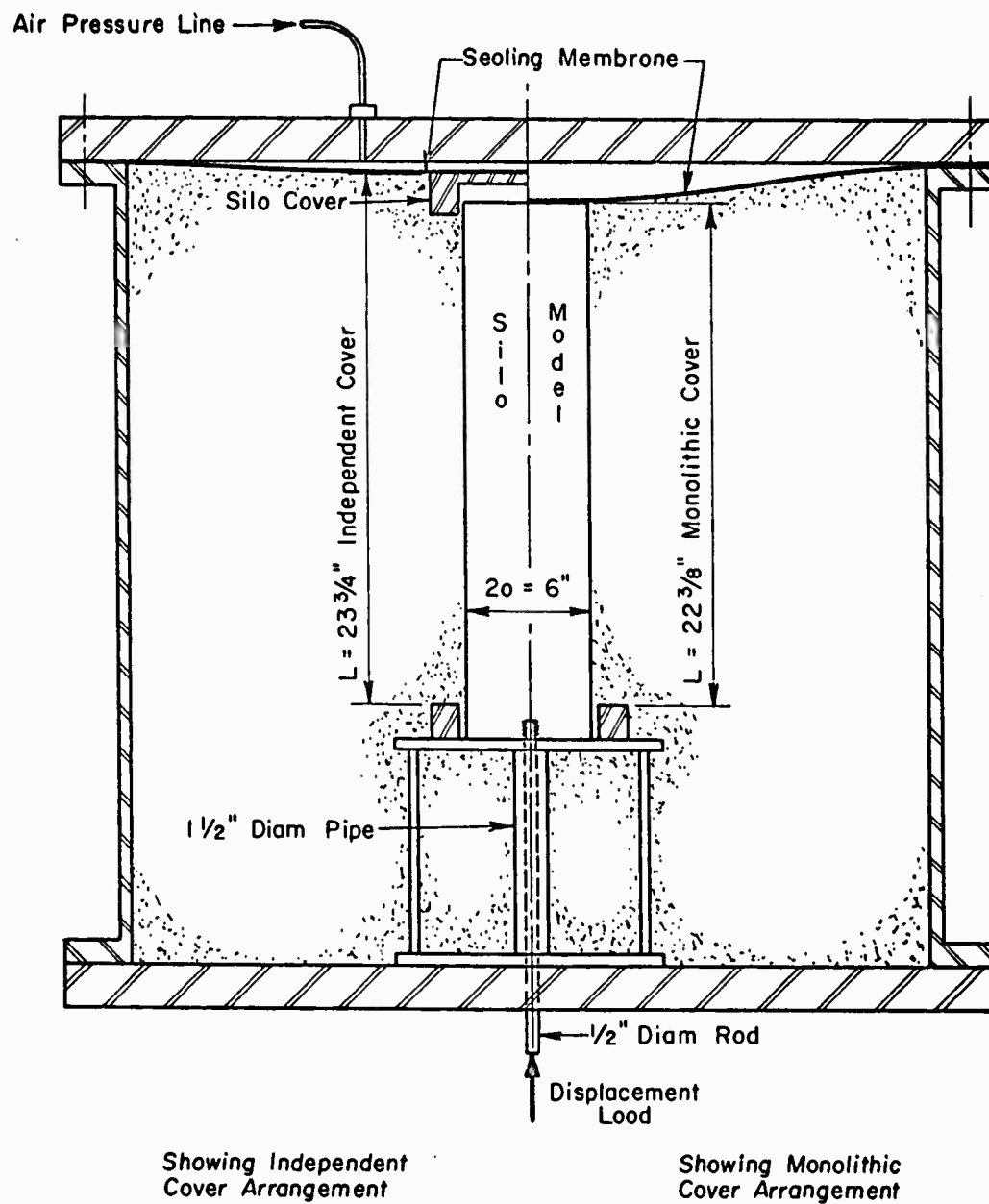


Fig. 29 SILO MODEL PUSH-OUT TEST ARRANGEMENT

Table 7  
SILO MODEL PUSH-OUT TESTS

Test No.	Silo Model Arrangement	Average Sand Density (pcf)	$\phi$ (deg)	Surface Pressure (psi)	Max Shear Load (lb)	Apparent c/p	$\tau / p$	
							Measured	Theory
1	Independent Cover	100.5 (loose)*	30.0	10	1205	0.027	0.267	1.026
2	Independent Cover	110.3 (dense)	36.5	7.5	4305	0.220	1.29	1.666
3	Monolithic Cover	99.6 (loose)	29.7	10	940	0.014	0.23	0.491
4	Monolithic Cover	111.0 (dense)	37.5	5	3535	0.354	1.68	1.412
5	Monolithic Cover	100 (loose)	30.0	20	1840	0.010	0.22	0.470
6	Monolithic Cover	108.9 (dense)	35.5	5	3225	0.292	1.53	1.247
7	Monolithic Cover	99 (loose)	29.5	0	125	Apparent c = .055 psi		
8	Monolithic Cover	107.7 (dense)	34.5	0	625	" 1.31 psi		

\* Loose, dense refers to placement technique (see text).



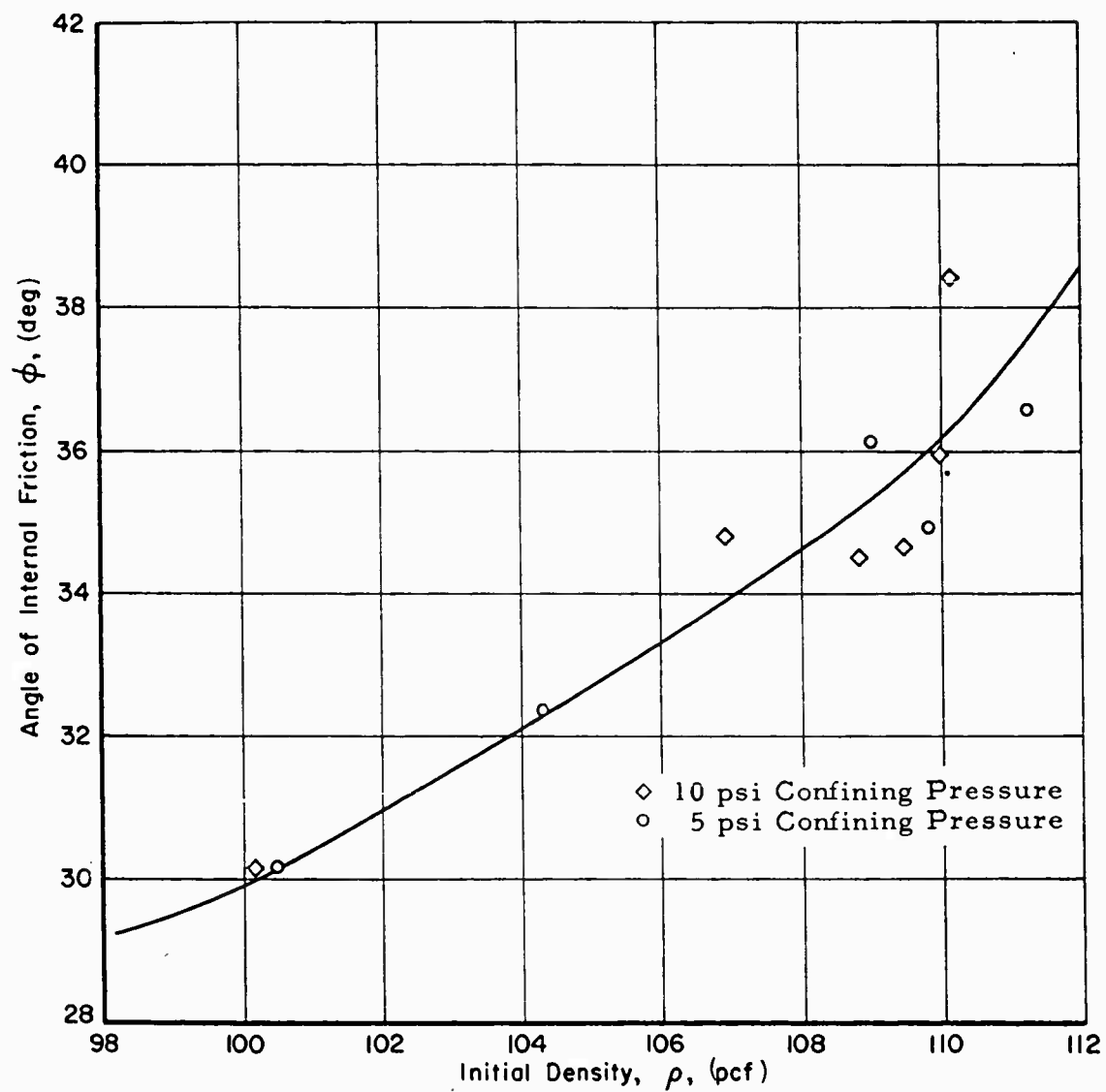


Fig. 30 ANGLE OF INTERNAL FRICTION VERSUS DENSITY,  
OTTAWA SAND

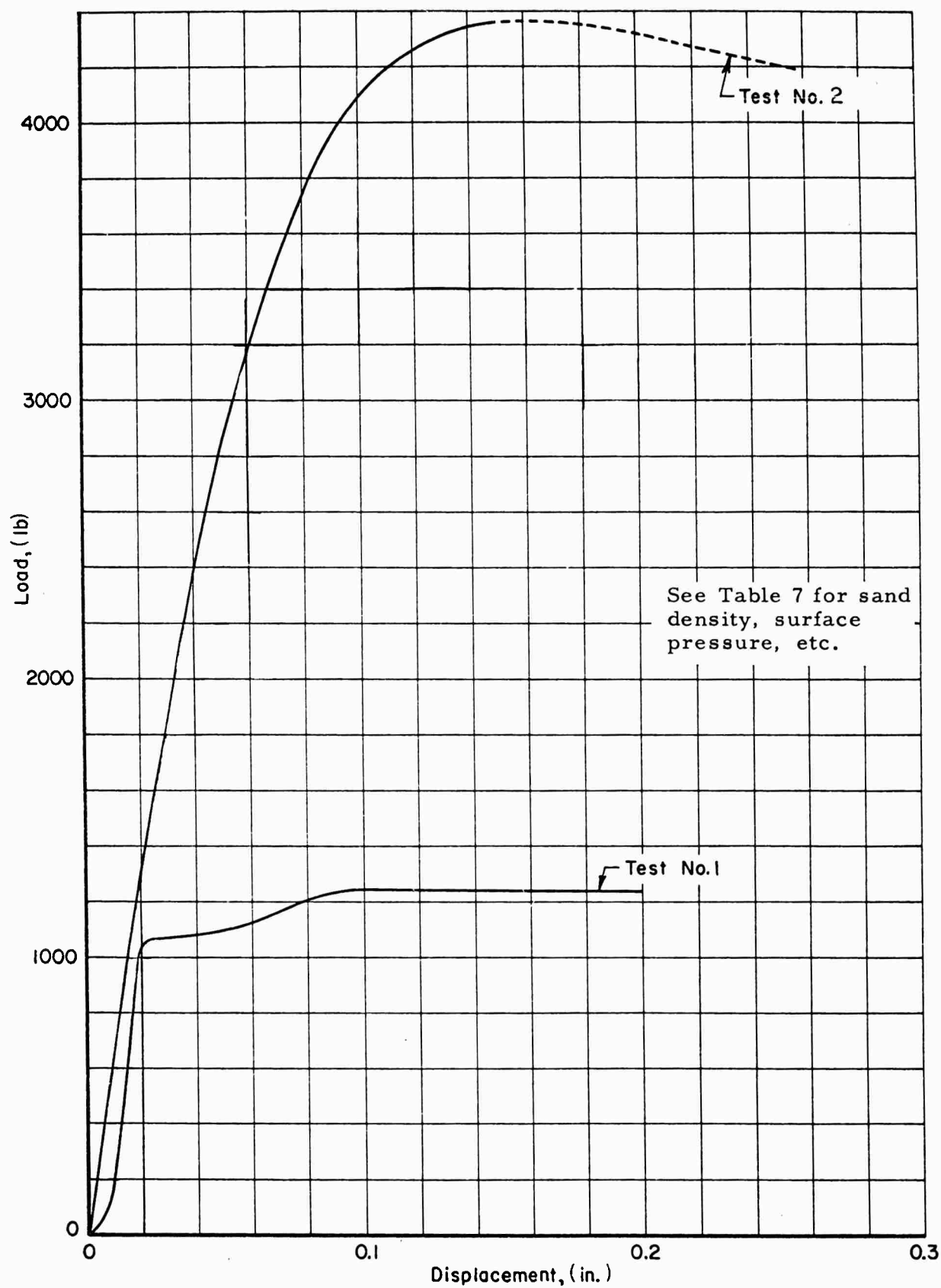


Fig. 31a LOAD DISPLACEMENT CURVES FOR SILO MODEL  
PUSH-OUT TESTS, INDEPENDENT COVER

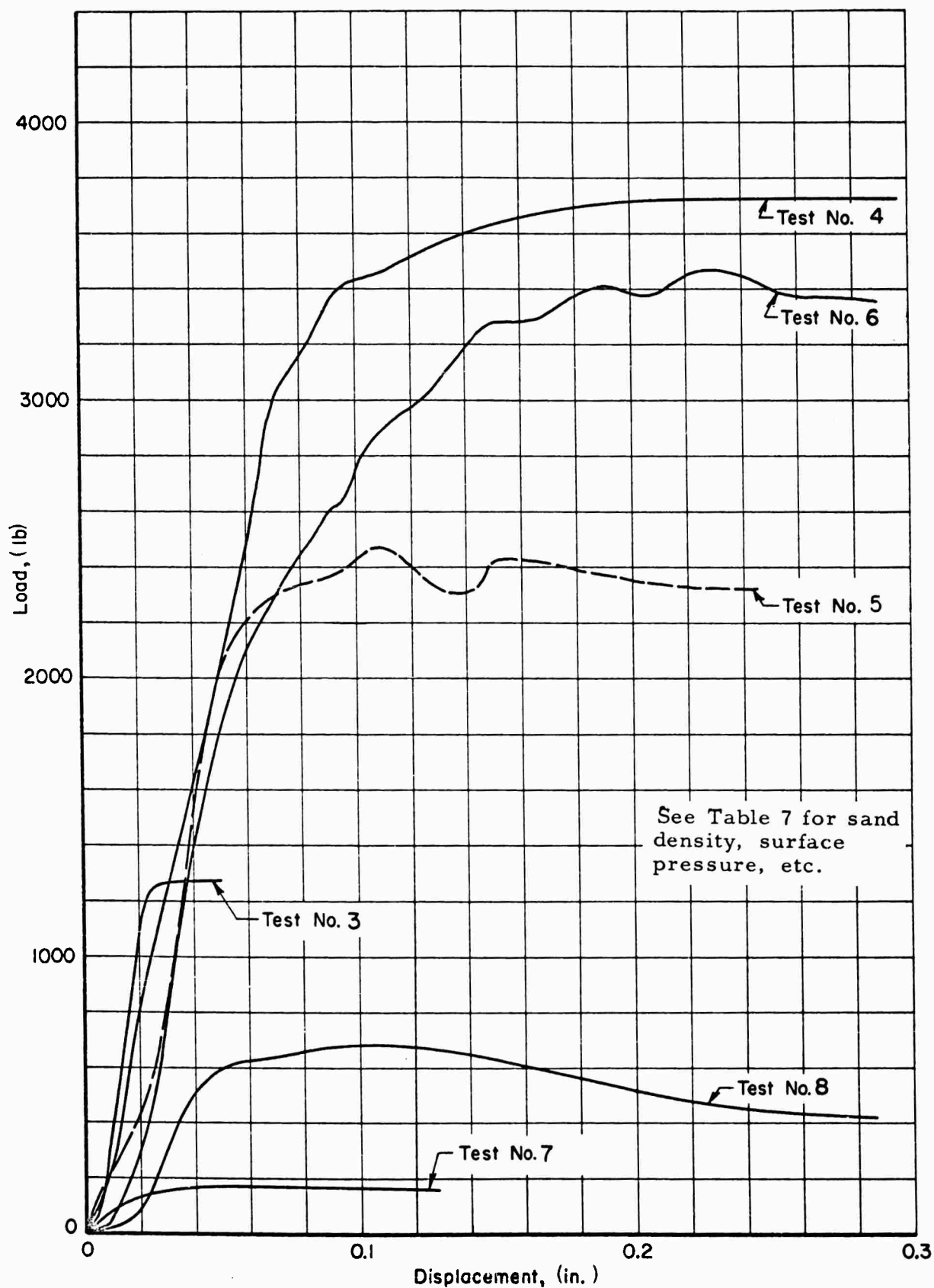


Fig. 31b LOAD-DISPLACEMENT CURVES FOR SILO MODEL  
PUSH-OUT TESTS, MONOLITHIC MODEL

for each test are given in figures 31a and 31b. Tests 7 and 8 (monolithic cover tests) were run with no surface pressure to obtain a value for the "no-load" shearing strength or the apparent cohesion ( $c$ ) at the silo model surface. The apparent cohesion was found according to the assumption that the surface shear  $\tau$  given by the theory (Eq. 89) accurately represents the measured average shear value. Thus, by taking

$$\tau_{\text{theory}} = \tau_{\text{measured}}$$

it is possible to compute the value of  $c$  since  $p$ ,  $w$ ,  $a/L$  and  $\phi$  are known. The result is:  $c = .055$  psi, Test 7 (Loose Sand,  $\rho = 99$  pcf); and  $c = 1.31$  psi, Test 8 (Dense Sand,  $\rho = 107.7$  pcf).

This apparent cohesion is fictitious in that it is actually caused by intergranular pressures created during soil placement. These intergranular pressures generate initial normal soil stress at the failure surfaces over and above the normal stress determined from equilibrium considerations. The initial normal stresses impart a "no-load" shearing resistance property that is assumed to be identical to that created by cohesion. The apparent cohesive stresses found from Tests 7 and 8 are used to obtain  $c/p$  ratios for tests 1 through 6 by assuming a linear relationship between  $c$  and the sand density. The value of  $c/p$  obtained in this manner is given in table 7 for each test.

Maximum measured shear loads at the silo model interface and average theoretical and measured shear stress-to-surface pressure ratios ( $\tau/p$ ) are also given in the table. The maximum shear loads were found by subtracting the silo model weight from the maximum jack load for the independent cover tests and subtracting the model weight and surface pressure ( $p$ ) acting on the silo model for the monolithic cover tests.

Measured and theoretical  $\tau/p$  values for the loose sand tests compare very poorly. The wide discrepancy is probably caused by the small void ratio reduction resulting from grain redistribution in the vicinity of the silo model wall which relieves part of the normal pressure at the silo model surface. It is concluded that the analysis is not applicable to soils that

ARMOUR RESEARCH FOUNDATION OF ILLINOIS INSTITUTE OF TECHNOLOGY

experience void ratio reductions during shear (e.g., loose sand). It is interesting to note that an average normal pressure ( $n$ ) on the model surface of  $1/3$  the surface overpressure ( $p$ ) results in  $\tau/p$  values of approximately 0.21 which compares favorably with the measured ratios for the loose sand tests.

For the dense sand tests, the  $\tau/p$  values given by the theory compare fairly well with the measured values. However, for the monolithic cover dense sand tests (Tests 4 and 6), the measured  $\tau/p$  ratio is approximately 20 percent higher than the value obtained from the theory. Thus, for these tests, the theory did not yield an upper-bound value. This indicates that the assumed conical failure surface through the soil is incorrect.

#### D. Segmented Silo Model Tests

These tests simulate a more realistic silo model environment than the push-out tests described in the previous section. For these experiments, shear loads developed at the silo model surface are generated by relative motion between the structure and soil. This relative motion is created by soil compression. The silo model was embedded in dense Ottawa sand contained in the Foundation Dynamic Soil Facility. The test arrangement is shown schematically in figures 32a and 32b for the independent and monolithic cover tests. Two tests were run, one with and one without the independently supported cover. Surface pressure up to 285 psi was employed.

To accentuate the silo skin friction forces (generated by the relative displacement at the silo-soil interface) the segmented silo model has been made as rigid as possible in the longitudinal direction acknowledging that the silo segment loads must be measurable even for small friction forces. The cantilever-Maypole arrangement for the segmented silo shown in figure 33 was used for these tests. The segmented silo model consists of four, equal, 6-in. diameter cylindrical segments 6-in. long, each independently pin connected to three cantilever arms radiating from a  $3/4$ -in. diameter center pole that is supported at the silo model base plate (see figure 33 and 34). A  $3/32$ -in. clearance was provided between each segment and at the base and cover. The cylinder segments were fabricated from  $3/16$ -in. wall steel tubing, and 20 V-grooves per inch,  $1/32$ -in. deep were cut in the outside surfaces to assure a

ARMOUR RESEARCH FOUNDATION OF ILLINOIS INSTITUTE OF TECHNOLOGY

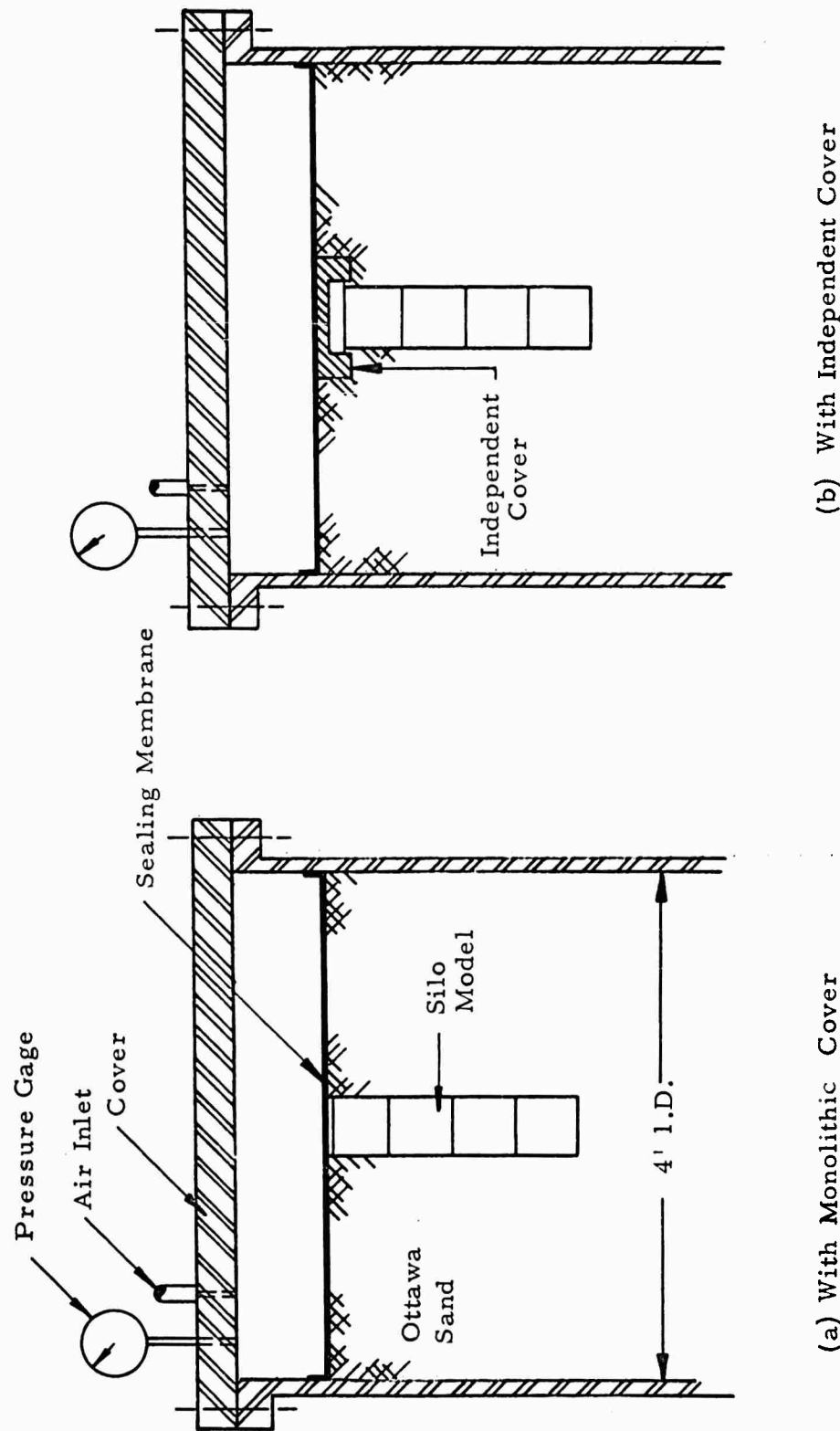


Fig. 32 SEGMENTED SILO MODEL TEST ARRANGEMENT

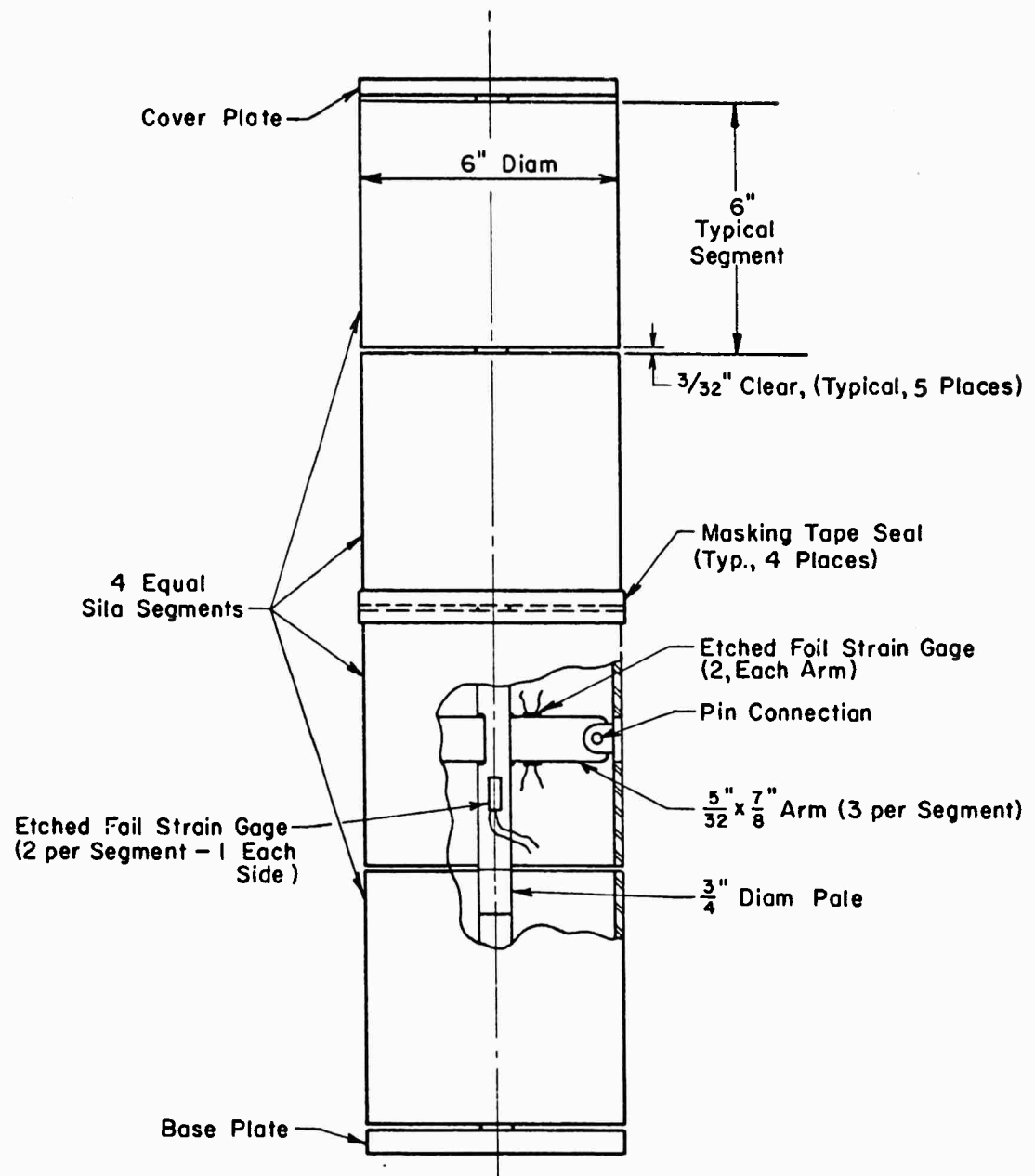


Fig. 33 SEGMENTED SILO MODEL

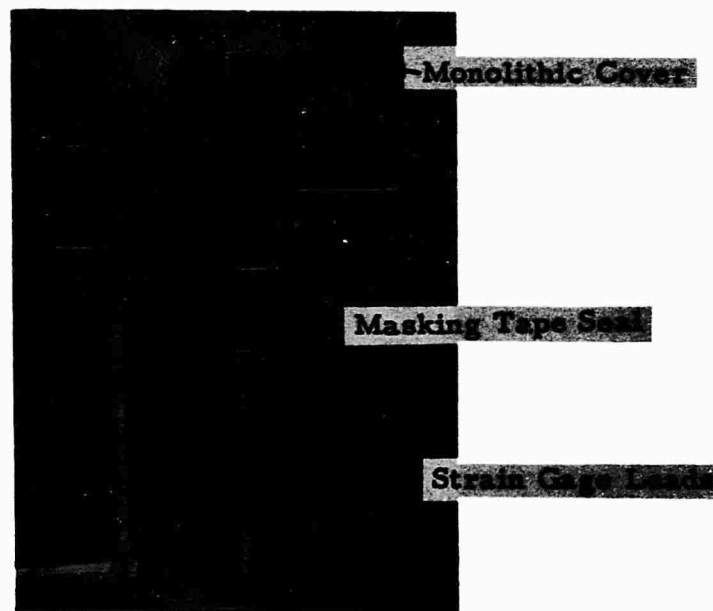


Fig. 34 SEGMENTED SILO MODEL



silo-soil interface angle of internal friction equal to the sand-on-sand value. An assembled and exploded view of a typical segment is shown in figure 35.

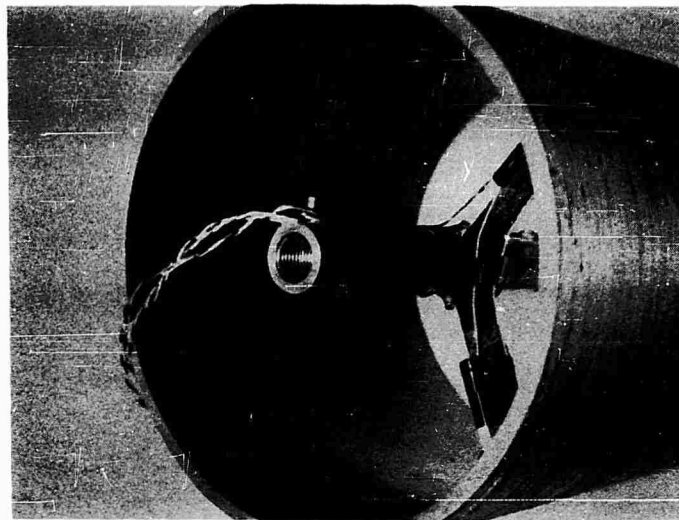
Silo lining model shear resultants of each silo segment were determined from strain measurements made with Budd etched-foil gages, type C6-121 and C6-141-B. The location of the gages is shown in figure 33. The C6-121 gages are located on the silo segment support arms near the center pole in order to register the highest arm strain. These gages are mounted in pairs on each arm, one gage each on the upper and lower surfaces. The C6-141-B gages are mounted in pairs on opposite sides of the 3/4-in. diameter center pole below the silo segment support arms. These gages register the sum of the segment loads and serve as a check on the individual segment loads obtained from the arms. The output of each pair was averaged to eliminate the effects of local bending of the pole. The 9-in. diameter independent silo cover was the same as used for the push-out tests.

The silo cover and sand surface vertical displacements were measured during the surface pressurization by two LVDT's, one at the center of the cover and one 10-inches from the pressure vessel wall. Figure 36 shows the two LVDTs in place with pressure vessel head removed. The ARF Dynamic Soil Facility, shown in figure 36, consists of a pressure vessel fabricated from a 4-ft ID by 4-ft cylinder with a fixed dished head on the bottom and a removable flat head on top. Design was based on 300-psi internal pressure. The Ottawa sand used for the tests was the same as used for the silo push-out tests. The average sand density of 108.9 pcf, for both tests, was obtained by penetration of a one-horsepower, 10,000 rpm concrete vibrator probe in a symmetrical manner around the silo model.

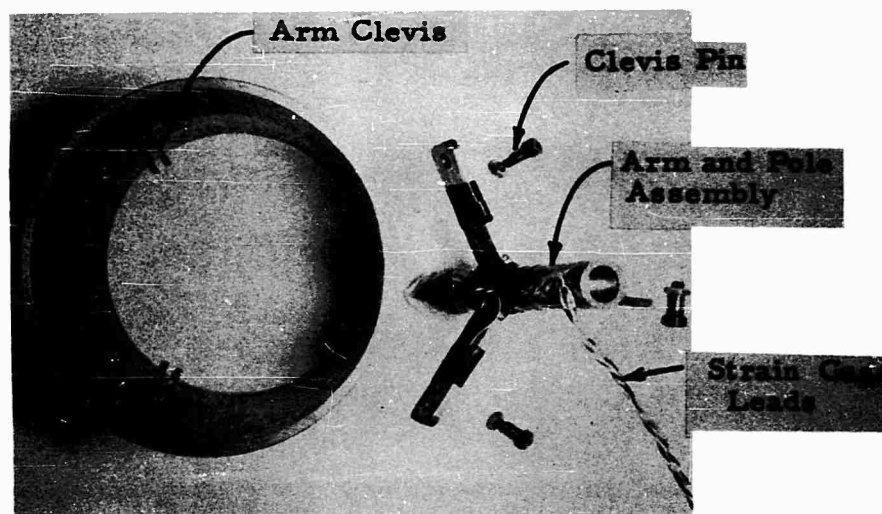
Surface pressure versus displacement curves for the sand surface 10-in. from the pressure vessel wall (14-in. from the center of the model) and the silo cover are given in figure 37 for both tests. Curves of pressure versus shear load for each of the four segments are given in figures 38a and 38b. These shear loads were obtained from segment arm strain measurements.

It is observed in figures 38a and 38b that the shear loads are much smaller than predicted from the upper-bound analysis (given in section V B)

ARMOUR RESEARCH FOUNDATION OF ILLINOIS INSTITUTE OF TECHNOLOGY



a. ASSEMBLED VIEW



b. EXPLODED VIEW

Fig. 35 TYPICAL SILO MODEL SEGMENT

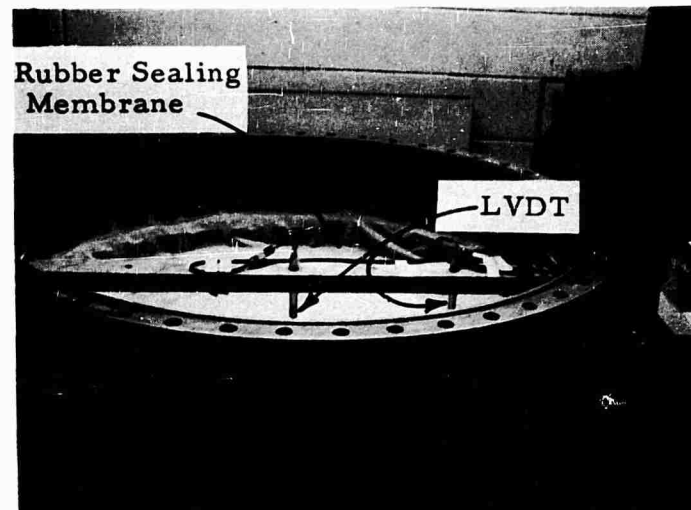


Fig. 36a SEALING MEMBRANE AND LVDT ARRANGEMENT

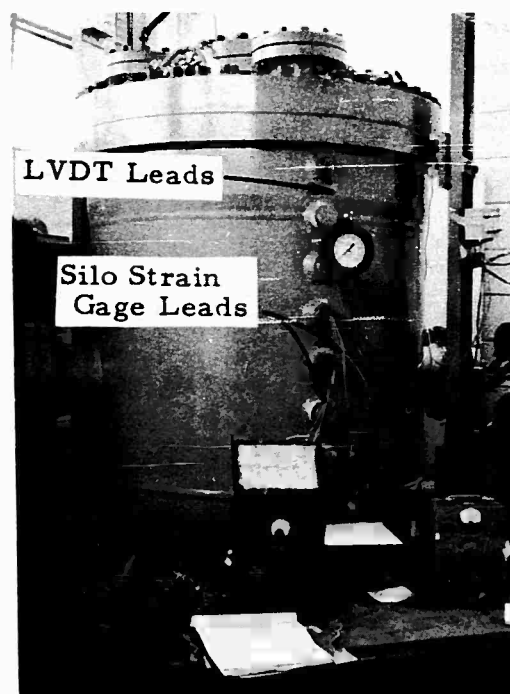


Fig. 36b ARF DYNAMIC SOIL FACILITY

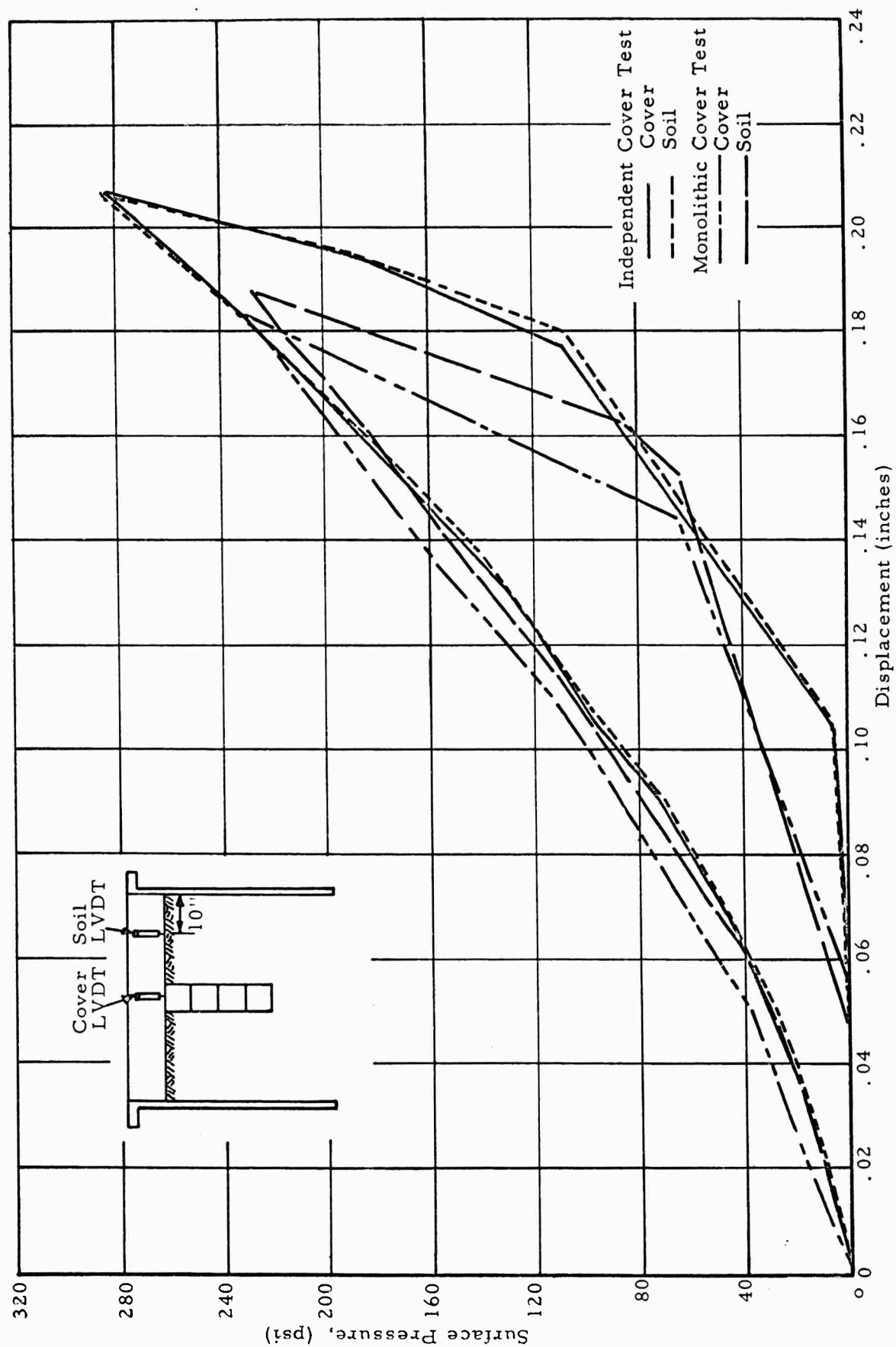


Fig. 37 SURFACE PRESSURE VERSUS SILO COVER AND SOIL DISPLACEMENT

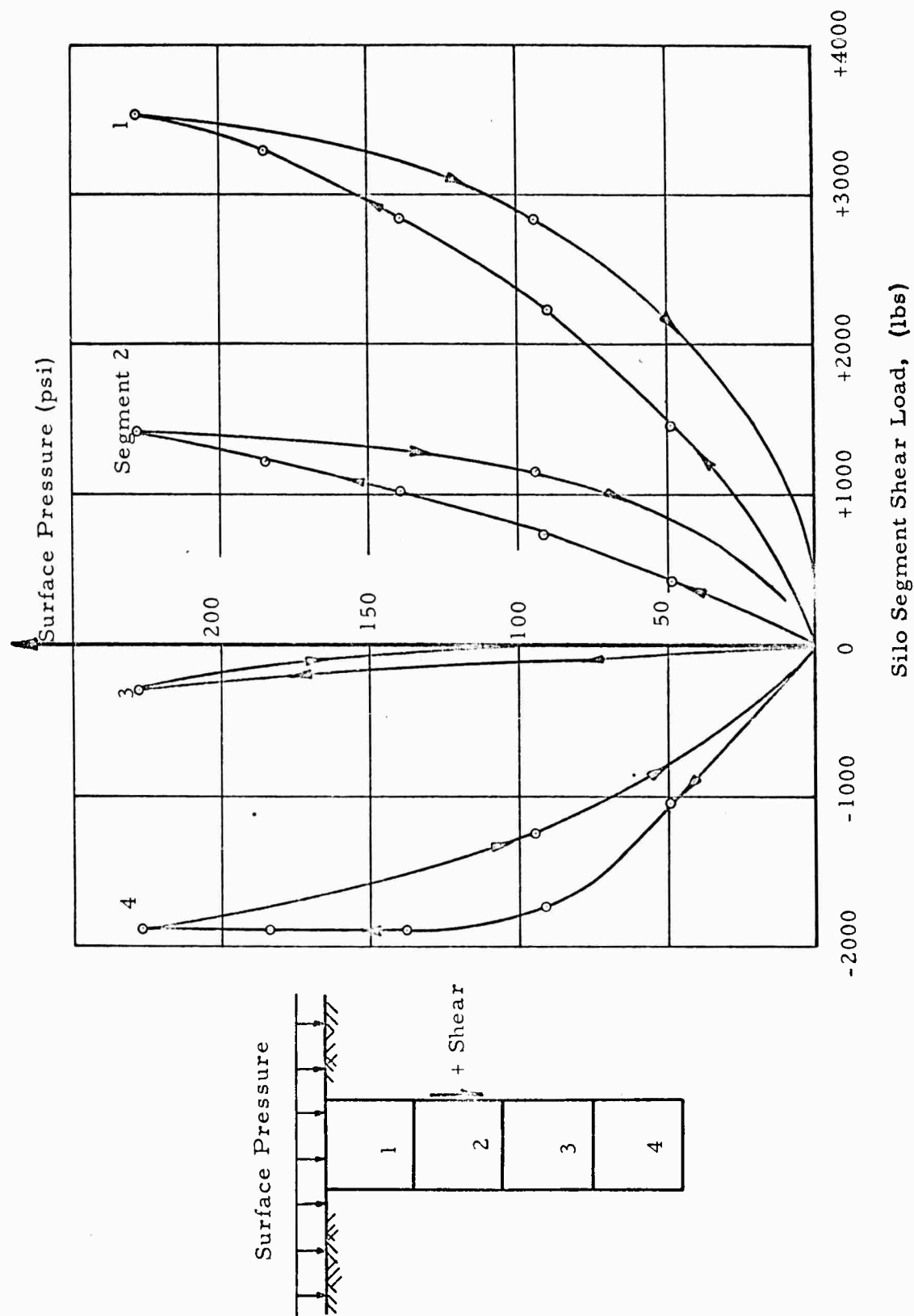


Fig. 38a PRESSURE VERSUS SEGMENT SHEAR, SILO WITH MONOLITHIC COVER

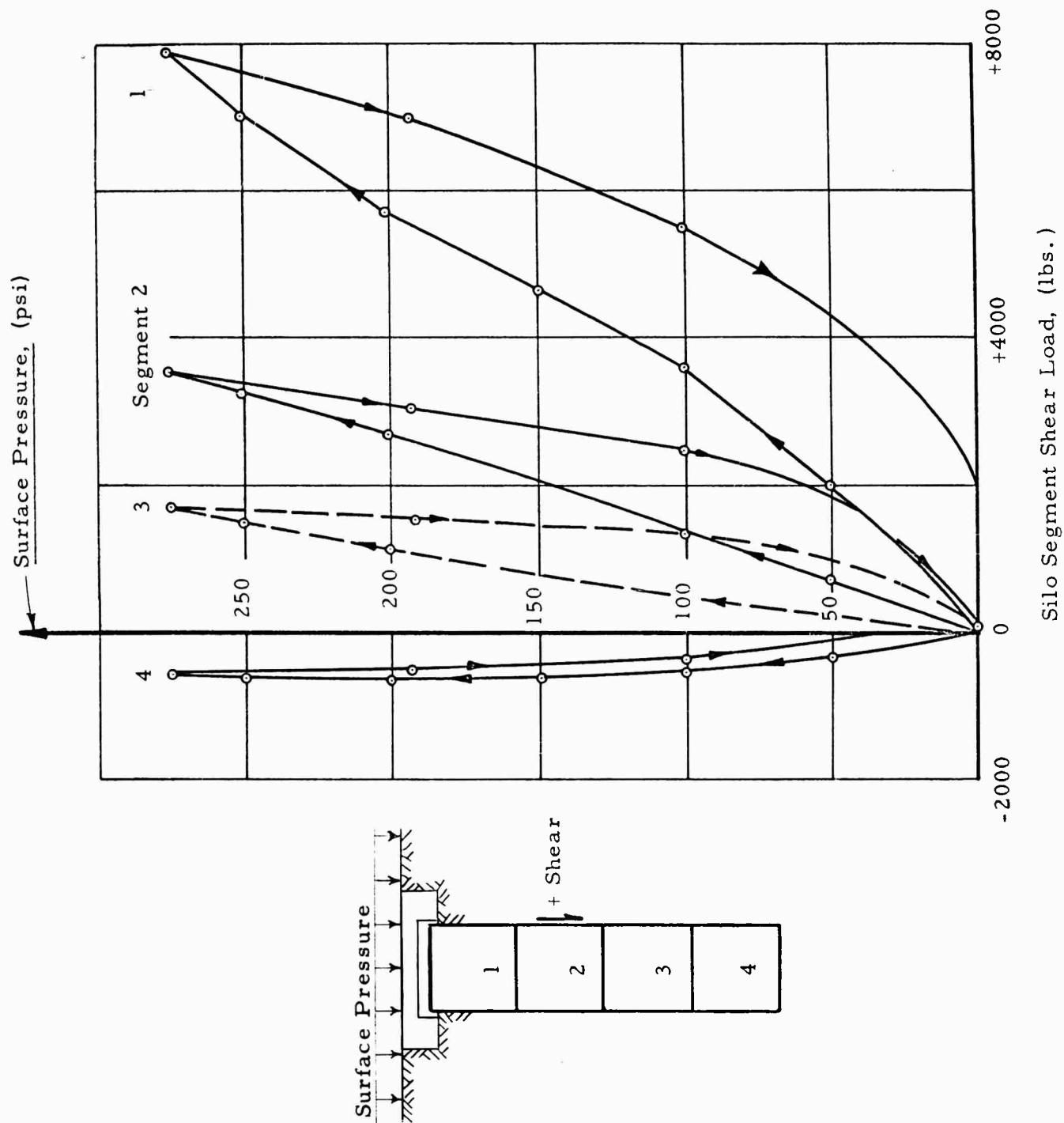


Fig. 38b SURFACE PRESSURE VERSUS SEGMENT SHEAR, INDEPENDENT COVER

since the relative motion of the soil with respect to the silo is quite small. This is apparent from the monolithic cover curves in figure 37; that is, the soil and cover displacements are nearly identical whereas the soil strain must exceed the model strain to obtain the necessary relative motion (see figure 24). Unfortunately, the soil strains were even less than anticipated. The surface displacements, which are a measure of the soil strains, were considerably smaller for these tests than for the tunnel model tests (Fig. 18). The untreated wall (no Teflon lining) of the ARF dynamic pressure vessel is probably the primary cause of the nearly trivial soil strains. The conclusion is that the silo is more flexible than the soil; consequently, the silo strains match the soil strains. Future tests with the segmented silo model in the manner described here should obviously be accompanied by more flexible soil and containment vessel wall treatment to reduce the shear generated at the soil boundary to a minimum.

## SYMBOL INDEX

### Section V

a	shell radius
c	cohesive stress
$C_1, C_2$	elemental soil cohesive forces
$F_1, F_2$	elemental soil friction forces
$F_3$	elemental circumferential soil force resultant
L	silo length above neutral plane
n	normal stress
p	surface overpressure
P	elemental overpressure force
w	$= \rho L/2$
W	elemental soil wedge weight
$\theta$	failure angle through soil medium
$\rho$	soil density
$\tau$	shear stress
$\phi$	angle of internal friction



## VI. CONCLUSIONS AND RECOMMENDATIONS

The analysis of the response of a cylindrical shell to a plane wave has progressed to the point where the characteristics of the predicted response appear to be in excellent qualitative agreement with the meager experimental evidence available (e. g. NTS tests on buried conduits). The results obtained with a step pulse loading indicate that the maximum stresses and displacements may be significantly lower for a decaying stress pulse. This conclusion follows from the fact that the maximum dynamic response values occur in the neighborhood of five or six transit times. Thus, it is necessary to investigate effects of a decaying pressure pulse to obtain realistic results for full scale structures. It is felt that a logical and important continuation of this phase of the theoretical investigation should be concerned with the following additions or modifications to the existing method of analysis:

1. A refined stress wave with a linear rise to a peak stress and then an exponential or linear decay (depending on the complexity of the Fourier series representation) to a constant stress level.
2. A nonlinear foundation modulus.
3. Tangential surface shears proportional to the normal pressure.

In view of the fact that these features are associated with real soil behavior the possibility of including these items should be thoroughly investigated.

The ultimate objective of the experimental investigations on buried cylindrical shells is to verify the ability of the method of analysis to predict shell stresses and displacements. The static testing of tunnel models represents an initial step toward this objective. Unfortunately the test results suffer from the current lack of satisfactory soil stress and strain measurement devices. Furthermore, the measurement of applied surface pressure and related surface deflections are insufficient (for the pressure vessel used for these tests) to accurately determine the required free-field stress and strain at the tunnel model instrumentation section. The limited experimental results of Section III appear to substantiate the static theory given in Section II. Two hypotheses are required to reach this conclusion; namely, that 1) the ratio of vertical

ARMOUR RESEARCH FOUNDATION OF ILLINOIS INSTITUTE OF TECHNOLOGY

free-field pressure to surface pressure decreases, and 2) the ratio of free-field strain to average strain (based on the surface displacements) increases with increasing containment vessel wall friction. It is recommended that these tests be continued as soon as suitable soil pressure and strain gages are available.

The reported theoretical investigation of longitudinal bending of silo linings from differential horizontal displacements of the free-field relates only to static behavior. That is, expressions are presented to determine lining pressures, shears and bending moments in terms of a given free-field displacement profile and foundation modulus. The elastic stresses produced from this effect are shown to be significant for the reinforced concrete silo lining studied. This investigation should be expanded to investigate the dynamic effects of this loading source.

For such an analysis it would be necessary to obtain a time dependent free-field displacement function which varies with depth. The final horizontal displacements could be made to conform closely to those specified in the design criteria for current ICBM facilities. It is anticipated that the horizontal displacements generated from Rayleigh waves would be useful in specifying the displacements. Two structure-soil interaction restoring forces should be considered, one proportional to the relative displacement and the other proportional to the relative velocity. Virtual mass effects should also be included in the analysis. The static solution results indicate that the bending rigidity of silos is so great that only deflections due to shear need be taken into account. This suggests the use of a simplified structural model for the investigation of dynamic effects.

The exploratory series of tests performed, to investigate the problem of longitudinal silo friction, generated by relative vertical motion between the silo and the soil indicate the need for a more detailed analysis along the following lines. As a first approximation to the analysis, the zones above and below the neutral plane can be considered separately. Below the neutral plane, near the base of the silo, the state of stress is similar to that of a deep circular footing, for which the shear pattern and corresponding stresses are already known (13). Above the neutral plane,

ARMOUR RESEARCH FOUNDATION OF ILLINOIS INSTITUTE OF TECHNOLOGY

solutions can be obtained for the plastic stress distribution in this axisymmetric problem, which is analogous to the familiar two-dimensional earth pressure theories. Similar solutions have been developed (14) previously which should now be extended for this problem. These solutions can be superimposed to yield a combined solution for the silo problem. This first approximation can be improved by considering the interaction of these solutions to satisfy continuity conditions required in the actual problem.

Silo model push-out tests should be continued employing models with various length-to-radius ratios and alternate soils in addition to Ottawa sand. Tests with dynamically applied surface pressure should also be conducted employing a segmented silo model with higher axial rigidity.

The technique presented for the analysis of the stress-wave transmission and spallation problem in a silo resulting from surface air-blast loading indicates that severe tensile forces do not develop under loading of sufficiently long duration compared to the transit time of the stress wave down the silo length. Further investigation should be directed toward establishing the load parameters under which spallation damage does occur.

## REFERENCES

1. Newmark, W. M. and Hall, W. J., Preliminary Design Methods for Underground Protective Structures, AFSWC-TR-60-5, University of Illinois, Urbana, Ill., December 1959.
2. Salmon, M. A., Investigation of Silo Linings, Final Report, Contract AF29(601)-1168 for AFSWC, Kirtland AFB, New Mexico, Armour Research Foundation, Chicago, Illinois, September 1959. Confidential.
3. Watkins, R. K. and Spangler, M. G., "Some Characteristics of the Modulus of Passive Resistance of Soil: A Study of Similtude", Highway Research Board Proceedings, 37 (1958).
4. Watkins, R. K., "Influence of Soil Characteristics on Deformation of Embedded Flexible Pipe Culverts", Highway Research Board Bulletin 223 (1959).
5. Timoshenko, S., Theory of Elastic Stability, McGraw-Hill Book Co., Inc., (1936).
6. Bleich, H. H. and DiMaggio, F. L., "Dynamic Buckling of Submerged Plates and Shells", Columbia University Publication, Dept. of Civil Engineering Mechanics, Office of Naval Research Contract NONR-266(08). Technical Report No. 12 September, 1954.
7. Salmon, M. A., Investigation of Silo Linings, Interim Report, Contract No. AF29(601)-2596 for AFSWC, Kirtland AFB, New Mexico Armour Research Foundation, Chicago, Illinois, October 1960, Confidential.
8. Wiedermann, A. H., The Investigation of a Concept for Medium-Structure Interaction, Contract AF29(601)-2652 for AFSWC, Kirtland AFB, New Mexico, Armour Research Foundation, Chicago, Illinois, April 1961.

ARMOUR RESEARCH FOUNDATION OF ILLINOIS INSTITUTE OF TECHNOLOGY

9. Anderson, D. C. and Ashby, A., Development and Evaluation of Instrument Techniques to Measure Structural Effects in Nuclear Weapons Effects Simulation, Contract AF 33(616)-7098, ASD Technical Report 61-24, Wright-Patterson AFB, Ohio, Armour Research Foundation, Chicago, Illinois, April 1961.
10. Haywood, J. H. and Wilson, L. B., "The Strain-Energy Expression for Thin Elastic Shells", Trans. ASME, December 1958.
11. Spangler, M. G., "The Structural Design of Flexible Pipe Culverts", Iowa State College, Eng. Exper. Sta. Bull. 153 (1941).
12. Riley, W. F., Daniel, I. M. and Durelli, A. J., Stress Wave Phenomena in Semi-Solids, Contract No. AF29(601)-2564 for AFSWC, Kirtland AFB, New Mexico, Armour Research Foundation, Chicago, Illinois, July 1961.
13. Meyerhof, G. G., "The Ultimate Bearing Capacity of Foundations", Geotechnique, 2, 301 (1951).
14. Sokolovski, V. V., Statics of Soil Media, Butterworths Scientific Publications, London, (1960).

APPENDIX A

AIR-BLAST INDUCED STRESS WAVES IN  
LAUNCH SILOS

by T. A. Zaker

APPENDIX A  
AIR-BLAST INDUCED STRESS WAVES IN  
LAUNCH SILOS

by T. A. Zaker

In the investigation of the vulnerability of hardened missile launch facilities to nuclear attack, there arises the possibility of damage to the underground launch silo structure resulting from transient longitudinal stress conditions induced by air blast at the ground surface. For certain conditions of loading and silo wall geometry, this phenomenon can result in the development of severe cracking or spallation of the wall structure. The purpose of this appendix is to describe a brief investigation of this effect in a representative launch silo.

In this appendix a technique is presented for an analysis of longitudinal stress-wave propagation in the reinforced concrete walls of a missile launch silo caused by surface air-blast pressure. The equations governing the phenomenon are given; the pertinent physical properties of the materials are discussed; and a preliminary analysis of an idealized wall configuration is presented for a surface loading having a peak over-pressure of 300 psi generated by the surface burst of a 1-MT weapon.

1. Theoretical Considerations

When a column of material is subjected to time-dependent surface pressure loading at one end, longitudinal waves of stress are induced and propagate down the length of the column. Such waves give rise to strains and particle velocities which depend on the properties of the medium. When the stresses exceed the proportional limit of the material, the waves are propagated at velocities which depend on the stress amplitude and on the current physical state of the material. Failure by spallation occurs when the local tensile strength of the medium is exceeded, and the material separates locally. The problem can be analyzed on the basis of a one-dimensional model of the system, wherein the physical state variables are regarded as functions of distance along the column and of the time.

ARMOUR RESEARCH FOUNDATION OF ILLINOIS INSTITUTE OF TECHNOLOGY

Consider a column of material of constant cross section, and assume that the stress and particle velocity components parallel to the column axis are uniformly distributed across each section at every instant of time. The differential equations for the local conservation of mass and momentum are

$$\frac{\partial u}{\partial x} = \rho_0 \frac{\partial}{\partial t} \left( \frac{1}{\rho} \right) \quad (\text{A-1})$$

$$\rho_0 \frac{\partial u}{\partial t} + \frac{\partial \sigma}{\partial x} = \rho_0 f \quad (\text{A-2})$$

where

$x$  is initial position coordinate of particle,  
 $t$  is time,  
 $\rho$  is density,  
 $\rho_0$  is initial density, a constant,  
 $u$  is particle velocity,  
 $\sigma$  is compressive longitudinal stress, and  
 $f$  is body force per unit mass.

It is to be emphasized that these equations are written with respect to a Lagrangian frame of reference, in which the initial particle position coordinate ( $x$ ) and time ( $t$ ) are taken as independent variables; no limitations are placed on the magnitudes of particle displacement and velocity. This representation is particularly convenient when the current physical state of a particle depends on its prior deformation history. If we supplement equations A-1 and A-2 with constitutive equations of the medium in the form of stress-density relations  $[\sigma = \sigma(\rho)]$ , a system of two partial differential equations in the two dependent variables,  $u$  and  $\sigma$ , results.

It is convenient to define the compressive longitudinal strain ( $\epsilon$ ) as the current change in length per unit of initial length. Then  $\epsilon = 1 - \rho_0/\rho$ , and if we assume time-independent stress-strain relations of the form  $\sigma = \sigma(\epsilon)$ , equations A-1 and A-2 become



$$E \frac{\partial u}{\partial x} + \frac{\partial \sigma}{\partial t} = 0 \quad (A-3)$$

$$\rho_0 \frac{\partial u}{\partial t} + \frac{\partial \sigma}{\partial x} = \rho_0 f \quad (A-4)$$

where  $E$  is defined by  $E = d\sigma/d\epsilon$  and is not necessarily a constant. Equations A-3 and A-4 are of hyperbolic type and can be written in differential form along so-called characteristic lines in the  $x$ - $t$  plane as follows:

$$d\sigma \pm \rho_0 c du = \rho_0 f dx \quad (A-5)$$

where the positive and negative signs apply respectively on the wave lines

$$dx = \pm c dt \quad (A-6)$$

in which the wave speed ( $c$ ) is defined by  $c = \sqrt{E/\rho_0}$ . Strictly speaking,  $c$  is simply the rate at which a wave traverses the material of the column; the true speed of a wave relative to a frame of reference fixed in space depends not only on  $c$  but also on the local particle velocity and the local strain.

If we suppose the column to be oriented vertically and that the body force ( $f$ ) is due to gravity, then  $f = g$ , where  $g$  is the gravitational acceleration. We may then define  $\bar{\sigma} = \sigma - \rho_0 g x$ , so that equations A-5 become

$$d\bar{\sigma} \pm \rho_0 c du = 0 \quad (A-7)$$

on

$$dx = \pm c dt. \quad (A-6)$$

These are the usual equations for the one-dimensional propagation of longitudinal waves, but the relations between  $\bar{\sigma}$  and  $\epsilon$  here are functions of position in view of the definition of  $\bar{\sigma}$ . However, the body force resulting from gravity is usually assumed small compared to the stress gradients in problems of interest.

ARMOUR RESEARCH FOUNDATION OF ILLINOIS INSTITUTE OF TECHNOLOGY

Equations A-6 and A-7 lend themselves to convenient numerical or graphical computation of wave motion in linear or nonlinear media. By considering piecewise linear stress-strain relations and piecewise constant boundary values of stress, the wave motion may be analyzed on the assumption of regions of uniform physical state in the x-t plane separated by steep-fronted compression or unloading waves and by composition discontinuities. The analysis of each wave-wave interaction (or wave-composition discontinuity interaction) reduces to the application of the appropriate one of equation A-7 in finite-difference form across each wave of the system resulting after interaction, and the satisfaction of the interface conditions of continuity of stress and particle velocity in zones between the waves. Where spallation occurs, the condition of continuity of particle velocity is replaced by a stress boundary condition.

The analysis is readily extended to the case of a column with abrupt changes in cross section area\*. Retaining the one-dimensional formulation and neglecting any stress transmitted to the surrounding medium at the area changes between zones of constant area, the condition of stress continuity must be replaced by continuity of total force across such area changes.

Neglecting body forces, equations A-7 and A-6 may be written for each constant-area zone as

$$dF \pm \rho_0 c dA du = 0 \quad (A-8)$$

on

$$dx = \pm c dt \quad (A-6)$$

---

\* L. Griffis, The Behavior of Longitudinal Stress Waves Near Discontinuities in Bars of Plastic Material, NDRC Report No. A-212, OSRD No. 1799, (September 1943).

where  $F = \sigma A$  is total compressive normal force, and  
 $A$  is cross sectional area

The weighted acoustic impedance ( $\rho_o c A$ ) represents the local slope of characteristic lines in a plane of dependent variables,  $F$  and  $u$ . In the general case,  $\rho_o$  and  $A$  are functions of position, and the local value of  $c$  will depend on the current state of the material if the medium is nonlinear. In a stepwise numerical computation, these values are treated as locally constant, and the state of the material between two opposite-facing waves resulting from a wave-wave interaction or a wave-area discontinuity interaction is determined by the intersection of two characteristics in the  $F$ - $u$  plane. These characteristics correspond respectively to the two opposite-facing waves arising after the interaction. The intersection of characteristics in the  $F$ - $u$  plane enforces the simultaneous equality of force and particle velocity in adjacent states behind opposite-facing waves.

To illustrate this point, consider the interaction of a rightward-moving wave ( $dx = c_1 dt$ ) in zone 1 with an area discontinuity separating zones 1 and 2. In general, the interaction will give rise to a rightward-moving transmitted wave ( $dx = c_2 dt$ ) in zone 2 and a leftward-moving reflected wave ( $dx = -c_1 dt$ ) in zone 1. Regions of uniform state in the  $x$ - $t$  space separated by the discontinuity lines are sketched in figure A-1a. The first digit of the numerical identification denotes the constant-area zone while the second refers to the physical ( $F, u$ ) state shown in figure A-1b. States 0 and 1 are assumed known, and are connected by equation A-8 with the lower sign chosen so as to apply across the rightward-moving incident wave:

$$F_1 - F_0 = \rho_o c_1 A_1 (u_1 - u_0). \quad (A-8a)$$

Similarly equation A-8 with lower sign applies to the unknown jump in properties across the rightward-moving transmitted wave, while equation A-8 with upper sign applies to the unknown jump in properties across the leftward-moving reflected wave:

$$F_2 - F_0 = \rho_0 c_2 A_2 (u_2 - u_0) \quad (A-8b)$$

$$F_2 - F_1 = \rho_0 c_1 A_1 (u_2 - u_1) . \quad (A-8c)$$

State 2 is thus determined in F-u space by the intersection of oppositely directed characteristic lines from each constant-area zone, corresponding to equation A-8 applied in finite form across the opposite-facing resultant waves. The continuity of force and velocity across the area change are obviously satisfied by the intersection of these lines. In the example sketched in figure A-1, the transmitted wave is a wave of compression, while the reflected wave is determined to be an unloading or expansion wave.

By these procedures, the solution to a problem of one-dimensional stress wave propagation can be carried forward graphically in time and distance from given initial and boundary value data. Specification of tensile fracture criteria leads to an assessment of the possibility of spallation in the material; quite complicated failure criteria, such as time-dependent or displacement-dependent forms, can be handled by a semigraphical method.

## 2. Material Properties

The cylinder outside walls of a representative launch silo are of reinforced concrete extending to a depth of about 163.5 ft below grade, and have an inside radius of 27.5 ft. The wall thickness to level 2 at a depth of about 30 ft is 8 ft, and the remainder of the wall is 4 ft in thickness. An annular shoulder of inside radius 13.25 ft and approximately 4 ft in depth connects to the silo wall at grade, and a circular slab 7-ft thick, carrying the flame deflector structure, forms the base of the silo.

The structural concrete used is of 3,750-psi ultimate static compressive strength. Longitudinal (vertical) reinforcing steel is specified as No. 14 bars spaced at 9 inches in each face in the 8-ft thick wall section, and No. 14 bars spaced at 18 inches in each face in the 4-ft section. Deformed billet steel bars are called for in accordance with ASTM

specification A432-59T\*. These bars have a static yield strength of 60,000 psi and an ultimate tensile strength of 90,000 psi at 7 percent elongation. Each bar has a cross sectional area of 2.25 sq in.

A dynamic yield stress of 4,875 psi is specified in the concrete, and a minimum dynamic yield stress of 75,000 psi is called for in the reinforcing steel.

The area of the annular shoulder presented to surface pressure (loaded area) is 3410 sq ft. The silo closure is carried on a girder structure, and is assumed to act independently of the silo walls. The cross sectional area of the 8-ft section (Section 1) is 1582 sq ft, while that of the 4-ft section (Section 2) is 742 sq ft. The area of the base is 3120 sq ft.

The weight density of concrete is taken to be 150 lb per cu ft, while that of the soil below the silo is taken as 120 lb per cu ft. The seismic velocity in the soil below is assumed to be 7000 fps.

From these data, composite force-strain curves were constructed for sections 1 and 2 of the silo by addition of piecewise linear force-strain curves for steel and concrete at equal strain. The total steel area in section 1 is 1187 sq in., and that in section 2 is 556 sq in. assuming 6 inches of concrete cover over the steel circles in each face. Young's modulus for steel was taken as  $30 \times 10^6$  psi, while that for concrete was assumed to be 1000 times the static compressive strength, or  $3.75 \times 10^6$  psi. Perfectly plastic behavior was assumed in the concrete at compressive strains greater than the yield strain of 0.001, and the concrete was assumed ineffective in tension.

The piecewise linear force-strain curves for concrete and steel in sections 1 and 2 are shown in figure A-2, while the composite curves are given in figure A-3. It is apparent that the contribution of the steel to the strength of the composite in compression is quite small. On the other

---

\* Deformed Billet Steel Bars for Concrete Reinforcement with 60,000 psi Minimum Yield Point, ASTM Stds., 1959 Suppl., Pt. 1, 242-246.

hand, the strength of the steel in tension is of the order of the tensile strength of the concrete, if the latter were taken at the commonly assumed value of 10 percent of the compressive strength.

The curves shown in figure A-3 can be applied as the constitutive data in a dynamic problem if no credit is taken for any increase in strength owing to dynamic effects; such increases are, at best, uncertain quantities, and their omission will generally result in an underestimate of the applied loading required to cause significant damage.

Hysteresis effects, resulting from compression beyond the yield point and subsequent unloading, are shown in the individual force-strain curves and in the composite curves. Hysteresis effects, in general, give rise to permanent deformation or residual strains under sufficiently intense loading. The wave speed corresponding to each linear segment of the composite force-strain relations is to be calculated from

$$c = \frac{1}{A} \sqrt{\frac{1}{\rho_0} \frac{dF}{d\epsilon}} \quad (A-9)$$

where  $A$  is the nominal cross sectional area. With the assumption of negligible tensile strength in concrete, it is seen from figure A-3 that severe yielding and steel fracture would occur at tensile forces of about  $110 \times 10^6$  lb in section 1 and about  $50 \times 10^6$  lb in section 2.

### 3. Stress Wave Problem

In view of the discussion of material properties, some aspects of the stress wave propagation problem in silo walls can be illustrated by investigation of a simplified model neglecting the effect of reinforcing steel. To this end, we consider a model of the silo wall consisting of a column of plain concrete having a single area change (Sections 1 and 2), and assume the tensile strength of concrete to be 10 percent of its static compressive strength, or 375 psi.

The masses of the annular shoulder and base slab are neglected, and these components are assumed to act simply as load transmitters from the air and to the soil below. The force at the base of the silo walls is assumed to be transmitted to a semi-infinite column of soil (Section 3) equal in area to the silo base slab, and linear elastic behavior is assumed in the soil. Properties of sections 1, 2, and 3 for the elastic range of behavior are given in the table A-1. The wave speed ( $c$ ) for the concrete is calculated from  $c = \sqrt{E/\rho_o}$ .

Table A-1

Section	0	1	2	3
Component	Shoulder	8-ft wall	4-ft wall	Soil
A, sq ft	3410	1582	742	3120
$\rho_o$ , lb-sec <sup>2</sup> /in. <sup>4</sup>	----	$2.25 \times 10^{-4}$	$2.25 \times 10^{-4}$	$1.80 \times 10^{-4}$
c, fps	----	$10.65 \times 10^3$	$10.65 \times 10^3$	$7.0 \times 10^3$
$\rho_o c A$ , lb-sec/in.	----	$6.62 \times 10^6$	$3.10 \times 10^6$	$6.78 \times 10^6$

The loading is assumed to be a pulse of peak overpressure 300 psi resulting from the surface burst of a 1-MT weapon. A simplified representation of the overpressure-time history at the ground for surface busts has been developed by Newmark\* from theoretical solutions to the point-source explosion problem in free air. The representation is based on the replacement of the actual pressure-time curve by two straight line segments. From the

---

\* N. M. Newmark and W. J. Hall, Preliminary Design Methods for Underground Protective Structures (U), AFSWC TR-60-5 p. 3-16 (December, 1959) SECRET.

initial peak of 300 psi, the overpressure decays linearly with time to about 68 psi at time  $t_1 = 62$  msec and then linearly to zero at time  $t_2 = 700$  msec.

In view of the area of the shoulder, the initial peak force applied to the system is  $147 \times 10^6$  lb. The wave pattern calculated by the techniques presented earlier is shown in the x-t diagram of figure A-4 up to  $t = 35$  msec, together with a schematic diagram of the model sketched along the distance axis. The linear decay of the loading is replaced as shown by two constant-pressure intervals, the decrease from the initial pressure occurring at about  $t = 11.5$  msec. The initial digit of the numerical identification of regions in the x-t diagram of figure A-4 refer to the constant-area zones in the model, while the remaining digits refer to the corresponding force-velocity states shown for clarity in two F-u diagrams, figures A-5 and A-6. Compression waves are shown in figure A-4 as solid lines, while unloading waves are shown as dashed lines.

The principal characteristics through the origin of the F-u plane for the linear elastic range in each section of the concrete column and in the soil are shown in figures A-5 and A-6. The slope of each of these lines is equal to the corresponding weighted acoustic impedance ( $p_o c A$ ). Every other line segment in these diagrams has a slope equal in absolute value to that of the corresponding principal characteristic through the origin. The tensile forces required to produce failure in sections 1 and 2 are also shown along the negative F-axis on the assumption that the tensile strength of concrete is 10 percent of its static compressive strength.

It is apparent that, for the surface loading considered in this problem, the material remains elastic and well within acceptable stress limits. Velocities up to about 40 ips are attained (State 4, Fig. A-5), and a maximum compressive force of about  $180 \times 10^6$  lb develops (State 16, Fig. A-5) at the base of the silo wall upon reflection of waves at the silo-soil interface. As the surface pressure loading continues to decay, the forces and velocities in the system can be expected to decrease continually toward zero (Fig. A-6).

From figure A-4, observe that the surface pressure decays to half its initial value at about  $t = 40$  msec. This characteristic of the loading

ARMOUR RESEARCH FOUNDATION OF ILLINOIS INSTITUTE OF TECHNOLOGY



corresponds to nearly three transits of a stress wave down the length of the silo. Owing to the relatively slow decay of the assumed surface loading, no appreciable tensile stresses are expected to develop in the model. On the other hand, it is clear that for intense surface pressure of sufficiently short duration (of the order of a fraction of the transit time of a stress wave down the silo length) severe tensile forces may develop near the area discontinuity between sections 1 and 2 upon emergence at the surface of the reflection of the initial input wave from the base of the silo (note State 21, Fig. A-6). This indicates that spallation damage to the silo structure is more likely to occur as a result of intense, short-duration loading from, say, the air blast caused by a close near-surface high-explosive burst than from that caused by MT-range nuclear weapon in the 300-psi overpressure region. It is precisely this effect which accounts for the so-called close-in "brisance" of a high explosive and leads to severe scabbing and fracturing of solids in contact explosions.

Finally, it may be noted that body forces have tacitly been assumed negligible in the foregoing analysis. The dead-load compressive stress at the base of the silo wall may, in reality, be as high as about 200 psi if the entire weight of the silo wall structure is carried by the walls and base slab. However, the material is found to remain linearly elastic throughout the motion considered in this problem, and, in such a case, it can be shown that dead-load forces may simply be added to those obtained from the analysis neglecting body forces, in accordance with a transformation similar to that discussed in connection with equation A-7. In general, this is not possible when plastic flow and fracture occur in a problem.

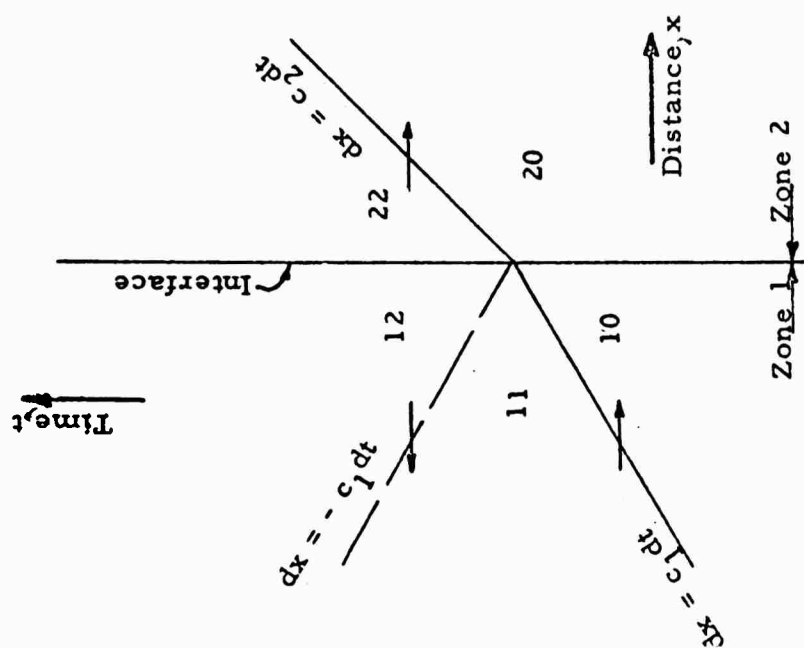
#### 4. Conclusion

A technique has been presented for an analysis of the stress-wave transmission and spallation problem in a representative missile launch silo resulting from surface air-blast pressure loading. A preliminary analysis of the problem has been carried out on the basis of a highly simplified model of the silo-wall system, and composite force-strain curves for the reinforced concrete of the silo walls have been devised for use in a more sophisticated analysis.

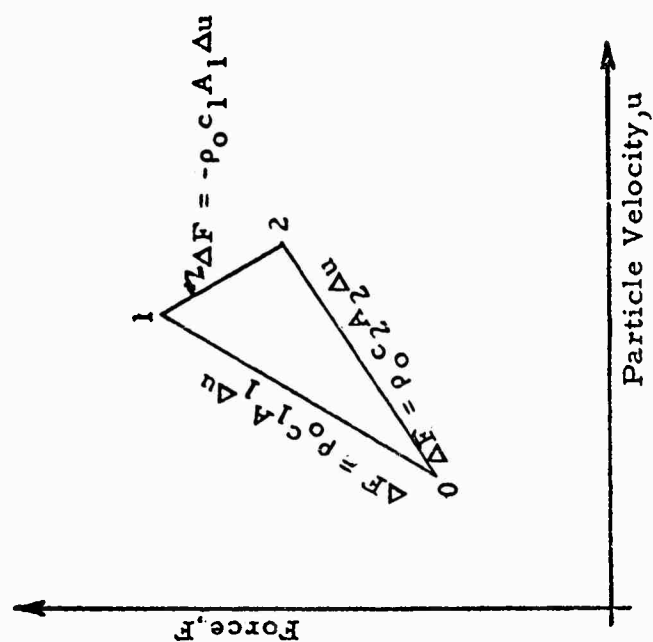
ARMOUR RESEARCH FOUNDATION OF ILLINOIS INSTITUTE OF TECHNOLOGY

The analysis of the plain concrete model under loading resulting from a 1-MT surface burst in the 300-psi overpressure region indicates that decay times associated with this type of loading are sufficiently large compared to the transit time of a stress wave down the length of the silo so that severe tensile forces are not likely to develop. On the other hand, it is observed that intense, short-duration air-blast pressure may result in strong tensile waves and consequently spallation or scabbing of the material.

Further investigation should be directed toward the establishment of load parameters under which severe damage of this type may occur. In addition, significant improvement can be made to the one-dimensional model described here. These improvements should be based on more realistic treatment of coupling between the motion of silo walls and that of the closure and base slab, and between the motion of the base slab and that of the soil below the silo. Various degrees of elastic and anelastic coupling can be considered along with equivalent-mass addition to the system with time, within the frame-work of the one-dimensional formulation.

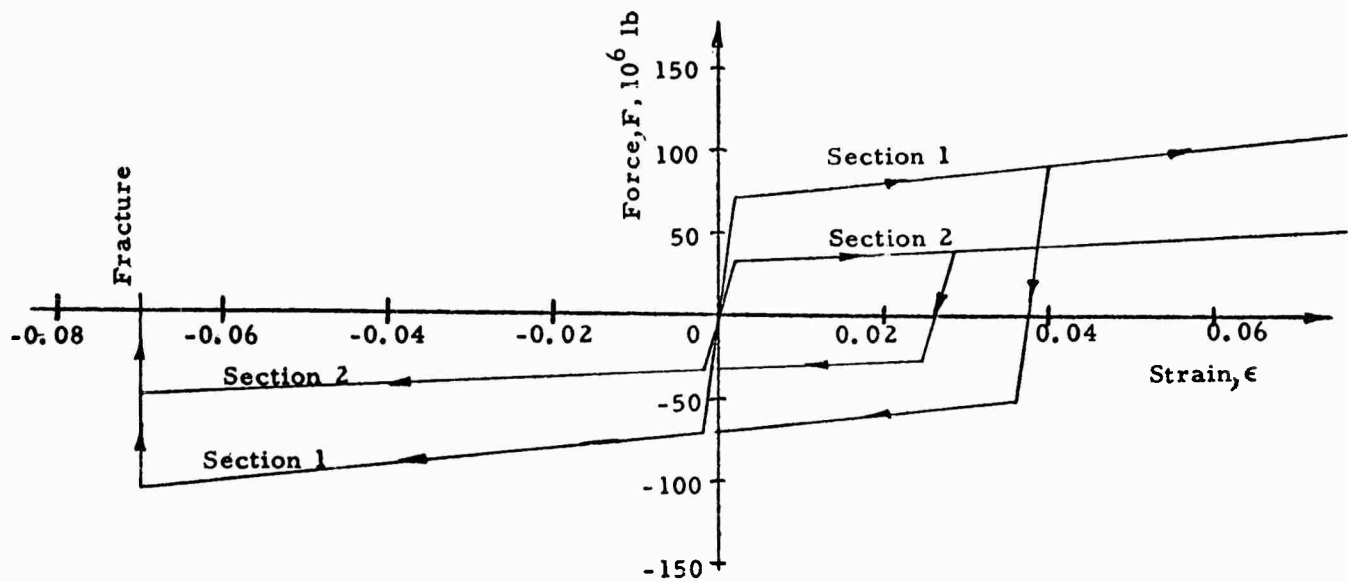


a. x-t Diagram

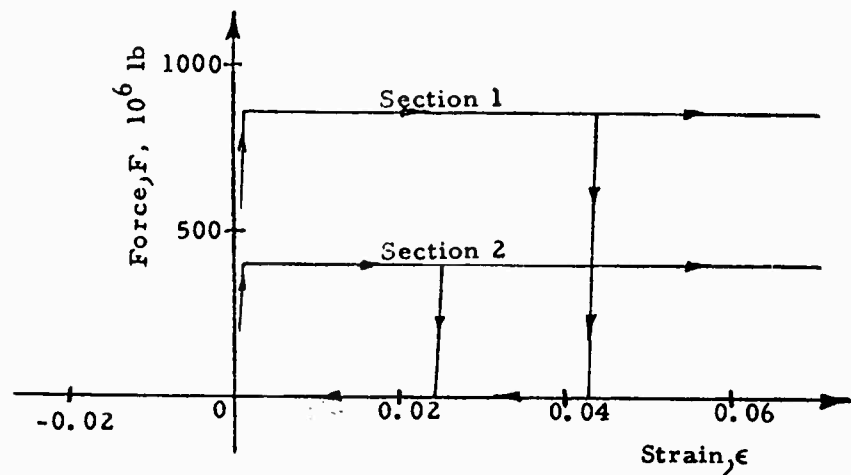


b. F-u Diagram

Fig. A-1 WAVE AND STATE DIAGRAMS FOR WAVE-AREA DISCONTINUITY INTERACTION



a. Reinforcing Steel



b. Concrete

Fig. A-2 FORCE-STRAIN RELATIONS FOR STEEL AND CONCRETE

ARMOUR RESEARCH FOUNDATION OF ILLINOIS INSTITUTE OF TECHNOLOGY

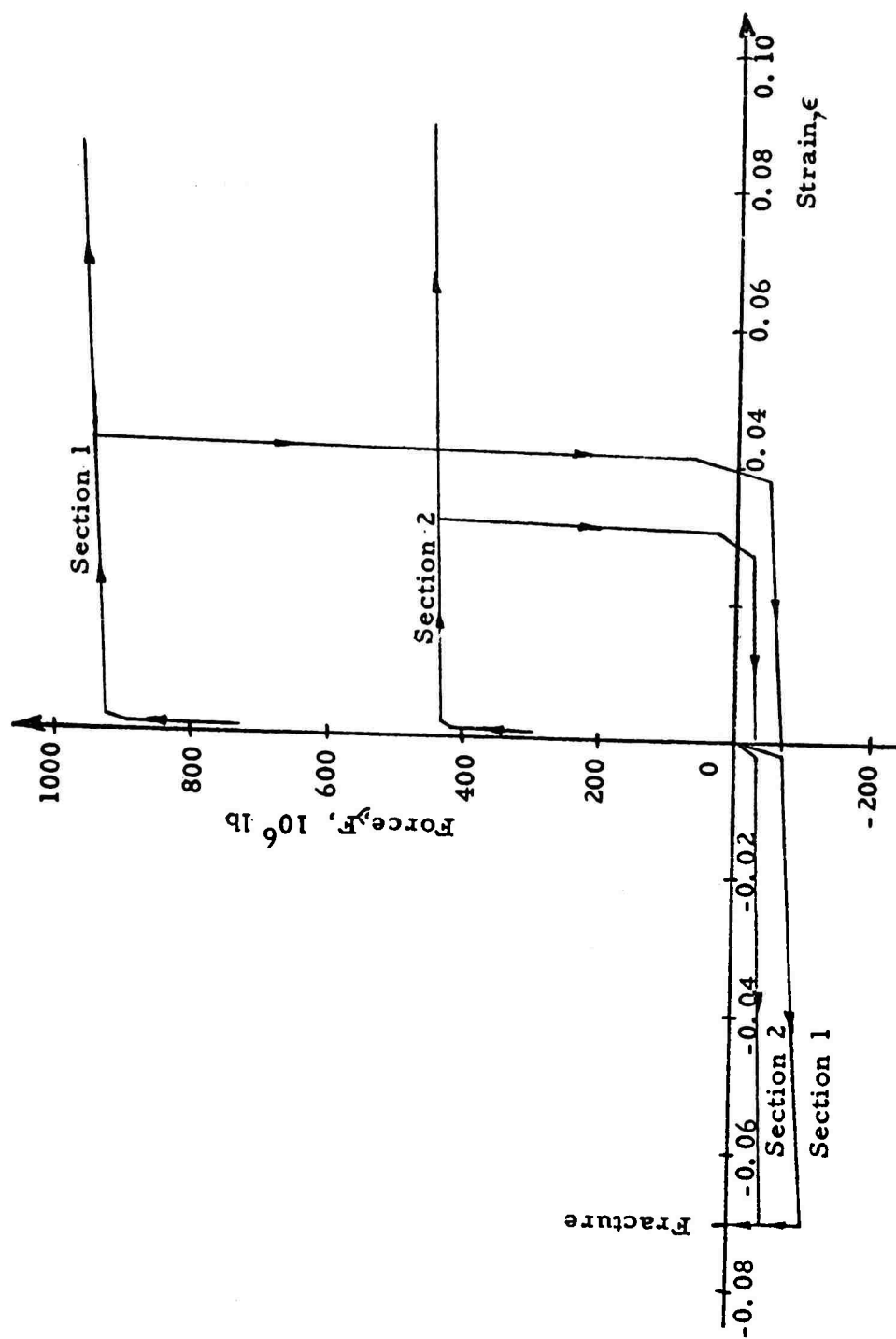


Fig. A-3 COMPOSITE FORCE-STRAIN RELATIONS FOR SILO WALLS

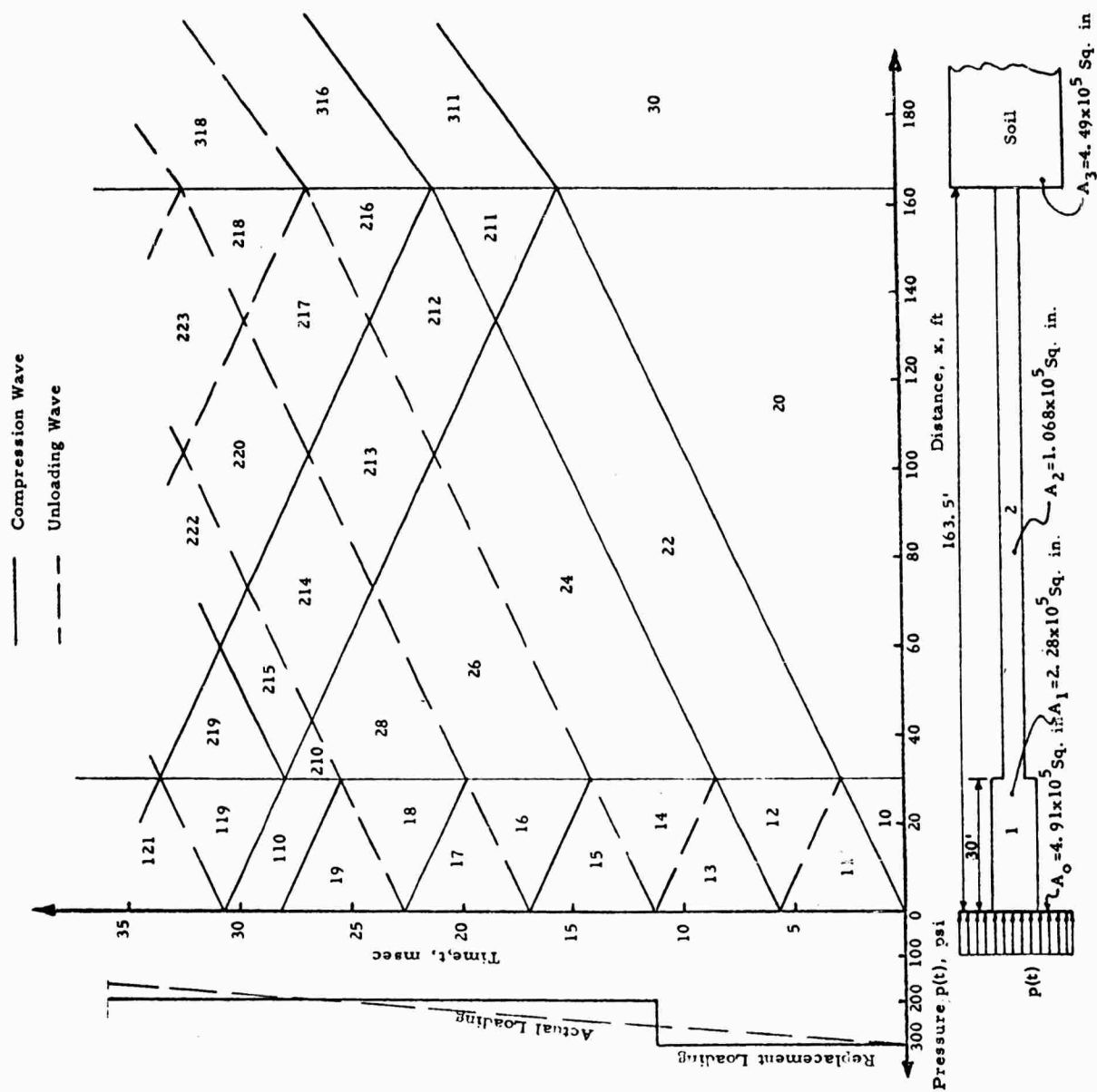


Fig. A-4 WAVE DIAGRAM FOR SILO WALL MODEL

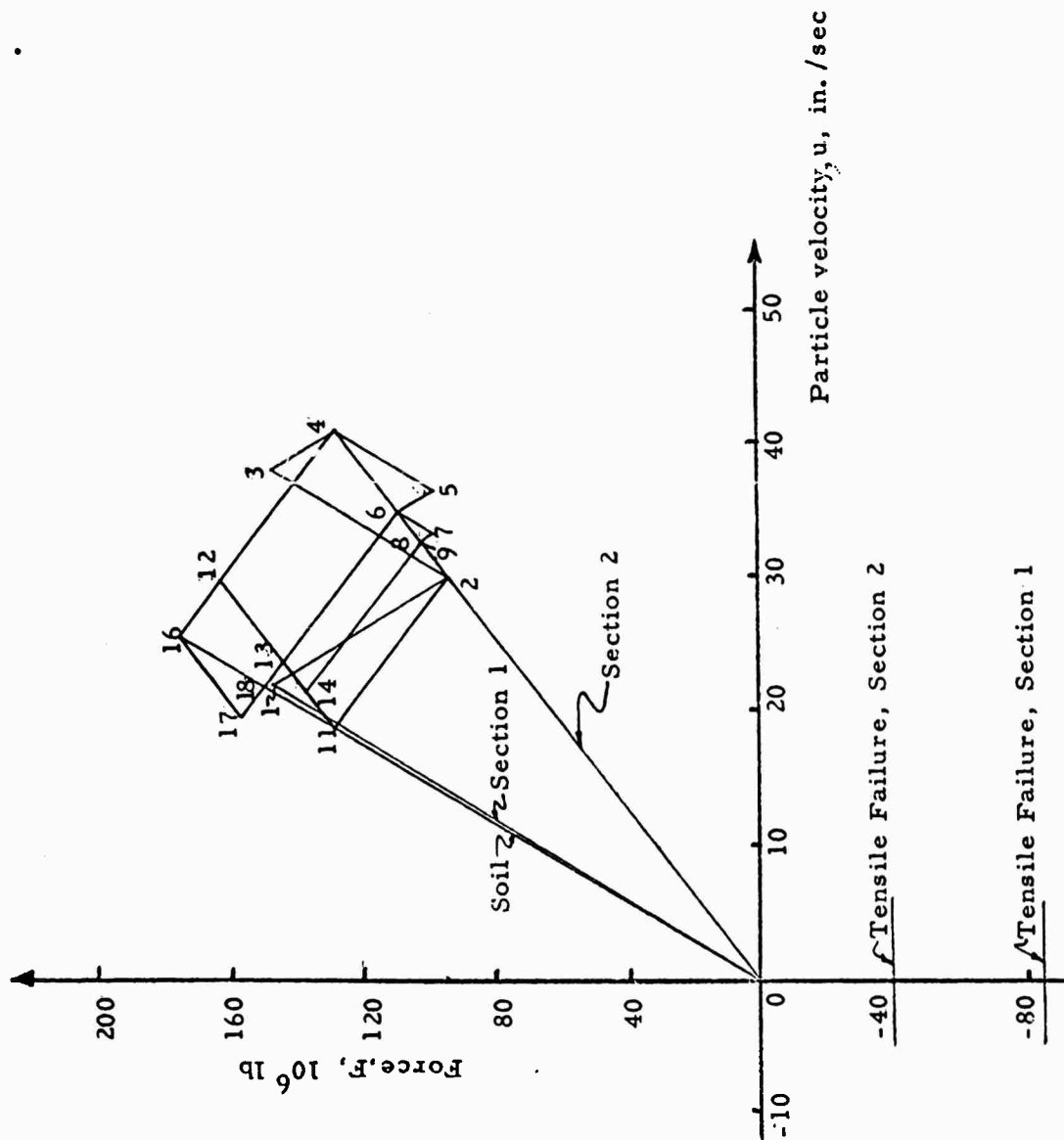


Fig. A-5 STATE DIAGRAM FOR SILO WALL MODEL, I

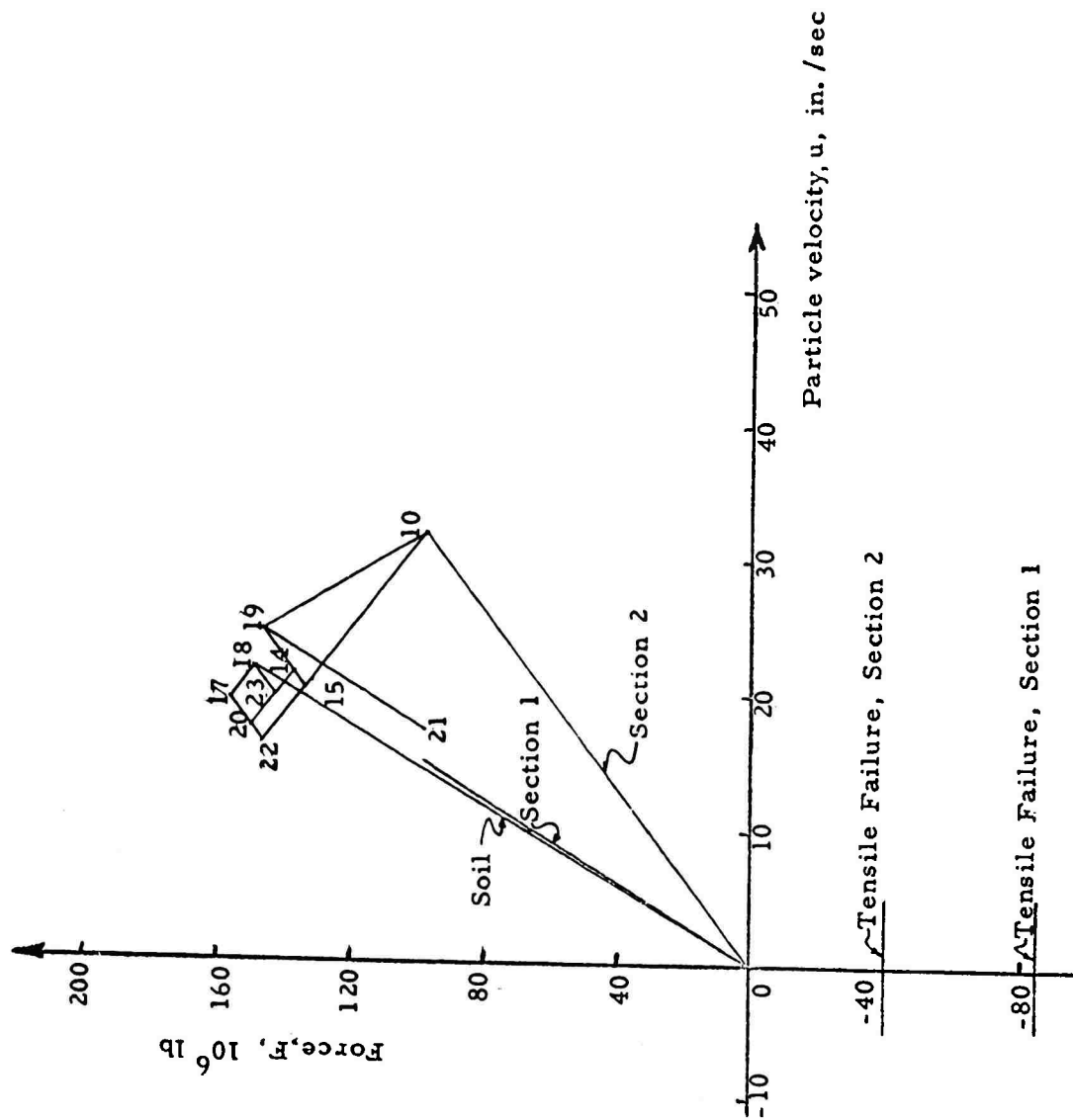


Fig. A-6 STATE DIAGRAM FOR SILO WALL MODEL, II



APPENDIX B  
PLAIN STRAIN SOLUTION FOR THE DISPLACEMENTS AT  
BOUNDARY OF A CIRCULAR HOLE IN AN INFINITE  
ELASTIC PLATE

APPENDIX B  
PLAIN STRAIN SOLUTION FOR THE DISPLACEMENTS AT  
BOUNDARY OF A CIRCULAR HOLE IN AN INFINITE  
ELASTIC PLATE

The plain strain solution for the displacements at the boundary of a circular hole in an infinite elastic plate for the case of a radial load varying as  $\cos n \theta$  can be obtained from the general solution of the two-dimensional problems in polar coordinates\*. The stress function for loads varying as  $\cos n \theta$  is

$$\phi = \left[ a_n r^n + b_n r^{-n} + c_n r^{2+n} + d_n r^{2-n} \right] \begin{matrix} \sin n \theta \\ \cos n \theta \end{matrix} \quad (B-1)$$

where  $n \geq 2$

The corresponding stresses are

$$\sigma_{rr} = \left[ a_n (n-n^2) r^{n-2} - b_n (n+n^2) r^{-n+2} + c_n (2+n-n^2) r^n + d_n (2-n-n^2) r^{-n} \right] \cos n \theta, \quad (B-2)$$

$$\sigma_{\theta\theta} = \left[ a_n (n^2 - n) r^{n-2} + b_n (n+n^2) r^{-n+2} + c_n (2+3n+n^2) r^n + d_n (2-3n+n^2) r^{-n} \right] \cos n \theta, \quad (B-3)$$

$$\sigma_{r\theta} = \left[ a_n (n^2 - n) r^{n-2} - b_n (n+n^2) r^{-n+2} + c_n (n+n^2) r^n + d_n (n-n^2) r^{-n} \right] \sin n \theta. \quad (B-4)$$

---

\* Timoshenko and Goodier, Theory of Elasticity, 2nd Edition, p. 116, McGraw-Hill Book Co., N. Y. (1951).

We consider the infinite plate with a circular hole of radius,  $a$ , subjected to the internal pressure,  $p \cos n \theta$ , where  $n \geq 2$ . The boundary conditions at  $r = a$  are

$$\sigma_{rr} = -p \cos n \theta, \sigma_{r\theta} = 0, \text{ at } r = a. \quad (\text{B-5})$$

Since the loading is self-equilibrated, the stresses at infinity must go to zero as  $\frac{1}{r^2}$ . Hence

$$a_n = c_n. \quad (\text{B-6})$$

Substituting the expressions for the stresses into the boundary conditions, we obtain

$$-b_n(n+n^2)a^{-n-2} + d_n(2-n-n^2)a^{-n} = -p$$

$$-b_n(n+n^2)a^{-n-2} + d_n(n-n^2)a^{-n} = 0.$$

Hence

$$\left. \begin{aligned} b_n &= -\frac{pa^{n+2}}{2(n+1)} \\ d_n &= \frac{pa^n}{2(n-1)} \end{aligned} \right\} \quad (\text{B-7})$$

The radial displacement at  $r = a$  for plain strain is

$$u_r \Big|_{r=a} = \frac{1}{E} \left\{ b_n(1+\nu) n a^{-n-1} + d_n \left[ 4(1-\nu^2) - (1+\nu)(2-n) \right] a^{-n+1} \right\} \cos n \theta \quad (\text{B-8})$$

or, using equation B-7,

$$u_r \Big|_{r=a} = \frac{pa}{E} \left[ \frac{2n+1}{n^2-1} (1+\nu)(1-2\nu) \right] \cos n \theta. \quad (\text{B-9})$$

Now  $\frac{E}{(1+\nu)(1-2\nu)}$  is the apparent modulus of uniaxial strain which we have defined as  $E_c$ . The ratio of radial pressure to displacement gives the value of  $k$ , hence

$$ka = E_c \frac{n^2 - 1}{2n + 1}, \quad n \geq 2. \quad (B-10)$$

APPENDIX C

COMPUTER PROGRAM FOR SHELL RESPONSE TO RADIAL PRESSURE

## APPENDIX C

### COMPUTER PROGRAM FOR SHELL RESPONSE TO RADIAL PRESSURE

The flow diagram for the program machine code is given in figure C-1. An algebraic programming language is employed based on the Internal Translator (IT)\* originally developed at Carnegie Institute of Technology, and serves as basic input to the UNIVAC 1105 compiler. The following nomenclature has been used in the computer program. Variables marked with a single asterisk are required input data for the program and those with a double asterisk are output variables. Variables defined within the program are not listed here.

$$Y0^{**} = \tau, \left(\frac{ct}{a}\right), \text{ nondimensional time}$$

$$Y1^{**} = x_n, \left(\frac{a_n}{a}\right), \text{ nondimensional modal displacement}$$

$$Y2^{**} = x'_n, \left(\frac{\dot{a}_n}{c}\right), \text{ nondimensional modal velocity}$$

$$Y20^{**} = ka / \rho c^2$$

$$Y21^{**} = s / \rho c$$

$$C33^*, Y22^{**} = K_{m_v}, \text{ virtual mass coefficient}$$

$$C41^*, Y23^{**} = \tau_1, \left(\frac{ct_1}{a}\right)$$

$$C40^*, Y24^{**} = \beta, \text{ free-field stress biaxial ratio}$$

$$C43^*, Y25^{**} = \tau_F, \text{ last value of } \tau \text{ ( } \tau_F \leq 99 \Delta \tau_T \text{ )}$$

$$C30^*, Y31^{**} = a/h, \text{ shell radius to thickness ratio}$$

---

\* A. J. Perlis, J. W. Smith, and H. R. Van Zoeran, "Internal Translator (IT) A Compiler for the 650", Computation Center Report, January 1957.

$$Y32^{**} = \rho / \rho_s$$

$$Y33^{**} = \bar{E}/ka$$

$$Y34^{**} = \frac{\sigma_o}{ka} \frac{a}{h}$$

$$C42^*, Y35^{**} = \Delta \tau_T, \text{ Type-Out interval}$$

$$Y49^{**} = \omega_n, \text{ natural frequency in nth mode}$$

$$Y104^{**} = ka/E^*$$

$$C44^*, Y105^{**} = \lambda_4 \begin{cases} 1, & \text{for addition of fictitious buckling pressure} \\ 0, & \text{for omission of fictitious buckling pressure} \end{cases}$$

$$CO^{**} = \delta \tau, \text{ integration interval}$$

$$C31^* = \rho, \text{ soil density (lb-sec}^2\text{-in}^{-4}\text{)}$$

$$C32^* = \rho_s, \text{ shell density (lb-sec}^2\text{-in}^{-4}\text{)}$$

$$C34^* = c, \text{ stress wave velocity (ips)}$$

$$C35^* = s, \text{ damping coefficient (lb-sec-in}^{-3}\text{)}$$

$$C36^* = \sigma_o, \text{ peak free-field pressure (psi)}$$

$$C37^* = E^*, \text{ apparent soil modulus (psi)}$$

$$C38^* = ka, \text{ foundation modulus times shell radius (psi)}$$

$$C39^* = E, \text{ Young's modulus of shell (psi)}$$

$$I11^* = n_i, \text{ initial displacement mode}$$

$$I19^* = n_F, \text{ final displacement mode}$$

$$I24^* = \begin{cases} 0, & \text{Short Program, No output at } \theta = \frac{\pi}{4}, \frac{\pi}{2} \dots \\ 1, & \text{Long Program, } x_n \text{ and } p_n \text{ output at } \theta = \frac{\pi}{4} \dots \end{cases}$$

MJ1 Switch  $\left\{ \begin{array}{l} \text{Off, Typeout: Header, Rigid Body Mode (n = 1)} \\ \text{Static Solution, and } \sum \text{ output} \\ \text{On, Typeout: Same as per off position plus each mode} \\ \text{output} \end{array} \right.$

Table C-1 identifies the four columns of output from the computer program. Rows that do not have the letter, U, in the comments column are not typed if the MJ1 switch is off. Unless indicated to the contrary, all response output is for the head-on point ( $\theta = 0^\circ$ ). If the input value of I24 = 0, the displacements and pressures at  $\theta = \pi/4, \pi/2 \dots$  are not computed. In the static and summation ( $\sum$  output) portion of the list, the following abbreviations are used

$$W(\theta) = \sum_N^{n_F} \frac{a_n}{a} \cos n \theta, \quad \left\{ \begin{array}{l} N = 2 \text{ for } n_i = 1 \\ N = n_i \text{ otherwise} \end{array} \right.$$

$$P(\theta) = \sum_N^{n_F} \frac{p_n}{\sigma_o} \cos n \theta, \quad \left\{ \begin{array}{l} N = 0 \text{ for } n_i = 1 \\ N = n_i \text{ otherwise} \end{array} \right.$$



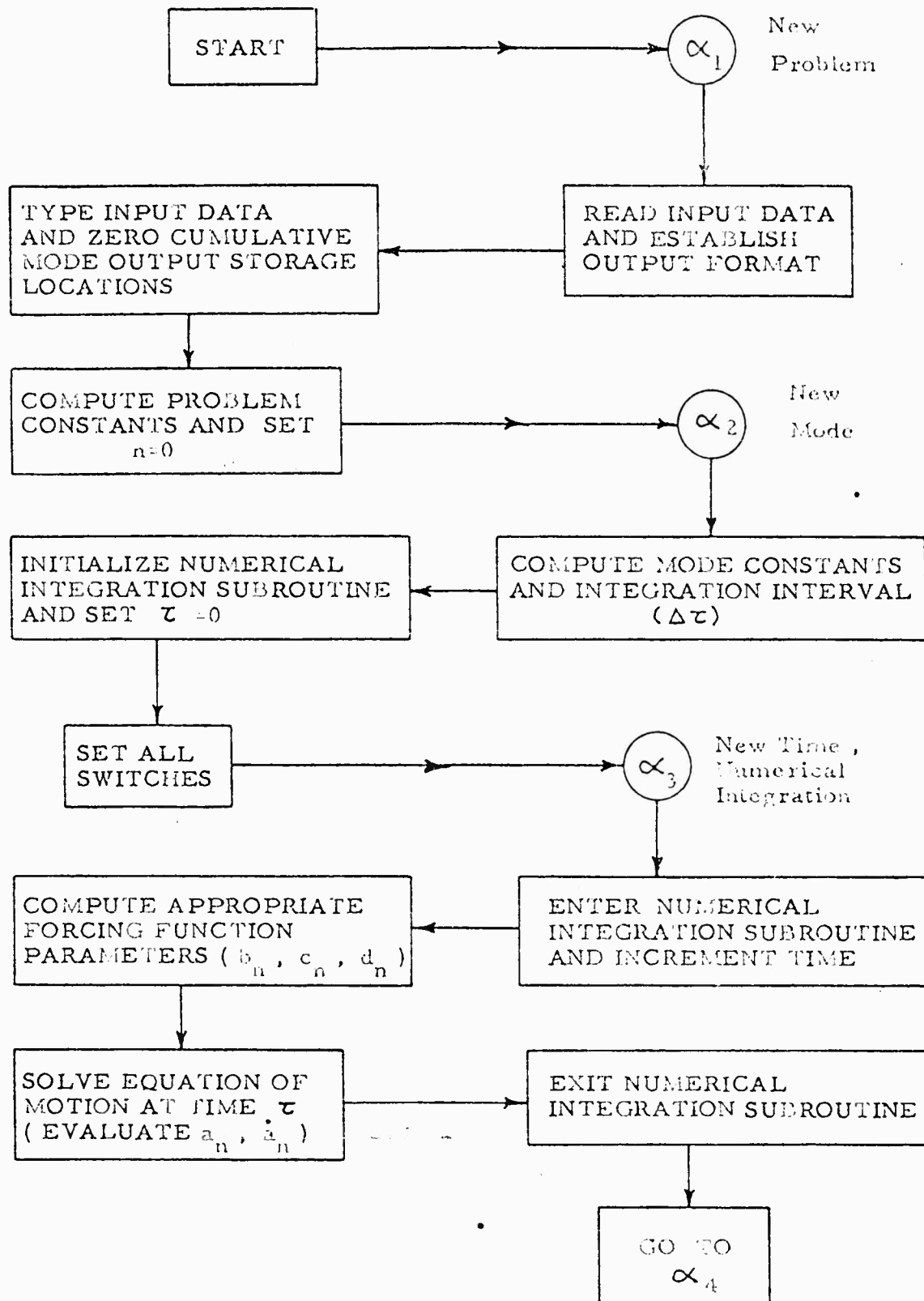


Fig. C-1 FLOW DIAGRAM FOR MACHINE CODE

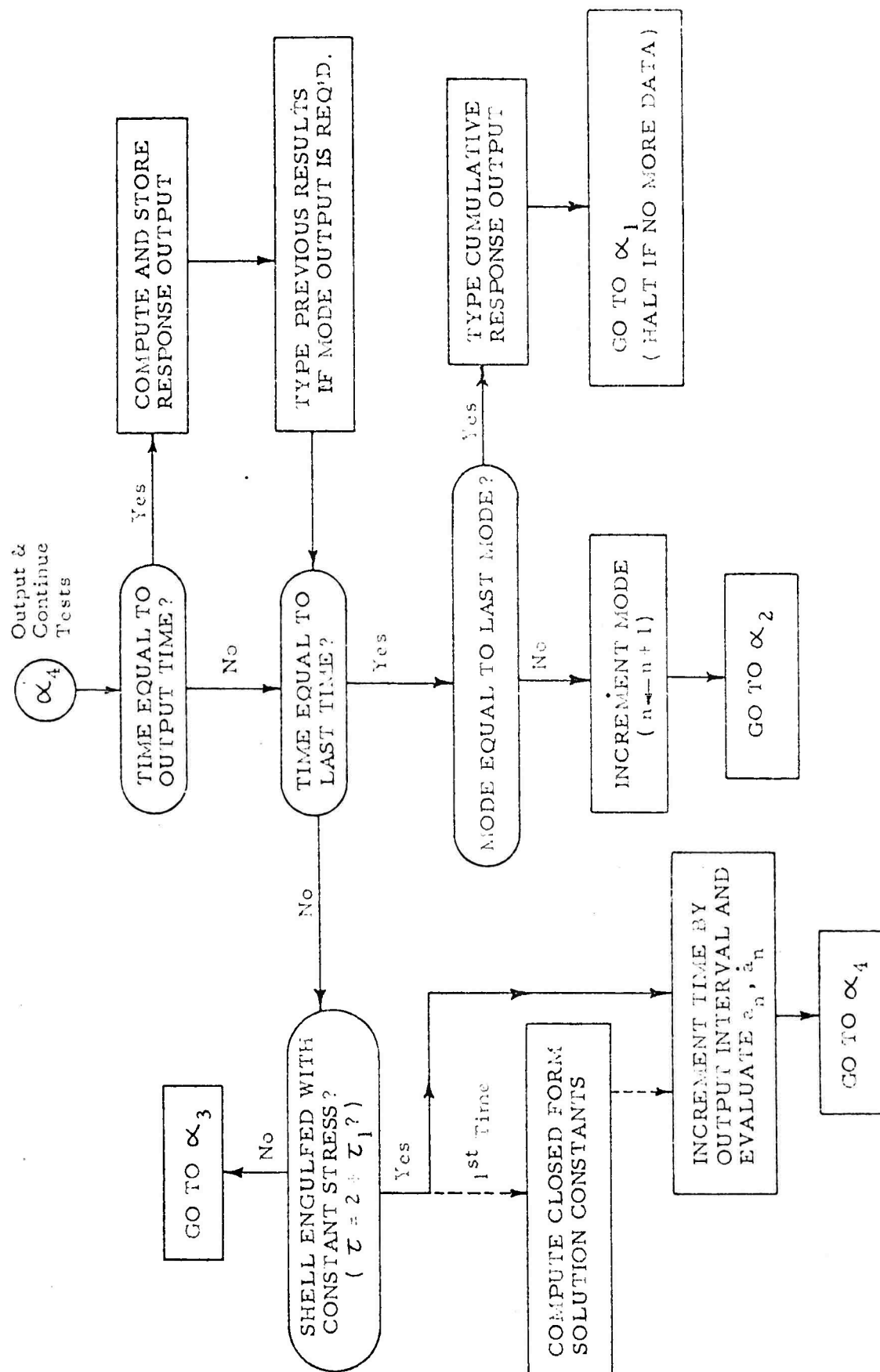


Fig. C-1 (Cont.) FLOW DIAGRAM FOR MACHINE CODE

Table C-1  
OUTPUT FORMAT

Field 1	Field 2	Field 3	Field 4	Comments		
$ka/\rho c^2$	$s/\rho c$	$K_{m_v}$	$\tau_1$	U	Header	
-	-	$ka/E$	$\lambda_4$	U		
$\beta$	$\tau_F$	$a/h$	$\rho/\rho_s$	U		
-	$\bar{E}/ka$	$\sigma_o a/kah$	$\Delta\tau_T$	U		
-	-	300	$\delta\tau$		For $n = 1$	
-	-	-	-			
$n$	$\omega_n$	-	-			
0	0	0	0			
$\tau$	$f_o/\sigma_o$	0	$p_o/\sigma_o$	Repeat to $\tau_F$		For $n \geq 1$ Repeat to $n_F$
$x_1$	$x'_1$	0	$p_1/\sigma_o$			
$\vdots$	$\vdots$	$\vdots$	$\vdots$	U		
$\tau_F$	$f_o/\sigma_o$	0	$p_o/\sigma_o$			
$x_1$	$x'_o$	0	$p_1/\sigma_o$			
-	-	300	$\delta\tau$	U		
-	-	-	0			
$n$	$\omega_n$	0	0			
0	0	0	0			
$\tau$	0	0	0			
$x_n$	$f_n/\sigma_o$	$M_n/\sigma_o a^2$	$p_n/\sigma_o$	Repeat to $\tau_F$	Static Solution	
$\vdots$	$\vdots$	$\vdots$	$\vdots$			
$\tau_F$	0	0	0			
$x_n$	$f_n/\sigma_o$	$M_n/\sigma_o a^2$	$p_n/\sigma_o$			
-	-	-	0	U		
-	-	-	0	U		
$W(0)$	$(f_D + f_B)/\sigma_o$	$M/\sigma_o a^2$	$P(0)$	U		
$W(\pi/4)$	$W(\pi/2)$	$W(3\pi/4)$	$W(\pi)$	U		
$P(\pi/4)$	$P(\pi/2)$	$P(3\pi/4)$	$P(\pi)$	U		
-	-	-	0	U		
-	-	-	0	U		
$\tau$	0	0	0	U		
$W(0)$	$f_n/\sigma_o$	$M_n/\sigma_o a^2$	$P(0)$	U		
$W(\pi/4)$	$W(\pi/2)$	$W(3\pi/4)$	$W(\pi)$	U		
$P(\pi/4)$	$P(\pi/2)$	$P(3\pi/4)$	$P(\pi)$	U		
$\vdots$	$\vdots$	$\vdots$	$\vdots$	U		

ARMOUR RESEARCH FOUNDATION OF ILLINOIS INSTITUTE OF TECHNOLOGY

IT CORRECTION PROGRAM JOB D88  
CHARGE K199:OPTIONAL DYNAMIC RING BENDING:RRR:2118

SEP 11 1961

REEL B366

L21

I 30 Y 530 C 1000 S 95 E2,3,4,6,8

1.	57	50:120:130:1.999,
1.05	65	G50 IF 120:530
1.1		Y120:#0.0
2.	50	C120:#0.0
2.5		C20:#3.1415927
2.7		I0:#2
3.		G21
3.1	1	Y20:#C38/C31*C34*C34
3.2		Y21:#C35/C31*C34
3.3		Y22:#C33
3.45		Y23:#C41
3.5		Y24:#C40
3.55		Y25:#C43
3.6		Y31:#C30
3.65		Y32:#C31/C32
3.7		Y33:#C39/C38
3.75		Y34:#C36*C30/C38
3.8		Y35:#C42
3.85		Y104:#C38/C37
3.9		Y105:#C44
4.	91	TY20 TY21 TY22 TY23
4.1	79	TY104 TY105
5.	80	TY24 TY25 TY31 TY32
6.	81	TY33 TY34 TY35
7.	92	Y36:#Y21/Y20
8.		Y30:#I11*I11
9.		Y41:#Y30/Y30+1.0
10.		Y42:#Y30-1.0
11.		Y37:#Y41*Y32*Y34*Y20
12.		Y30:#Y41*Y31*Y32
13.		Y38:#Y30*Y21
14.		Y43:#Y30*Y20
15.		Y39:#Y42*Y33/12.0*Y31*Y31*Y31
16.		Y40:#Y105*Y33*Y34/2.0*Y31*Y33*Y31
17.		Y47:#1.0+Y30*Y22/I11
18.		Y48:#(1.0+Y42*Y39)*Y43/Y47
19.		Y49:#06E*Y480
20.		Y30:#C20/6.0*Y49
21.		Y26:#Y35
22.		I18:#1
23.		I15:#1.0+Y35/Y30
24.		C0:#Y45/I15
25.		T(300.)TC0
26.		C10:#1.0+Y24
27.		C11:#(C10/2.0)+(1.0-Y24)/4.0
28.		C12:#(1.0-Y24)/2.0
29.		C13:#(1.0-Y24)/4.0
30.		C14:#C20*Y23
31.		C15:#1.0+Y104+Y24
32.		C16:#Y23/2.0
33.		C17:#(1.0+Y104-Y24)/2.0
34.		C18:#C11+0.375
35.		C19:#(3.0-2.0*Y24)/8.0
36.		Y27:#Y31*Y33/2.0*Y33+Y31

ARMOUR RESEARCH FOUNDATION OF ILLINOIS INSTITUTE OF TECHNOLOGY

37.		Y28:#Y42*Y33/12.0*Y34*Y31*Y31	u
37.1		G76 IF I24#0	u
37.2		C25:#I11*C20/4.0	u
37.3		66:I23:1:1.3:	u
37.4	66	C(20+I23):#Q4E,I23*C250	u
37.5		G78 IF I11:1	u
37.6		C24:#-1.0	u
37.7		G76	u
37.8	78	C24:#-C24	u
38.	76	Y79:#Y27/Y31	u
39.		Y29:#A.0*Y28*Y31*Y31	u
40.		I17:#25	u
40.5		I22:#24	u
41.	23	Y0:#0.0	u
42.		Y1:#0.0	u
43.		Y2:#0.0	u
44.		T(0.)	u
45.		TI11 TY49 T(0.) T(0.)	u
46.		TY0 TY1 TY2 T(0.)	u
47.		G7	u
48.	2	G35 IF Y23#0.0	u
49.		G117 IF Y0:#2.0	u
50.		Y44:#0BE,1.0-Y00	u
51.		G29	u
52.	25	Y44:#C20	u
53.		I17:#24	u
54.	29	Y46:#Y44	u
55.		I12:#I11	u
56.		I14:#0	u
57.	33	G30 IF I12#0	u
58.		Y(60+I14):#Q3E,I12*Y460/I12	u
59.		G31	u
60.	30	Y(60+I14):#Y46	u
61.	31	32:I16:1:1.3:	u
61.5	27	I13:#A0+I14+I16	u
62.		G26IF(I12-I16)#0	u
63.		YI13:#(Q3E,(I12-I16)*Y460/I12-I16)	u
64.		+Q3E,(I12+I16)*Y460/I12+I16	u
65.		G32	u
66.	25	YI13:#Y46+Q3E,(I12+I16)*Y460/I12+I16	u
67.	32	I1:#I1	u
68.		G38 IF I14#5	u
69.		G34 IF I14#10	u
70.		G39 IF I14#15	u
71.		I14:#10	u
72.		I12:#0	u
73.		Y46:#Y44	u
74.		G33	u
75.	34	G35 IF Y0*Y23	u
76.		Y69:#1.0-Y0	u
77.		Y80:#(-Y69*C10*Y70)+(C11*Y71)-(Y69*C12*Y72)	u
78.		+C13*Y73	u
78.1		Y30:#(-Y69*Y70)+(0.5*Y71*0.75+Y69*Y69)-(0.5*Y69*Y72)	u
78.2		+0.125*Y73	u
79.		Y84:#Y70-(Y69*Y71)+0.5*Y72	u
79.5		Y80:#(Y80+Y104*Y30+Y36*Y84)/C14	u
80.		Y81:#((-Y69*C10*Y60)+(C11*Y61)-(Y69*C12*Y62)	u
81.		+C13*Y63)/C14	u
82.		Y82:#((-Y69*Y60)+(0.5*(0.75+Y69*Y69)*Y61)-(0.5*Y69*Y62)	u
83.		+0.125*Y63)/C14	u

83.1 Y82:#Y104\*Y82  
 84. Y83:#(Y60-(Y69\*Y61)+0.5\*Y62)\*Y104/C14  
 85. G36  
 86. 35 G58IF>.0\*#Y0-Y23  
 86.1 Y45:#C20  
 86.2 G59  
 86.3 58 Y45:#08E+1.0=Y0+Y230  
 87. 59 Y46:#Y45  
 88. I12:#Y11  
 89. I14:#6  
 90. G33  
 91. 38 I12:#0  
 92. I14:#15  
 93. G33  
 94. 39 Y69:#1.0=Y0  
 95. G22 IF Y23#0  
 96. 41. I12>.0+1.3  
 97. 40 Y(90+I12):#(Y(60+I12)-Y(65+I12))/Y23  
 98. 41 Y(100+I12):#(Y(70+I12)-Y(75+I12))/Y23  
 99. G56  
 100. 22 28. I12>.0+1.3  
 101. 37 Y(90+I12):#0.0  
 102. 28 Y(100+I12):#0.0  
 103. 56 Y80:#Y75-(Y76\*Y59+C16)+(Y77\*0.5)  
 103.1 -(Y69\*Y100)+(0.5\*Y101\*0.75+Y69\*Y69)  
 103.2 Y80:#Y80-(0.5\*Y59\*Y102)+0.125\*Y103  
 104. Y30:#(C10\*Y75)+(C12\*Y77)-(Y69\*C10\*Y100)  
 104.1 +(C11\*Y101)-(Y69\*C12\*Y102)+C13\*Y103  
 105. Y84:#Y76+Y100-(Y69\*Y101)+0.5\*Y102  
 105.5 Y80:#(Y30+Y104\*Y80+Y36\*Y84)/C20  
 106. Y81:#(C10\*Y65)+(C12\*Y67)-(Y69\*C10\*Y90)  
 107. +(C11\*Y91)-(Y69\*C12\*Y92)+(C13\*Y93)/C20  
 108. Y82:#Y65-((Y69+C16)\*Y66)+(0.5\*Y67)-(Y69\*Y90)  
 109. +0.5\*(0.75+Y69\*Y69)\*Y91  
 110. Y82:#(Y82-(0.5\*Y69\*Y92)+0.125\*Y93)/C20  
 110.1 Y82:#Y104\*Y82  
 111. Y83:#(Y65+Y90-(Y69\*Y91)+0.5\*Y92)/C20  
 111.5 Y83:#Y83\*Y104  
 112. 36 C1:#Y2  
 112.1 G93 IF I11\*1  
 112.2 C2:#Y81+Y83\*C35\*C34/C38  
 112.3 C2:#(C36\*C2)-C35\*C34\*C1  
 112.4 C2:#C2/((2.\*C32/C30)+C33\*C31)\*C34\*C34  
 112.5 G4  
 112.9 93 I0:#I0  
 113. C2:#((Y81+Y82+Y83\*Y36)\*Y37)-(Y38\*Y2)  
 114. -(1.0+Y42\*Y39-Y40\*Y80)\*Y43\*Y11/Y47  
 115. G4  
 116. 3 G5 IF (Y26-0.5\*C0)\*Y0  
 117. 53 G63 IF I11\*1  
 118. C300:#Y27\*Y80  
 119. C500:#Y79\*Y80  
 120. TY26 TC300 T(0.) TC500  
 120.1 C(300+I18):#C300  
 120.2 C(500+I18):#C500  
 120.3 G77 IF I24#0  
 120.34 I25:#600+I18  
 120.38 I26:#900+I18  
 120.4 68. I23, I25, 100, I26,  
 120.5 68 C123:#C500

120.6 77 C500:#Y81+C35\*C34\*((Y83/Y104)-Y2\*C37/C361)/C37  
 120.63 94 TY1 TY2 T(0.) TC500  
 120.66 G95  
 120.7 67 C500:#Y81+Y82+(Y83\*Y36)-(Y1+Y36\*Y2)\*Y31/Y34  
 120.8 TY1 TC300 TC400 TC500  
 120.85 95 IO:#IO  
 120.9 C(500+I18):#C(500+I18)+C500  
 121. G64 IF I11#1  
 121.1 C(400+I18):#C(400+I18)+C400  
 121.2 C(300+I18):#C(300+I18)+C300  
 121.3 C(200+I18):#C(200+I18)+Y1  
 121.4 G60 IF I24#0  
 121.5 75:I23:1:1:4:  
 121.6 49 I20:#30+I18+100\*I23  
 121.7 75 YI20:#YI20+Y1\*C(20+I23)  
 121.8 64 G60 IF I24#0  
 121.9 61:I23:1:1:4:  
 122. 62 I20:#500+(100\*I23)+I18  
 122.1 61 CI20:#CI20+C500\*C(20+I23)  
 122.2 G60  
 122.25 63 IO:#IO  
 122.3 TY26 T(0.) T(0.) T(0.)  
 122.4 C300:#Y29\*Y1  
 122.5 C400:#Y28\*Y1  
 122.6 G67  
 123. 60 G47 IF I18:#99  
 124. I18:#I18+1  
 125. Y26:#Y26+Y35  
 126. G74  
 127. 47 G51 IF I11#I19  
 128. I11:#I11+1  
 129. G92  
 129.1 51 T(0.)  
 129.2 82 T(0.)  
 129.4 83 TY120 TY121 TY122 T(Y123+Y124)  
 129.6 84 T(0.) T(-Y120) T(0.) TY120  
 129.7 85 TY123 T(Y123-Y124) TY123 T(Y123+Y124)  
 129.8 86 T(0.)  
 129.9 87 T(0.)  
 130. 52:I20:1:1:99:  
 131. 73 T(Y35\*I20) T(0.) T(0.) T(0.)  
 132. 88 TC(200+I20) TC(300+I20) TC(400+I20) TC(500+I20)  
 133. G52 IF I24#0  
 134. 89 TY(130+I20) TY(230+I20) TY(330+I20) TY(430+I20)  
 135. 90 TC(600+I20) TC(700+I20) TC(800+I20) TC(900+I20)  
 136. 52 I20:#I20  
 137. G57  
 138. 74 GI22 IF Y0:2.0+Y23=0.5\*CO  
 139. G5  
 140. 24 Y111:#Y1  
 141. Y112:#Y2  
 142. Y0:#Y26  
 143. Y50:#(1.0+(Y39-Y40\*C15)\*Y42)\*Y43  
 144. Y51:#Y38/2.0\*Y47  
 145. Y52:#Y50/Y47  
 146. G42 IF I11'1  
 147. Y80:#C15  
 148. Y81:#0.0  
 149. Y83:#Y104  
 150. Y114:#Y37\*Y104

ARMOUR RESEARCH FOUNDATION OF ILLINOIS INSTITUTE OF TECHNOLOGY

150.1		Y113:#Y114*1.0+(1.5*Y23)+Y36
150.2		G69
150.3	42	G43 IF I11'2
150.4		Y81:#C12
150.5		Y82:#Y104/2.0
150.6		Y83:#0.0
150.7		Y113:#Y37*C17
150.8		Y114:#0.0
150.81		Y120:#Y113/Y50
150.83		Y122:#Y28*Y120
150.85		Y123:#Y79*C15
150.87		Y124:#3.0*Y33*C17/(3.0*Y33)+4.0*Y31*Y31*Y31
150.89		Y121:#(Y123*Y31)+Y29*Y120
150.9		G69
151.	43	Y113:#0.0
151.1		Y81:#0.0
151.2		Y82:#0.0
151.3		Y83:#0.0
151.4		Y114:#0.0
151.5	69	Y54:#-Y51
151.6		Y53:#(Y113/Y50)-Y38*Y114/Y47*Y47
151.7		Y117:#Y114/Y50
151.8		Y57:#Y111-Y53
152.		Y116:#Y112-Y117
153.		G44 IF Y52*Y51*Y51
154.		G45 IF Y52*Y51*Y51
155.		T(2.) T(2.) T(2.) T(2.)
156.		I22:#48
157.	46	Y56:#06E*(Y51*Y51)-Y520
158.		Y58:#Y54+Y56
159.		Y59:#Y54-Y56
160.		Y85:#02E*Y560
161.		Y86:#02E*Y590
162.		Y87:#(-Y116+Y59*Y57)/2.0*Y56
163.		Y88:#(-Y116+Y58*Y57)/2.0*Y56
163.4		Y115:#-(Y52*Y57)-Y58*Y116)/2.0*Y56
163.5		Y119:#((Y52*Y57)-Y59*Y116)/2.0*Y56
164.	48	Y110:#Y25-2.0-Y23
165.		Y1:#(Y87*Y85PY110)+(Y88*Y86PY110)+Y53+Y117*Y110
166.		G70 IF I11'1
167.		Y82:#Y104*Y26-1.0-Y23/2.0
168.	70	Y21#(Y115*Y85PY110)+(Y119*Y86PY110)+Y117
168.4		G53 IF I11'1
168.5		G72
169.	44	I0:#I0
187.		T(1.) T(1.) T(1.) T(1.)
188.		I22:#54
189.		Y55:#06E*Y52-(Y51*Y51)0
190.		Y89:#(Y116-Y54*Y57)/Y55
190.5		Y118:#((Y54*Y116)-Y50*Y57/Y47)/Y55
191.		Y95:#02E*Y540
192.	54	Y110:#Y26-2.0-Y23
193.		Y109:#Y55*Y110
193.4		G71 IF I11'1
193.5		Y82:#Y104*Y26-1.0-Y23/2.0
194.	71	Y1:#((Y57*04E*Y1090)+Y80*03E*Y1090)*Y95PY110)+Y53
194.5		+Y117*Y110
194.6		Y2:#((Y118*03E*Y1090)+Y116*04E*Y1090)*Y95PY110)+Y117
195.		G53 IF I11'1
195.5		G72



195.7	45	IO: #10
196.		T(3.) T(3.) T(3.) T(3.)
197.		I22: #55
198.		Y96: #Y116-Y54*Y57
199.		Y95: #Q2E: Y54Q
200.	55	Y110: #Y26-2.0-Y25
201.		Y1: #((Y57+Y96*Y110)*Y95PY110)+Y53+Y117*Y110
201.4		Y2: #((Y116+Y54*Y96*Y110)*Y95PY110)+Y117
201.5		G53 IF I11+1
201.6	72	C46: #C35/C24*(2.*C32/C30)+C33*C31
201.65		C47: #C45*2.+C41-Y26
201.7		C48: #C36/C37
201.75		C49: #Y112-C48
201.8		C50: #Q2E: C47Q
201.85		Y2: #C46-C49*C50
201.9		Y1: #Y11-(C48*2.+C41-Y26)+(C49*1.-C50)/C46
202.		G53
203.	21	READ
204.		G1
205.	7	I5: #3*10
206.		Y(I5+1): #C0/2.0
207.		Y(I5+2): #1.0
208.		Y(I5+3): #C0/2.0
209.		Y(I5+5): #1.0*(0.5P0.5)
210.		Y(I5+4): #C0*Y(I5+5)
211.		Y(I5+6): #Y(I5+4)
212.		Y(I5+8): #1.0+0.5P0.5
213.		Y(I5+7): #C0*Y(I5+8)
214.		Y(I5+9): #Y(I5+7)
215.		Y(I5+10): #C0/6.0
216.		Y(I5+11): #1.0/3.0
217.		Y(I5+12): #C0/2.0
218.	6	I3: I1.1+1: I0:
219.	13	Y(I1+2*10): #0.0
220.	5	I4: #1+I5
221.		I2: I6.1+1+4:
222.	16	G2
223.	4	8: I1.1+1: I0:
224.	17	I2: #I1+10
225.		I3: #I2+10
226.		YI2: #YI4*CI1)-Y(I4+1)*YI3
227.		YI1: #YI1+YI2
228.	8	YI3: #YI3+(3.0*YI2)-Y(I4+2)*CI1
229.		G(I5+8)
230.	9	Y0: #Y0+C0/2.0
231.	10	G12
232.	11	G9
233.	12	I4: #I4+3
234.		G3

DISTRIBUTION (con't)

Copy No.

- 45-46 Office of the Chief, Corps of Engineers, US Army (Protective Construction Branch), Wash 25, DC
- 47-48 Director, US Army Waterways Experiment Sta (WESRL), P. O. Box 60, Vicksburg, Miss
- 49 Commanding Officer, US Army Engineering Research and Development Labs, Fort Belvoir, Va

NAVY ACTIVITIES

- 50 Chief, Bureau of Yards and Docks, Department of the Navy, (D-400), Wash 25, DC
- 51 Commanding Officer and Director, Naval Civil Engineering Laboratory, Port Hueneme, Calif
- 52 Officer-in-Charge, Civil Engineering Corps Officers, US Naval School, Naval Construction Battalion Center, Port Hueneme, Calif

OTHER DOD ACTIVITIES

- 53-54 Chief, Defense Atomic Support Agency, ATTN: Blast and Shock Division, Wash 25, DC
- 55 Commander, Field Command, Defense Atomic Support Agency (FCWT), Special Weapons Publication Distribution, Sandia Base, N Mex
- 56-65 ASTIA (TIPDR), Arlington Hall Sta., Arlington 12, Va

OTHER

- 66 University of Illinois, Talbot Laboratory, Room 207, ATTN: Dr. N. M. Newmark, Urbana, Ill  
Contract AF 29(601)-4508
- 67 Armour Research Foundation, Illinois Institute of Technology, 10 West 35th Street, Chicago 16, Ill  
Contract AF 29(601)-5008
- 68 University of New Mexico, Department of Civil Engineering, ATTN: Dr. Eugene Zwoyer, Albuquerque, N Mex  
Contract AF 29(601)-4520
- 69 Massachusetts Institute of Technology, Department of

DISTRIBUTION

Copy No.

HEADQUARTERS USAF

1	Hq USAF (AFOCE), Wash 25, DC
2	Hq USAF (AFCEI-ES), Wash 25, DC
3	Hq USAF (AFRDR), Wash 25, DC
4	Hq USAF (AFCIN-3B), Wash 25, DC
5	USAF Dep IG for Insp (AFCDI-B-3), Norton AFB, Calif

MAJOR AIR COMMANDS

6	AFSC (SCT), Andrews AFB, Wash 25, DC
7	SAC (OAWS), Offutt AFB, Nebr
8	AFLC, ATTN: Mr. Louis A. Nees, Wright-Patterson AFB, Ohio
9-10	AUL, Maxwell AFB, Ala
	AFOAR, Bldg T-D, Wash 25, DC
11	(RRONN)
	AFCLR, Hansom Fld, Bedford, Mass
12	(CRRA)
13	(CRZG)

AFSC ORGANIZATIONS

14	ASD (ASAPRL), Wright-Patterson AFB, Ohio
15-17	BSD (WDFN/Capt Fluhr), AF Unit Post Office, Los Angeles 45, Calif

KIRTLAND AFB ORGANIZATIONS

	AFSWC, Kirtland AFB, N Mex
18	(SWEH)
19-42	(SWOI)
43	(SWRS)

ARMY ACTIVITIES

44	Director, Ballistic Research Laboratories, ATTN: Library, Aberdeen Proving Ground, Md
----	---

TDR-62-1

DISTRIBUTION (con't)

Copy No.

Civil and Sanitary Engineering, ATTN: Dr. R. Whitman,  
Cambridge, Mass

Contract AF 29(601)-4927

70

Official Record Copy (SWRS)

<p>Air Force Special Weapons Center, Kirtland AF Base, New Mexico Rpt. No. AFSWC-TDR-62-1 (U) THE INVESTIGATION OF SILO AND TUNNEL LININGS. 162 p. incl illus., tables, 14 refs. Final report, March 1962</p> <p>Some of the aspects of the problem of determining the response of underground cylindrical tunnel and silo linings to blast-induced loading are presented in this report. The studies include the effects on silo linings of differential horizontal soil displacements, vertical skin-friction forces generated by vertical compression of the surrounding soil, and axial response of a silo with integral cover to the blast-induced cover loading.</p> <p>(U)</p>	<p>UNCLASSIFIED</p> <ol style="list-style-type: none"> <li>1. Blast loading</li> <li>2. Kinematics</li> <li>3. Model studies</li> <li>4. Pressure</li> <li>5. Soils -- effects of blast</li> <li>6. Stress and strain</li> <li>7. Tunnels -- effects of blast</li> <li>8. Underground shock waves</li> <li>9. Underground structures</li> <li>I. AFSC Project 1080, Task 108003</li> <li>II. Contract AF 29(601)-2596</li> <li>III. Illinois Inst. of Tech., Chicago Armour Research</li> </ol> <p>UNCLASSIFIED</p>	<p>Air Force Special Weapons Center, Kirtland AF Base, New Mexico Rpt. No. AFSWC-TDR-62-1 (U) THE INVESTIGATION OF SILO AND TUNNEL LININGS. 162 p. incl illus., tables, 14 refs. Final report, March 1962</p> <p>Some of the aspects of the problem of determining the response of underground cylindrical tunnel and silo linings to blast-induced loading are presented in this report. The studies include the effects on silo linings of differential horizontal soil displacements, vertical skin-friction forces generated by vertical compression of the surrounding soil, and axial response of a silo with integral cover to the blast-induced cover loading.</p> <p>(U)</p>	<p>UNCLASSIFIED</p> <ol style="list-style-type: none"> <li>1. Blast loading</li> <li>2. Kinematics</li> <li>3. Model studies</li> <li>4. Pressure</li> <li>5. Soils -- effects of blast</li> <li>6. Stress and strain</li> <li>7. Tunnels -- effects of blast</li> <li>8. Underground shock waves</li> <li>9. Underground structures</li> <li>I. AFSC Project 1080, Task 108003</li> <li>II. Contract AF 29(601)-2596</li> <li>III. Illinois Inst. of Tech., Chicago Armour Research</li> </ol> <p>UNCLASSIFIED</p>
<p>Air Force Special Weapons Center, Kirtland AF Base, New Mexico Rpt. No. AFSWC-TDR-62-1 (U) THE INVESTIGATION OF SILO AND TUNNEL LININGS. 162 p. incl illus., tables, 14 refs. Final report, March 1962</p> <p>Some of the aspects of the problem of determining the response of underground cylindrical tunnel and silo linings to blast-induced loading are presented in this report. The studies include the effects on silo linings of differential horizontal soil displacements, vertical skin-friction forces generated by vertical compression of the surrounding soil, and axial response of a silo with integral cover to the blast-induced cover loading.</p> <p>(U)</p>	<p>UNCLASSIFIED</p> <ol style="list-style-type: none"> <li>1. Blast loading</li> <li>2. Kinematics</li> <li>3. Model studies</li> <li>4. Pressure</li> <li>5. Soils -- effects of blast</li> <li>6. Stress and strain</li> <li>7. Tunnels -- effects of blast</li> <li>8. Underground shock waves</li> <li>9. Underground structures</li> <li>I. AFSC Project 1080, Task 108003</li> <li>II. Contract AF 29(601)-2596</li> <li>III. Illinois Inst. of Tech., Chicago Armour Research</li> </ol> <p>UNCLASSIFIED</p>	<p>Air Force Special Weapons Center, Kirtland AF Base, New Mexico Rpt. No. AFSWC-TDR-62-1 (U) THE INVESTIGATION OF SILO AND TUNNEL LININGS. 162 p. incl illus., tables, 14 refs. Final report, March 1962</p> <p>Some of the aspects of the problem of determining the response of underground cylindrical tunnel and silo linings to blast-induced loading are presented in this report. The studies include the effects on silo linings of differential horizontal soil displacements, vertical skin-friction forces generated by vertical compression of the surrounding soil, and axial response of a silo with integral cover to the blast-induced cover loading.</p> <p>(U)</p>	<p>UNCLASSIFIED</p> <ol style="list-style-type: none"> <li>1. Blast loading</li> <li>2. Kinematics</li> <li>3. Model studies</li> <li>4. Pressure</li> <li>5. Soils -- effects of blast</li> <li>6. Stress and strain</li> <li>7. Tunnels -- effects of blast</li> <li>8. Underground shock waves</li> <li>9. Underground structures</li> <li>I. AFSC Project 1080, Task 108003</li> <li>II. Contract AF 29(601)-2596</li> <li>III. Illinois Inst. of Tech., Chicago Armour Research</li> </ol> <p>UNCLASSIFIED</p>

<p>A theoretical method for estimating the forces acting on a cylindrical structure subjected to air blast-induced ground shock is presented. The radial forces on the surface of the cylinder consist of the undisturbed free-field pressure component plus pressures proportional to the radial velocity and displacement of the structure relative to the free-field particles. The effect of virtual mass, foundation modulus, and damping on the response was studied by obtaining solutions appropriate for tunnel and silo linings. Static tests on three metal, cylindrical tunnel models buried in dense Ottawa sand are presented and compared with the theoretical method. (U)</p> <p>Unclassified abstract</p>	<p>UNCLASSIFIED</p> <p>Foundation In ASTIA collection</p> <p>IV.</p>	<p>A theoretical method for estimating the forces acting on a cylindrical structure subjected to air blast-induced ground shock is presented. The radial forces on the surface of the cylinder consist of the undisturbed free-field pressure component plus pressures proportional to the radial velocity and displacement of the structure relative to the free-field particles. The effect of virtual mass, foundation modulus, and damping on the response was studied by obtaining solutions appropriate for tunnel and silo linings. Static tests on three metal, cylindrical tunnel models buried in dense Ottawa sand are presented and compared with the theoretical method. (U)</p> <p>Unclassified abstract</p>	<p>UNCLASSIFIED</p> <p>Foundation In ASTIA collection</p> <p>IV.</p>
<p>A theoretical method for estimating the forces acting on a cylindrical structure subjected to air blast-induced ground shock is presented. The radial forces on the surface of the cylinder consist of the undisturbed free-field pressure component plus pressures proportional to the radial velocity and displacement of the structure relative to the free-field particles. The effect of virtual mass, foundation modulus, and damping on the response was studied by obtaining solutions appropriate for tunnel and silo linings. Static tests on three metal, cylindrical tunnel models buried in dense Ottawa sand are presented and compared with the theoretical method. (U)</p> <p>Unclassified abstract</p>	<p>UNCLASSIFIED</p> <p>Foundation In ASTIA collection</p> <p>IV.</p>	<p>A theoretical method for estimating the forces acting on a cylindrical structure subjected to air blast-induced ground shock is presented. The radial forces on the surface of the cylinder consist of the undisturbed free-field pressure component plus pressures proportional to the radial velocity and displacement of the structure relative to the free-field particles. The effect of virtual mass, foundation modulus, and damping on the response was studied by obtaining solutions appropriate for tunnel and silo linings. Static tests on three metal, cylindrical tunnel models buried in dense Ottawa sand are presented and compared with the theoretical method. (U)</p> <p>Unclassified abstract</p>	<p>UNCLASSIFIED</p> <p>Foundation In ASTIA collection</p> <p>IV.</p>

<p>Air Force Special Weapons Center, Kirtland AF Base, New Mexico</p> <p>Rpt. No. AFSWC-TDR-62-1 (U) THE INVESTIGATION OF SILO AND TUNNEL LININGS, 162 p. incl illus., tables, 14 refs. Final report, March 1962</p> <p>Some of the aspects of the problem of determining the response of underground cylindrical tunnel and silo linings to blast-induced loading are presented in this report. The studies include the effects on silo linings of differential horizontal soil displacements, vertical skin-friction forces generated by vertical compression of the surrounding soil, and axial response of a silo with integral cover to the blast-induced cover loading.</p> <p>(U)</p>	<p>UNCLASSIFIED</p> <ol style="list-style-type: none"> <li>1. Blast loading</li> <li>2. Kinematics</li> <li>3. Model studies</li> <li>4. Pressure</li> <li>5. Soils -- effects of blast</li> <li>6. Stress and strain</li> <li>7. Tunnels -- effects of blast</li> <li>8. Underground shock waves</li> <li>9. Underground structures effects of blast</li> <li>I. AFSC Project 1080, Task 108003</li> <li>II. Contract AF 29(601)-2596</li> <li>III. Illinois Inst. of Tech., Chicago Armour Research</li> </ol>	<p>Air Force Special Weapons Center, Kirtland AF Base, New Mexico</p> <p>Rpt. No. AFSWC-TDR-62-1 (U) THE INVESTIGATION OF SILO AND TUNNEL LININGS, 162 p. incl illus., tables, 14 refs. Final report, March 1962</p> <p>Some of the aspects of the problem of determining the response of underground cylindrical tunnel and silo linings to blast-induced loading are presented in this report. The studies include the effects on silo linings of differential horizontal soil displacements, vertical skin-friction forces generated by vertical compression of the surrounding soil, and axial response of a silo with integral cover to the blast-induced cover loading.</p> <p>(U)</p>	<p>UNCLASSIFIED</p> <ol style="list-style-type: none"> <li>1. Blast loading</li> <li>2. Kinematics</li> <li>3. Model studies</li> <li>4. Pressure</li> <li>5. Soils -- effects of blast</li> <li>6. Stress and strain</li> <li>7. Tunnels -- effects of blast</li> <li>8. Underground shock waves</li> <li>9. Underground structures effects of blast</li> <li>I. AFSC Project 1080, Task 108003</li> <li>II. Contract AF 29(601)-2596</li> <li>III. Illinois Inst. of Tech., Chicago Armour Research</li> </ol>
<p>Air Force Special Weapons Center, Kirtland AF Base, New Mexico</p> <p>Rpt. No. AFSWC-TDR-62-1 (U) THE INVESTIGATION OF SILO AND TUNNEL LININGS, 162 p. incl illus., tables, 14 refs. Final report, March 1962</p> <p>Some of the aspects of the problem of determining the response of underground cylindrical tunnel and silo linings to blast-induced loading are presented in this report. The studies include the effects on silo linings of differential horizontal soil displacements, vertical skin-friction forces generated by vertical compression of the surrounding soil, and axial response of a silo with integral cover to the blast-induced cover loading.</p> <p>(U)</p>	<p>UNCLASSIFIED</p> <ol style="list-style-type: none"> <li>1. Blast loading</li> <li>2. Kinematics</li> <li>3. Model studies</li> <li>4. Pressure</li> <li>5. Soils -- effects of blast</li> <li>6. Stress and strain</li> <li>7. Tunnels -- effects of blast</li> <li>8. Underground shock waves</li> <li>9. Underground structures effects of blast</li> <li>I. AFSC Project 1080, Task 108003</li> <li>II. Contract AF 29(601)-2596</li> <li>III. Illinois Inst. of Tech., Chicago Armour Research</li> </ol>	<p>Air Force Special Weapons Center, Kirtland AF Base, New Mexico</p> <p>Rpt. No. AFSWC-TDR-62-1 (U) THE INVESTIGATION OF SILO AND TUNNEL LININGS, 162 p. incl illus., tables, 14 refs. Final report, March 1962</p> <p>Some of the aspects of the problem of determining the response of underground cylindrical tunnel and silo lining to blast-induced loading are presented in this report. The studies include the effects on silo linings of differential horizontal soil displacements, vertical skin-friction forces generated by vertical compression of the surrounding soil, and axial response of a silo with integral cover to the blast-induced cover loading.</p> <p>(U)</p>	<p>UNCLASSIFIED</p> <ol style="list-style-type: none"> <li>1. Blast loading</li> <li>2. Kinematics</li> <li>3. Model studies</li> <li>4. Pressure</li> <li>5. Soils -- effects of blast</li> <li>6. Stress and strain</li> <li>7. Tunnels -- effects of blast</li> <li>8. Underground shock waves</li> <li>9. Underground structures effects of blast</li> <li>I. AFSC Project 1080, Task 108003</li> <li>II. Contract AF 29(601)-2596</li> <li>III. Illinois Inst. of Tech., Chicago Armour Research</li> </ol>

<p>A theoretical method for estimating the forces acting on a cylindrical structure subjected to air blast-induced ground shock is presented. The radial forces on the surface of the cylinder consist of the undisturbed free-field pressure component plus pressures proportional to the radial velocity and displacement of the structure relative to the free-field particles. The effect of virtual mass, foundation modulus, and damping on the response was studied by obtaining solutions appropriate for tunnel and silo linings. Static tests on three metal, cylindrical tunnel models buried in dense Ottawa sand are presented and compared with the theoretical method. (U)</p> <p>Unclassified abstract</p>	<p>UNCLASSIFIED</p> <p>Foundation In ASTIA collection IV.</p>	<p>A theoretical method for estimating the forces acting on a cylindrical structure subjected to air blast-induced ground shock is presented. The radial forces on the surface of the cylinder consist of the undisturbed free-field pressure component plus pressures proportional to the radial velocity and displacement of the structure relative to the free-field particles. The effect of virtual mass, foundation modulus, and damping on the response was studied by obtaining solutions appropriate for tunnel and silo linings. Static tests on three metal, cylindrical tunnel models buried in dense Ottawa sand are presented and compared with the theoretical method. (U)</p> <p>Unclassified abstract</p>	<p>UNCLASSIFIED</p> <p>Foundation In ASTIA collection IV.</p>
<p>A theoretical method for estimating the forces acting on a cylindrical structure subjected to air blast-induced ground shock is presented. The radial forces on the surface of the cylinder consist of the undisturbed free-field pressure component plus pressures proportional to the radial velocity and displacement of the structure relative to the free-field particles. The effect of virtual mass, foundation modulus, and damping on the response was studied by obtaining solutions appropriate for tunnel and silo linings. Static tests on three metal, cylindrical tunnel models buried in dense Ottawa sand are presented and compared with the theoretical method. (U)</p> <p>Unclassified abstract</p>	<p>UNCLASSIFIED</p> <p>Foundation In ASTIA collection IV.</p>	<p>A theoretical method for estimating the forces acting on a cylindrical structure subjected to air blast-induced ground shock is presented. The radial forces on the surface of the cylinder consist of the undisturbed free-field pressure component plus pressures proportional to the radial velocity and displacement of the structure relative to the free-field particles. The effect of virtual mass, foundation modulus, and damping on the response was studied by obtaining solutions appropriate for tunnel and silo linings. Static tests on three metal, cylindrical tunnel models buried in dense Ottawa sand are presented and compared with the theoretical method. (U)</p> <p>Unclassified abstract</p>	<p>UNCLASSIFIED</p> <p>Foundation In ASTIA collection IV.</p>